MICROFLUIDIC DEVICES FOR FORENSIC DNA ANALYSIS

by

Jayna J. Shah
A Dissertation
Submitted to the
Graduate Faculty
of
George Mason University
In Partial Fulfillment of
The Requirements for the Degree
of
Doctor of Philosophy
Electrical and Computer Engineering

Committee:

_____ Dr. Rao V. Mulpuri, Dissertation Director
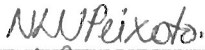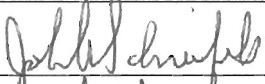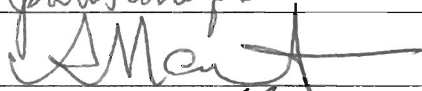
_____ Dr. Michael Gaitan, Committee Member

_____ Dr. Dimitrios E. Ioannou, Committee Member

_____ Dr. Nathalia Peixoto, Committee Member

_____ Dr. John A. Schreifels, Committee Member

_____ Dr. Andre Manitius, Department Chairperson

_____ Dr. Lloyd J. Griffiths, Dean, The Volgenau
                           School of Information Technology and
                           Engineering

Date: 10/25/2007   Fall Semester 2007
                           George Mason University
                           Fairfax, VA

Microfluidic Devices for Forensic DNA Analysis

A dissertation submitted in partial fulfillment of the requirements for the degree of Doctor of Philosophy at George Mason University

By

Jayna J. Shah
Master of Science
George Mason University, 2007

Director: Rao V. Mulpuri, Professor
Department of Electrical and Computer Engineering

Fall Semester 2007
George Mason University
Fairfax, VA

DEDICATION

This thesis is dedicated to my wonderful parents Jagat and Ragini Shah for their guidance during the early years, and my husband Dhaivat Parikh for his continued love and support.

ACKNOWLEDGEMENTS

I am extremely grateful to my parents for always believing in me, letting me follow my own path, and supporting all my decisions. I like to express many thanks to my sister Bhavini Shah and brother Vaishal Shah for their words of encouragement and for always being there for me when I needed them. I hope you will continue to do the same in future regardless of our geographic location. I would also like to thank my late father-in-law for all his support. I really wish that you had waited another month to see me being called a Doctor. I want to thank my mother-in-law for her encouraging words and strength despite her loss. Finally, I would like to express immeasurable thanks to my loving husband and friend, Dhaivat Parikh - thank you, Thank You, and THANK YOU. None of this would have been possible without your patience, constant encouragement, love, and emotional support.

TABLE OF CONTENTS

LIST OF TABLES

LIST OF FIGURES

x

LIST OF COMMONLY USED ABBREVIATIONS

bp……………………………………base pair
CE………………………………...capillary electrophoresis
COC……………………………...cyclicolefin copolymer
CPW……………………………...coplanar waveguide
DEA……………………………...diethylacrylamide
DMA……………………………...dimethylacrylamide
DNA……………………………...deoxyribonucleic acid
FWHM…………………………...full width at half maximum
EOF……………………………....electroosmotic flow
HPMC…………………………....hydroxypropyl methyl cellulose
LIF………………………………..laser-induced fluorescence
LPA……………………………....linear polyacrylamide
N………………………………...theoretical plates
η………………………………..efficiency
PC……………………………….polycarbonate
PCR…………………………….....polymerase chain reaction
PDMS……………………………poly(dimethyl siloxane)
PET………………………………poly(ethylene terephthalate)
PMMA…………………………...poly(methylmethacrylate)
PS……………………………….polystyrene
PVA……………………………....poly(vinyl alcohol)
PVC……………………………....poly(vinyl chloride)
$\mathscr{R}$……………………………....resolution
S-parameter…………………...scattering parameter
SEM……………………………...scanning electron microscopy
ssDNA…………………………...single-stranded DNA
T_g……………………………....glass transition temperature
TTE……………………………Tris Taps EDTA
µTAS……………………………micro total analysis system

ABSTRACT

MICROFLUIDIC DEVICES FOR FORENSIC DNA ANALYSIS

Jayna J. Shah, Ph.D.

George Mason University, 2007

Dissertation Director: Dr. Rao V. Mulpuri

The development of integrated, miniaturized, and portable DNA analysis systems is crucial to alleviate massive backlog of unanalyzed samples and to address ever increasing demand for these assays. This thesis work contributes towards the development of a fully integrated microdevice capable of "sample in – answer out" for forensic DNA analysis. Specifically, this work describes the development of rapid and robust fabrication protocol for solvent-actuated bonding of polymeric thermoplastic substrates at room temperature, the development of microchannel wall coating strategies to eliminate analyte-wall interactions for high resolution separation of single-stranded DNA, and the characterization of a thin-film planar microwave transmission line for microfluidic heating applications.

The solvent-actuated bonding protocol was based on the difference in capillary forces between the microchannel and the interstitial space between the surfaces of the two substrates to be bonded. This force differential wicked the bonding solvent into the

gap between the substrates causing them to bond. The technique was implemented by placing the two substrates under moderate pressure, applying a moderate pneumatic vacuum to the fluidic channel, and introducing tens of microliter of bonding solvent through one end of the fluidic channel. The effect of bonding solvent on the dimensions of the microchannel was analyzed, and the mechanical robustness of the bonded devices was also characterized. Electrophoretic separation of single-stranded DNA (ssDNA) was successfully performed to demonstrate the functionality of these devices.

To enhance ssDNA separation performance, schemes to modify poly(methyl methacrylate) (PMMA) – the primary substrate used in this work – were explored. This two step process consisted of altering surface hydrophilicity via surface activation using either nitric acid or UV/ozone followed by coating the surfaces with adsorptive polymers. Contact-angle measurements of the pristine and modified PMMA substrates were performed to quantify the change in wettability of the surface. Twofold increase in the separation efficiency was achieved by implementing these surface passivation strategies.

Finally, the use of a thin-film planar microwave transmission line as a microwave power source was investigated for on-chip microwave heating of fluids. The microwave characterization data was used to develop a first-order analytic model of the microwave power absorption. The model was used to understand microwave power flow through the device and to calculate the fraction of the incident power absorbed in the fluid. Additionally, a fit of the predicted temperature obtained using this model to the measured temperature was performed to evaluate efficiency of this heating method.

1. Introduction

Throughout history, humans have always tried to improve the tools they use. Miniaturization through scientific breakthrough has been the heart of technological advances, and it has become an important facet of our lives. Miniaturization methods are well-developed in the microelectronics industry. In 1965, when Gordon Moore made his first prediction about the number of transistors in a chip increasing exponentially over time [1], the transistor size was 100 μm. As epitomized by Moore's Law, the transistor size has reduced to 45 nm in 2007 over four decades and have brought the world ever faster and more powerful computers. Today, we are constantly lured into purchasing smaller and smaller cameras, PDAs, cell phones, and computers. Similar to the advances in the microelectronics industry, the area of biological and chemical analysis is undergoing a miniaturization effort. The benefits associated with miniaturization of biological and chemical analysis are mostly analogous to the benefits associated with miniaturization in the integrated circuit industry. These benefits include reduction in size and cost of equipment, faster analysis, shorter reaction times, and the possibility of parallel operation for multiple analysis as well as portable devices. One such chemical analysis pertinent to our daily lives is human identification through genetic material, especially for the criminal justice system. The goal of this thesis work is to investigate miniaturization of forensic DNA analysis methods through the use of microfluidic technology.

1

1.1.   Forensic DNA Analysis: Overview

Human identification by analysis of specific regions of DNA, within the human genome, was one of the biggest revelations of the twentieth century. The DNA evidence was first used in the English court system in 1986 [2]. It has since emerged as perhaps the most powerful evidentiary technique for the criminal justice system. Today, more than 20 years after its first use, forensic DNA identification remains a highly effective way to identify the source of biological evidence and a key to ensure accuracy and fairness in the criminal justice system. Forensic DNA analysis is a versatile method with applications in different branches of the justice system – criminal law, family law, and immigration law. Some of its applications in criminal law include helping prove guilt or innocence, identify crime and catastrophe victims, in family law to establish paternity, and in immigration law to prove blood relations to establish citizenship [3, 4].

Forensic DNA analysis, an indispensable and routine part of modern forensic casework, is a comparative measurement technique. This technique consists of analyzing biological sample, such as blood, hair, skin, saliva, or semen, found at the crime scene to determine individual's unique DNA profile (except in the case of identical twins). This is followed by interrogation of large DNA databases such as FBI's combined DNA index system (CODIS) [5] for finding matches to DNA profile generated from crime scene sample, or finding even partial matches to close relatives of a perpetrator [3].

The majority of human DNA, over 99.7%, is the same between people. It is the variation of only a small fraction (0.3% or ~ 10 million nucleotides) within the non-coding regions of the human genome that is responsible for the genetic difference

between people, making us unique individuals [3]. These variable regions of DNA, which provide the capability of using DNA information for identity purposes, are used for distinguishing one individual from the other through forensic DNA profiling. Specifically, the current methods for examining nuclear DNA are based on the amplification and detection of short tandem repeat (STR)-length polymorphisms (the existence of multiple alleles at a single locus). STRs, which account for 0.3% of the total human genome, are tandemly connected DNA regions of length 2 – 7 base pairs. These units are commonly repeated about 7 – 20 times and the number of these repeats can be highly variable among individuals [3]. Primarily, STRs are distributed throughout noncoding regions of the genome known as junk DNA. A combination of several tandemly repeating regions allows for highly effective discrimination tool for human identification purposes. For instance, according to current forensic DNA standards applicable in the United States, an individual's DNA profile consists of the alleles present at 13 specific chromosomal locations. When DNA profile contains alleles analyzed simultaneously at all of the 13 locations, the probability of two unrelated individuals having the same DNA by chance has been shown to be one in a trillion [3], offering highly discriminating DNA profiles. In addition to offering highly discriminating DNA profiles to forensic community, PCR-based STR analysis is the method of choice for forensic applications due to lower requirement of DNA sample (on the order of ng), and smaller size of generated DNA fragments, which allows for faster and easier electrophoretic separation.
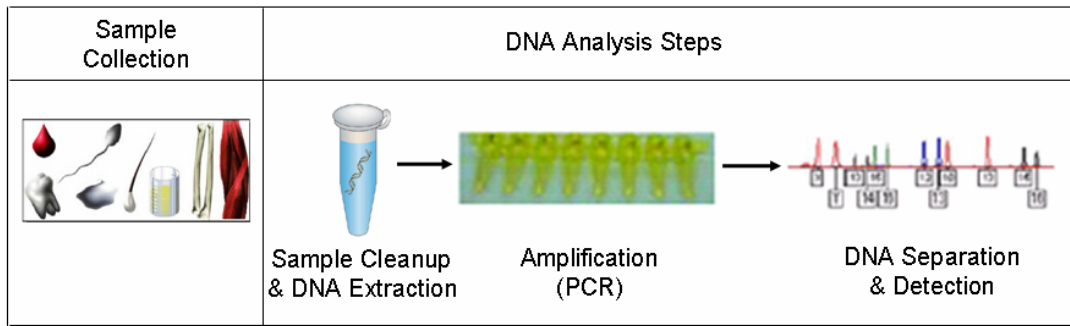
Figure 1-1: A schematic flow chart of typical steps involved in forensic DNA analysis (partially adapted from [3]). Cell membrane is first ruptured to release the nucleic acid(s) of interest. These nucleic acids are then purified and quantified to determine the quality of DNA recovered. The nucleic acids are then amplified, which is followed by separation and detection of short tandem repeats (STRs).

Figure 1-1 presents a flow chart of the major steps involved in forensic DNA analysis. The biological cells are first disrupted by chemical, osmotic, thermal, electrical, mechanical, or enzymatic means to rupture the cell membrane and extract the intracellular material. The intracellular material is then purified and measured to evaluate the quantity and quality of recovered DNA. These extraction methods are primarily employed to separate proteins and other cellular materials from the DNA molecules that inhibit the ability to analyze DNA. After extraction, the DNA undergoes a process known as polymerase chain reaction (PCR). PCR, often analogized as molecular 'photocopying,' is a process by which a specific region of DNA is replicated over and over again to yield millions of copies [6]. This is accomplished by heating and cooling samples in a precise thermal cycling pattern. The concentration of DNA increases exponentially after each cycle; hence, the ability to analyze very minute amount of initial sample. The PCR-end product can contain 20 or more DNA fragments that have to be

resolved from one another. In order to distinguish the various fragments from one another, a separation step is performed to pull the different sized fragments apart. This length based separation is typically performed by a process known as electrophoresis, which is an electrically driven charged analyte separation technique.

Since DNA extraction and quantitation are not part of this thesis work, only the information and literature pertinent to PCR and DNA separation is described in detail here. However, a detailed review of DNA purification and quantitation methods can be found in ref. [7].

1.2. PCR Amplification

PCR is the second process carried out in typical genetic analysis (Figure 1-1). It was first introduced by Saiki and co-workers [8] almost two decades ago, and has since become an indispensable tool for scientists in the life sciences, whether it involves molecular-, biological-, diagnostic-, forensic-, or agricultural-related analysis [6].
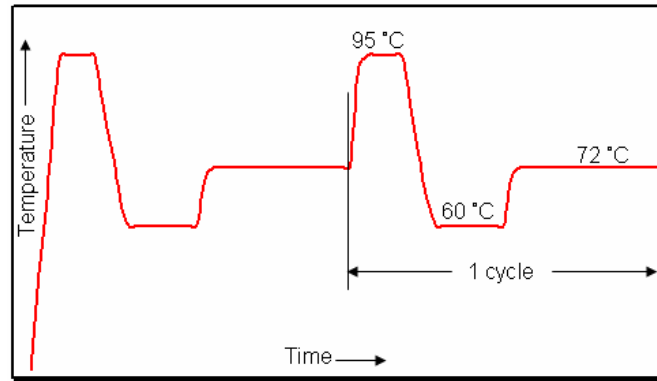
Figure 1-2: Typical thermocycling profile showing two cycles for PCR amplification. Thermal cycling typically involves three different temperatures that are repeated 25 to 35 times. At 95 ˚C, the DNA strands separate, or denature. At 60 ˚C, primers bind or anneal to the DNA template (the region to be amplified). At 72 ˚C, the DNA polymerase extends the primers by copying the target region.

PCR is an *in vitro* enzymatic process in which a specific region of DNA is replicated repeatedly to yield many copies of a particular sequence. PCR relies on thermocycling through three different temperatures as depicted in Figure 1-2. During the first step, called denaturation, the hydrogen bonds holding the double-stranded DNA template are broken to form two complementary single-strands of DNA (ssDNA). This step is performed at temperatures between 94 ˚C and 96 ˚C. This is followed by lowering the temperature of the reaction solution between 50 ˚C to 70 ˚C, called the annealing temperature, to allow primers to bind to the complementary sequences of the template DNA. The primers are synthetic sequences of ssDNA, which flank the template DNA and target the region to be amplified. In the final step, called extension, the temperature is raised close to 72 ˚C to allow replication of DNA. During this step, the DNA polymerase – DNA precursors present in the reaction solution – extends the primers by

6

copying the template DNA using the deoxynucleotide triphosphate building blocks [9].

This denaturation-annealing-extension process is repeated between 20-40 times with

appropriate hold times at each step. If 100% efficiency of the reaction is assumed,

template DNA will double in quantity at the end of each cycle. Hence, in theory, an

exponential amplification of a template DNA occurs and 30 cycles should yield 1.1

billion copies of the template DNA starting with only one copy.

Thus, thermocycling of the reaction mixture is an integral part of performing

successful PCR amplification. Additionally, Wittwer and Garling [10] emphasized that

precise thermal control during temperature hold times and rapid transition times between

temperature set points should result in optimal PCR efficiency.

1.2.1. Conventional PCR Amplification

Thermocycling for PCR amplification can be accomplished in a number of ways.

The conventional systems utilize metal blocks to hold thin-walled plastic PCR reaction

tubes. During amplification, the metal blocks are heated and cooled, in turn, heating and

cooling the PCR tubes containing the reaction mixture. This block heating method relies

on physical contact between the tubes and thermal block for transfer of heat. This

combined with relatively large reaction volumes required, typically 10-50 µL, results in

PCR amplification time on the order of three hours (for 30 cycles) [7]. While

conventional systems are improving in speed (heating rate of 1 ˚C/sec for widely used

GeneAmp PCR System 9600 from Applied Biosystems), they are still very time

consuming and the cost of reagents at the required volumes is very high. The limiting

factor for fast thermocycling and PCR amplification resides in the large thermal mass of the metal heating blocks. Additionally, transition times with these systems are much too slow to realize optimal PCR efficiency as suggested by [10].

1.3.   Electrophoretic Analysis

As mentioned earlier, the standard method used for separation of DNA following PCR is gel electrophoresis. Electrophoresis is an analytical technique involving the movement of electrically charged analytes under the influence of an electric field in a conductive liquid medium [11]. In the case of DNA, the phosphate groups on the backbone of DNA have a negative charge, which causes the DNA molecules to move toward the positive electrode under the influence of an electric field. The higher the voltage, the greater the electric force experienced by the DNA molecules, and the faster the movement of DNA.
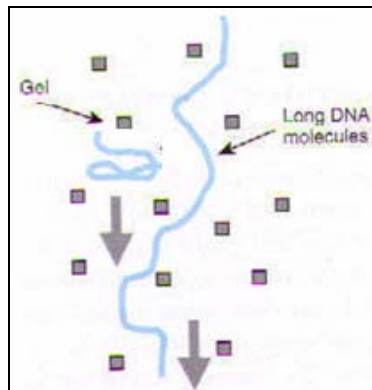
Figure 1-3: Migration of DNA molecules through sieving matrix or gel in electrophoresis (Adapted from [3]). Larger molecules interact more frequently with the pores and are thus retarded more in their motion compared to smaller molecules.

The migration of analytes during electrophoresis is dependent on their charge-to-size ratio. However, with one phosphate group for every nucleotide, DNA molecules possess a constant charge-to-mass ratio. Thus, a DNA molecule that is 50 nucleotide units long will experience the same electrostatic force as a DNA molecule that is 100 nucleotide units in length. Hence, a sieving matrix is required to retard the motion of DNA fragments based on their size. Typically, these sieving matrices are cross-linked gels or entangled polymers that serve as the sieving medium for the DNA molecules migrating toward the anode. The pore sizes formed within these matrices provide a medium through which migration of DNA fragments can be retarded based upon their size. The smaller DNA molecules travel through the sieving medium pores faster and reach the detector first, whereas larger DNA molecules move slower than the smaller DNA fragments (Figure 1-3). This difference in migration time results in size-based separation of DNA fragments [12]. Thus, the differences in the DNA fragment lengths provide basis for separating the fragments based on their length.

It is important to note that electrophoresis is a relative rather than an absolute measurement technique. A sizing standard containing known DNA fragment sizes is used to calibrate the migration times of the DNA fragments of interest [3].
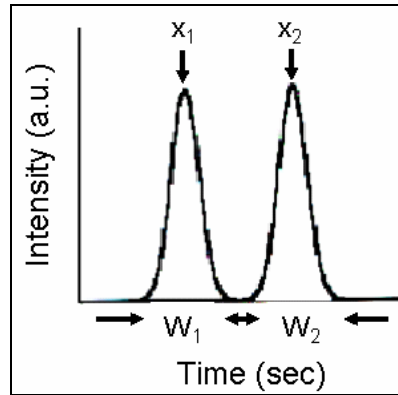
Figure 1-4: Determination of resolution and efficiency from an electropherogram. Adapted from Grossman [13].

As with chromatography, resolution is a parameter used in capillary electrophoresis (CE) to characterize the degree to which two components are separated. The basic definition of resolution, *R,* in an electrophoretic separation is given as the ratio of the distance between two peaks and the average peak width [12, 14]:

$$R = \frac{x_2 - x_1}{\frac{1}{2}(w_1 + w_2)}$$
(1-1)

where $(x_2 - x_1)$ is the distance in time domain between two peaks of DNA of different and known length, and w_1 and w_2 are the baseline peak widths (in time units) for each fragment. These values can be obtained from an electropherogram of the DNA separation as depicted in Figure 1-4. The efficiency of an electrophoretic process is analyzed by calculating theoretical plate numbers, *N,* and theoretical plate height, *H,* where:

$$H = \frac{L}{N} = \frac{\sigma_T^2}{L}$$
(1-2)

10

and L is the effective separation length (cm), σ_T^2 is the total variance due to multiple

dispersive phenomena on the analyte [12]. The number of theoretical plates can be

calculated as:

$$N = \frac{t^2}{(FWHM / 2.35)^2}$$ (1-3)

where t is the migration time in seconds and FWHM is the width measured at half the

peak height.

The total variance due to multiple dispersive phenomena in electrophoresis is

summarized using the following relationship [14]:

$$\sigma_T^2 = \sigma_{diff}^2 + \sigma_T^2 + \sigma_{inj}^2 + \sigma_{wall}^2 + \sigma_{det}^2$$ (1-4)

where σ_{diff}^2 represents variance due to molecular diffusion, σ_{inj}^2 represents variance due

to the injection system, σ_T^2 represents variance caused by temperature due to joule

heating, σ_{wall}^2 represents the variance due to the interactions of the analyte and column

wall, and σ_{det}^2 represents the variance due to the detection system.

1.3.1. Conventional Electrophoretic Analysis

Conventionally, slab gel electrophoresis [3] was the preferred method of choice

for separating DNA fragments as well as other biomolecules. This technique offers the

advantage of high throughput capacity (samples can be analyzed in 96 lanes

simultaneously), but it has been shown to be time-consuming, labor-intensive, and not

readily amenable to integration or automation [12]. Slab gels require microliters of costly

sample volumes. Waste disposal of toxic substances and radioactive detection probes used in slab gel electrophoresis are also limiting factors for its use. Additionally, poor heat dissipation of slab gels limit electric fields to < 100 V/cm and as a result, separation speed is limited.
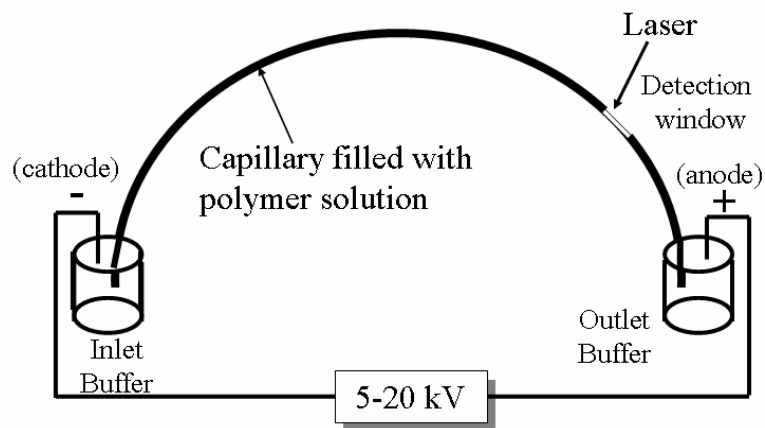
Figure 1-5: Schematic of a capillary electrophoresis instrument. Adapted from Butler [15].

Alternatively, capillary electrophoresis (CE), the standard method for most forensic laboratories in the world [15], has been shown to be highly reproducible and effective for rapid separations of DNA molecules as well as other biomolecular analytes. As shown in Figure 1-5, the primary elements of CE instrument include a narrow fused-silica capillary of 20-100 μm internal diameter and 20-100 cm length, two buffer vials, two electrodes connected to a high-voltage power supply, a laser excitation source, and a fluorescence detector. To compensate for a constant charge to mass ratio of DNA and to

produce conditions similar to slab gels, high viscosity buffers or polymerized gels that have pores similar to the slab gels are introduced into the capillaries [12]. During electrophoresis, the ends of the capillary are inserted into buffered solutions, and an electric field (~ 300 V/cm) is applied to induce separation. DNA fragments attached with fluorescent dyes are illuminated with laser light as they pass through the window and the fluorescence emitted from the dyes are used to detect and quantify DNA molecules.

Compared to slab gels, the high surface area-to-volume ratio of capillaries permits their operation at much higher field strengths resulting in shorter electrophoretic separation times. Also, in comparison with microliter of sample volumes required for slab gels, nanoliter to picoliter quantities of sample is required for capillary electrophoresis. Although CE allows rapid, high resolution separations compared to slab gels, commercial equipment used for CE are expensive and bulky. Further, the most commonly used CE instrument by the crime labs, single-capillary, process samples at a rate of approximately one sample per 30 min. The standard capillary length required for STR separations to obtain the needed resolution is 42 cm and this technology does not provide the opportunity to integrate sample preparation steps.

1.4.   Forensic DNA Analysis: Limitations of Existing Technology

Growing popularity and demand for this human identification method has resulted in tremendous progress towards the development of efficient, precise, and robust protocols for implementation of this technique, and it has also provided impetus towards further development. Even though technologies used for performing forensic DNA

analysis have experienced tremendous growth over the past 20 years, several limitations have hindered the widespread use of this technique.

Currently, each of the analytical process steps involved in Forensic DNA analysis, (DNA extraction, amplification, and separation) as shown in Figure 1-1, is executed individually and often times in separate laboratories, with analysis times ranging from hours to days [16, 17]. Macroscopic protocols, presently in use, require large volumes of sample and reagents increasing the cost of analysis. Moreover, bench-top analytical systems employed for performing DNA analysis utilize various manual and time-consuming laboratory processes, including centrifugation, filtration, measuring, mixing, and dispensing [18]. These processes, because of their manual nature, are prone to human errors, which can potentially compromise the data and result in increased costs. Additionally, these systems require highly trained personnel with extensive expertise and expensive equipment in laboratory setting to complete assays [19].

On the other hand, another problem facing the forensic community is the massive backlog of unanalyzed DNA samples awaiting analysis. According to the National Institute of Justice 2004 Annual Report and a report published by Pratt *et. al.* in Criminal Justice Polity Review in 2006 [20], estimates place the national DNA backlog at approximately 542,000 from unsolved homicide, rape, and property offense cases.

1.5. Forensic DNA Analysis: Automation, Integration, and Miniaturization

Although some of the labor- and time-intensive procedures have been recently streamlined by the use of robotic handlers, smaller, faster, and cheaper analysis tools have the potential to reduce capital investments for crime laboratories while increasing

their capacity. Therefore, technologies that may decrease the time and expense of conducting DNA analysis in the laboratory and augment the portability of DNA analysis devices warrant attention to satisfy the burgeoning need for high-throughput and low-cost forensic DNA profiling.

The development of integrated microchip based DNA technologies that assemble all analytical process steps into a single, seamless system have numerous advantages over the current technology – the potential to automate processing, decrease analysis time, increase efficiency, decrease manual sample handling, decrease sample and reagent consumption, and enable investigative uses of DNA closer to the crime scene [7]. With decreased sample handling, opportunity for sample contamination during sample processing is limited. With automated processing and reduced use of sample and reagents, the cost of analysis is lowered. Thus, the inherent potential of microfluidic technology can be utilized to combine integrated sample preparation with parallel, high-throughput, microchip-based electrophoresis, reducing the cost and analysis time required for performing DNA analysis.

1.5.1. A Brief Overview of Microfluidics

Microfluidics [21] is manipulation of small quantities of fluids in channels. Microfluidic systems consist of channels and reservoirs with at least two dimensions typically of sub-micron scale to hundreds of micrometers. Microfluidic devices are utilized in a wide variety of applications to control the flow of liquids and gases ranging in volume from sub-nanoliter to microliter. The most familiar microfluidic application is

inkjet printing that revolutionized home printing in the late 80's. The first reported use of a microfluidic device was a miniaturized gas chromatography system created on a silicon wafer in 1979 [22]. However, after the first publications, a decade passed without any major milestones in the field. It was not until 1990 when Manz and colleagues realized the potential of miniaturization for liquid phase separations that this field gained attention [23]. The first reports of microfluidic systems in the literature were of microfabricated electrophoretic separations [24, 25] followed by diffusive separation systems [26], and DNA amplification [27, 28]. Over the last decade, integrated microfluidic devices, also known as lab-on-a-chip devices or micro total analysis systems (µTAS), have gained researchers' attention in multiple disciplines. As a result the field has blossomed and branched off into many areas, including biological and chemical analysis [29, 30], point-of-care testing [31], clinical and forensic analysis [32], molecular diagnosis [33], and medical diagnosis. Some of the specific applications of microfluidic devices have expanded to include sample preparation, fluid handling, microreactors, separation systems, cell handling, and cell culturing.

Most significant benefits of microfluidic systems include high performance, design flexibility, reduced reagent volumes and associated cost, miniaturization, and automation [23, 34]. Miniaturization allows high-throughput, portability, lower cost, lower consumption of material and energy. The use of smaller amount of material also makes disposability economical; avoiding possible cross contamination in sensitive analytical processes. Since the most significant benefit of microfluidics is the ability to integrate multiple functionalities on a single device, an ideal integrated DNA analysis

system will be the one that accepts a complex biological sample (blood, semen, or saliva), remove PCR inhibitors, amplify the DNA, and separate and detect STR fragments of interest.

1.5.2. Microchip PCR Amplification

The introduction of microchip PCR in the early to mid-1990s revolutionized STR-based forensic DNA analysis. The first reports of PCR in a chamber created in a microfluidic device were published by Northrup and co-workers [35] in 1993 and Wilding *et. al.* [27] in 1994. Northup and colleagues used reagent volume of 25 – 50 µL; Wilding *et. al.* used a silicon/glass hybrid device and heated 5 – 10 µL of PCR reaction mixture. Both groups employed an external copper block heater and heated the entire microchip. These reports were followed by tremendous efforts from researchers worldwide to develop microchips for PCR amplification including a variety of substrates, heating methods, and surface chemistry. Since some of the work in this thesis focuses on evaluating a new heating method for PCR amplification, a brief review of microchip-based PCR is discussed here. Current research on PCR microchips is divided based on thermal cycler technology – contact and noncontact. This distinction of temperature cycling methods for microfluidic devices was made by Roper *et. al.* [6].

Contact heating methods are defined as those having heaters fabricated within the microchip or in contact with the microchip. Noncontact heating methods are defined as those having heaters remote from the microchip. Contact heating methods rely on

17

transfer of heat from a heated surface to fluid introducing substantially more thermal mass compared to noncontact heating methods.

Contact Heating Thermal Cyclers
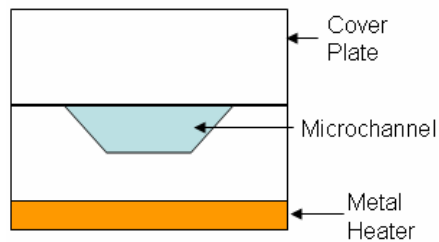
Figure 1-6: Contact based stationary thermal cycler for PCR. The sample is introduced into a microfluidic channel followed by heating and cooling of the entire microchip to provide thermocycling conditions.

Contact based thermal cycling methods fall into two categories: stationary and flow-through. Stationary thermal cyclers (Figure 1-6) heat and cool a static volume of fluid, whereas flow-through thermal cyclers force the PCR mixture to flow through constantly heated zones. Both methods are based on resistive (embedded or external) [36] or peltier based [37] heating elements. The stationary contact heating method, since its introduction, has been replicated and modified by many researchers in the field. Modifications include microchip PCR integration with microchip electrophoresis [38-40], single molecule detection [41], real-time PCR [42], low volume PCR reaction [43, 44], multiplexing [40, 45], temperature uniformity [46], and heat transfer optimization [47]. Even though these devices present excellent freedom for the design of PCR reaction

chamber, their temperatures need to be altered for performing temperature cycling, introducing unnecessary thermal mass and limiting thermal cycling rates.
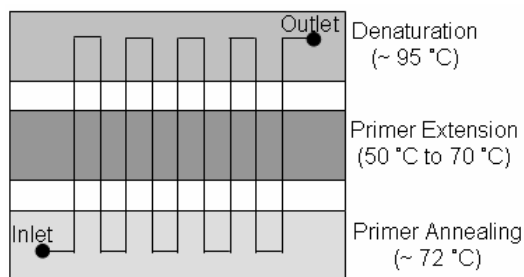
Figure 1-7: Contact based flow through thermal cycler. The sample is introduced through inlet and continuously flowed pumped towards the outlet. Three heaters at constant temperature are used to provide thermal cycling conditions.

As mentioned above, flow through thermocyclers similar to that shown in Figure 1-7 pump the PCR reaction mixture through constantly heated zones. The first flow through PCR amplification method was published by Kopp *et. al.* [48] in 1998. The device consisted of three heated zones, correlating to annealing, extension, and denaturation temperatures of thermocycling. The reaction mixture was flowed through each zone in a continuous serpentine channel with the hold times at each temperature depending on the flow rate of the mixture through the zones. A 25-cycle flow-through thermal cycler system developed by Schneegass *et. al.* [49] utilized platinum heaters microfabricated on a silicon wafer anodically bonded to a glass wafer containing the reaction chamber to heat the reaction mixture. These continuous-flow approaches allow

19

for faster heating and cooling rates compared to the static flow approach because time to change temperature of the fluid depends only on the flow rate the time and the sample takes to reach thermal equilibrium. However, one major disadvantage is that these devices are restricted in the number of cycles they can handle as they are decided during the design stage, which can only be modified at the expense of cost and time after fabrication. This issue was circumvented by Liu *et. al.* [50] who developed a rotary device with integrated heaters for microchip PCR. They introduced 12 nL sample into the chip and pumped it at a rate to enable 2-3 revolutions per minute. Subsequent modification to this method has included improvements in the number of cycles, PCR conditions to prevent cross-contamination during injection, etc [51, 52]. Even though the number of cycles was easily modifiable with their design, the fabrication process required additional and complex steps. In addition, this method is neither amenable to integration with other sample processing steps nor is it suitable for parallelization.

Noncontact Heating Thermal Cyclers

Limitations associated with contact heating methods for microchip PCR amplification were first realized by the Landers group of the University of Virginia and pioneering work was carried out by this group to develop noncontact heating methods based on infrared radiation (IR). The first report was published by Oda *et. al.* [28], which utilized IR light source (tungsten lamp) to selectively heat ~ 28 µL solution rather than the microchip substrate. Subsequently, further work was carried out to modify this heating method to decrease sample volume and improve thermal cycling rates resulting in several publications [53-55]. Most recently the group demonstrated 25-cycle

amplification with 130 nL reaction volume in 5 min in borosilicate glass microdevices [56].

1.5.3. Microchip Forensic DNA Electrophoresis

Microfabricated CE devices offer several advantages over standard fused silica capillaries. The shallow channel depths coupled with wide surfaces result in relatively high surface area to volume ratios, which is necessary for efficient dissipation of heat generated due to electrical current flowing in the microchannel during electrophoresis. More importantly, microfabrication processes allow precise definition of sample plug width through injection cross channel [57]. Since resolution is a strong function of the dimensions of the injection plug, the microfabricated CE devices result in higher resolution compared to their conventional capillary counterpart.
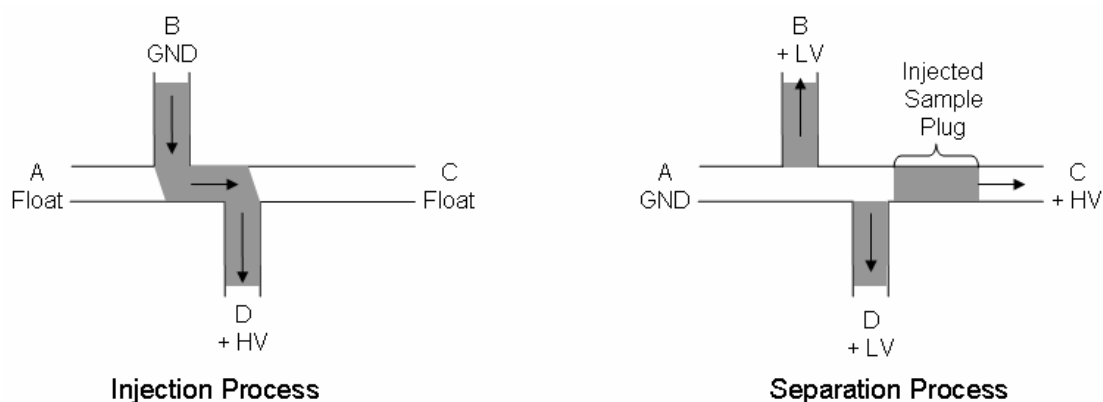
Figure 1-8: Schematic of injector "double-T" cross illustrating sample injection and separation process. LV refers to low voltage and HV refers to high voltage.

The DNA separation during microchip electrophoresis takes place through two separate voltage states, an "injection state" and a "separation" or "run" state, as shown in Figure 1-8. It is noteworthy that different architectures of the injection and separation channels exist, but the general process of DNA separation is similar (if not identical) for all available channel designs.
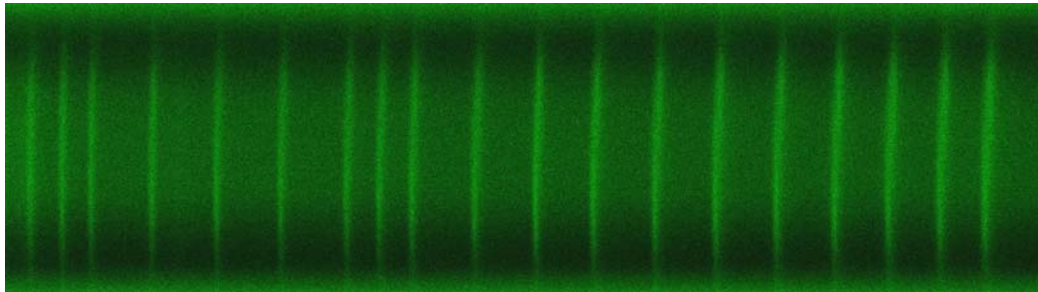
Figure 1-9: Fluorescence image of separated ssDNA fragments.

In the offset "double-T" injector region employed in this thesis work, sample is loaded into the reservoir (B) at one end of the injector. The electrokinetic injection takes place by an application of a positive voltage at the waste reservoir (D), which is at the opposite end of the injector channel. This forms a quasi-steady state flow of DNA within the injector (including the offset region). The reservoirs (A and C) at the opposite ends of the main separation channel are left to float during the injection state. The second

state of the separation process, the "run" state, begins when the voltages are switched to the cathode and the anode ends of the main separation channel. Small "pull back" voltages are applied at the reservoirs of the injector (B and D) to ensure that additional sample does not leak into the injector and that only the narrow plug of material at the intersection of the channels is injected into the separation channel. The resulting plug volume is on the order of picoliters, and can be carefully controlled – geometrically through fabrication, and electrically through proper application of voltages during the "injection" state. Fluorescence as a function of time is monitored at the end of the microchannel using optical detection system and an image (electropherogram) similar to the one shown in Figure 1-9 is used to analyze resolution and efficiency of separated DNA fragments.

For the successful development of microchip system for STR separations, a number of requirements must be fulfilled. For instance, the separation length must be designed to obtain sufficient single-base-pair resolution yet compact enough to minimize device footprint. The time required to complete the analysis should be kept lower than 30 min to outperform traditional capillary electrophoresis technology in terms of speed. To date, there have been several reports of separations of STR fragments in microfluidic devices [58-65]. The first use of plastic substrate for successful STR ladder separation was reported by Shi *et. al.* [62]. Their system comprised of polyolefin substrates, an effective separation length of 4.5 cm with a 100 μm offset "double T" injector and run temperature of 35 ˚C. Schmalzing and co-workers reported separation of STR fragments in glass microdevices with a cross injector and a run temperature of 50 ˚C [58, 59]. Some

groups have reported channel architecture that includes turn geometries to maximize channel lengths while keeping the absolute microchip footprint small [19, 60, 63, 64]. However, to the best of the author's knowledge, all of the reported STR separation systems with the exception of the one reported by Shi and co-workers [62] have employed glass substrates. It is likely that perhaps high-resolution separation techniques developed for DNA sequencing were adapted for forensic DNA separations. However, the use of these devices may not result in a truly disposable lab-on-a-chip system for forensic DNA analysis as glass substrate based device fabrication is complex and expensive.

1.6.   Goals and Organization of the Thesis

There are three major objectives of this thesis: the development and characterization of solvent-actuated bonding method for thermoplastic microfluidic devices, characterization of surface modification protocols for suppression of electroosmotic flow and prevention of analyte-wall interactions for enhanced separation of single stranded DNA, and theoretical assessment and data analysis of thin film coplanar waveguide (CPW) intended for use as a miniaturized heater for microfluidic heating applications.

The organization of the thesis is as follows:

- Motivation behind this research work and the need for microfluidics for forensic DNA analysis along with a brief overview of the analytical process steps involved in forensic DNA analysis are discussed thus far in this chapter. The techniques employed in this thesis work are also included in this chapter.

24

- *Chapter 2* presents an overview of the commonly used methods for bonding microfluidic devices. This chapter includes details of a new solvent-actuated bonding protocol developed and characterized in this thesis work for bonding thermoplastic microfluidic devices.

- *Chapter 3* defines the need for surface passivation of microchannels for microchip electrophoresis of ssDNA and presents comprehensive literature review of the passivation techniques used in microchannels. This chapter empirically compares new wall coating strategies investigated in this study for enhanced separation of ssDNA.

- *Chapter 4* examines the use of a thin film CPW for heating fluids in the microchannels. It presents detailed data analysis through development of analytical data analysis models and also describes efficiency of such transmission lines for heating applications.

- *Chapter 5* contains summary of this thesis work, and proposes future work for device bonding, surface passivation, and microwave dielectric heating.

1.7. Basic Techniques Employed in the Thesis

1.7.1. Microfluidic Device Fabrication

Microfluidic devices are typically fabricated out of silicon, glass, or polymeric (elastomeric and thermoplastic) materials. The choice of substrate material for microchip fabrication is application specific and depends on factors such as optical clarity, electrical conductivity, thermal properties, and chemical reactivity. The first reported microfluidic

devices were composed of silicon or glass and were fabricated using micromachining techniques adapted from the silicon microelectronics industry [22, 24, 66]. Silicon and glass devices are commonly used in microfluidics due to the well-understood fabrication techniques. However, the use of silicon in microfluidics has several drawbacks due, namely optical opacity, which inhibits the use of commonly employed optical detection techniques, and high electrical conductivity, which requires thick insulation layers for application of high electric fields. The beneficial optical properties, surface chemistry, and solvent compatibility of glass historically made it a substrate of choice, but the difficulties and costs associated with achieving small feature sizes and fluidic inlet drilling along with the limited selection of patternable fluidic structures, limits their usage, especially for low cost and disposable applications. Polymer microfabrication, although a relatively new field, is rapidly gaining popularity. Glass and silicon substrates are commonly used to generate the master from which these polymer devices are replicated.

Following substrate selection, microfluidic device fabrication can be divided into two parts – microchannel fabrication and microchannel enclosure. The current techniques for microchannel fabrication include conventional micromachining [67], soft lithography, hot embossing, in-situ construction [68], injection molding [69], and laser ablation [70]. The detailed emphasis here is placed on replication methods, which are used in this thesis work.

1.7.1.1. Microchannel Fabrication

Hot Embossing (Imprinting)
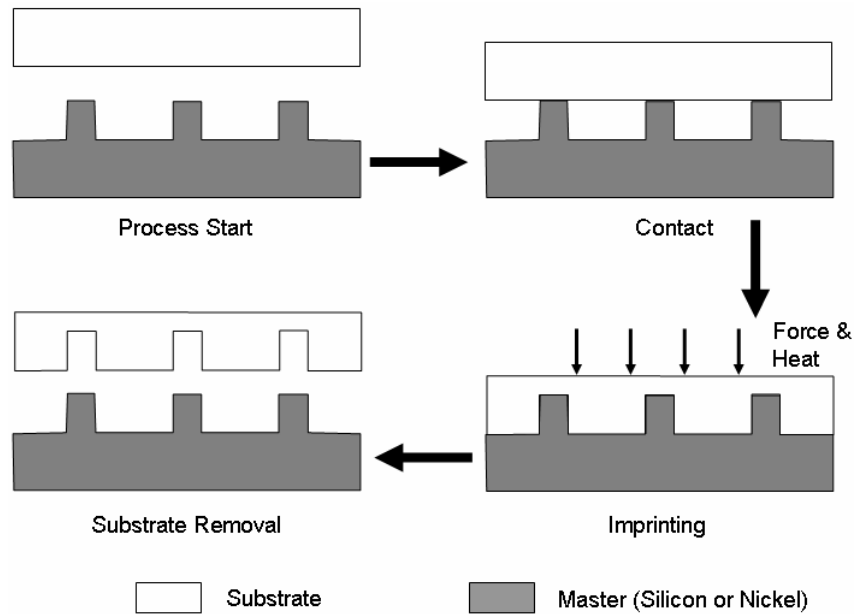
Figure 1-10: Schematic representation of hot embossing process.

Hot embossing is a method that can be used for patterning a large variety of thermoplastics, typically in the form of flat sheets.   Examples of some of the thermoplastics used in hot embossing include poly (methylmethacrylate) (PMMA), polycarbonate (PC), cyclicolefin copolymer (COC), polystyrene (PS), poly (vinyl chloride) (PVC), and poly (ethylene terephthalate) (PET).   The basic principle of embossing is that a polymer substrate is brought into conformal contact with a master containing negative of the desired pattern. The polymer substrate is heated near or above

its glass transition temperature (T_g). A master is then pressed against this substrate using pressure, fully transferring the pattern onto the substrate (Figure 1-10). After a certain time of contact between the master and the substrate, the master/substrate assembly is cooled down below T_g, which is followed by separation of the substrate from the master. The masters are typically made in silicon or metals. For forming masters in silicon, as mentioned above, silicon wafers are processed using micromachining techniques [71]. Metal masters are created using either electroplating against micromachined silicon masters or electroforms generated using the LIGA process [72]. LIGA is a German acronym for Lithographie (lithography), Galvanoformung (electroplating), Abformung (molding). The replication capability of embossing method is limited by the process used for fabrication of the master, and most embossed substrates are one layer planar structures.

Soft Lithography
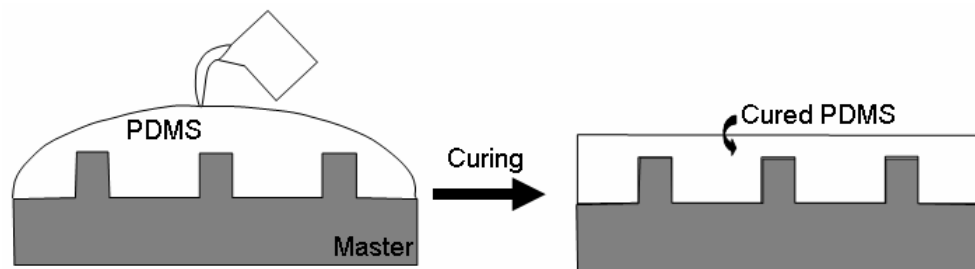
Figure 1-11: Schematic representation of soft lithography process.

Soft lithography is a process used to pattern elastomeric polymers, specifically poly (dimethyl siloxane) (PDMS). This process of molding a soft material from a

lithographic master was first developed at Bell Labs in 1974 [73]. Subsequently, several advances were made in Japan in the late 1980s that demonstrated micromolded microchannels for use in biological experiments [74]. Recently, the Whitesides research group at Harvard University has revolutionized the way soft lithographic techniques are used for the fabrication of microfluidic devices [75]. The common procedure used for making PDMS microchannels involves several steps (Figure 1-11): first, silicon or SU-8 master containing patterned features are fabricated. This is followed by pouring PDMS prepolymer, a two-component mixture of base and cross-linking agent, directly onto the patterned master. The PDMS prepolymer is then cured at a moderately elevated temperature (60 °C for approximately 2 hours) to replicate the desired features, which is then separated from the master. Soft lithography offers several advantages, including low cost and fast processing of microchannels.

1.7.1.2. Microchannel Sealing

Open microchannels have limited use in fluidic applications due to intolerance to pressure and evaporation of samples; hence, channel enclosure must be done as the following process step after microchannel fabrication. As with the fabrication of microchannels, a variety of methods exist for enclosure of microchannels. The selection of enclosure methods for silicon and glass microchannels include thermal bonding [25], electrically assisted anodic bonding [76], chemically assisted bonding [77], or adhesive bonding with polymers [78]. A detailed review of channel enclosure methods for polymeric substrates is provided in Chapter 2.

1.7.2. Principles of Fluorescence Microscopy

1.7.2.1. Laser-Induced Fluorescence Theory

Fluorescence microscopy is an excellent method to study materials that either fluoresce in their natural form (autofluorescence) or when they are treated with chemicals capable of fluorescing (secondary fluorescence). The fluorescence microscopy was devised in the early part of the twentieth century and today it is rapidly expanding and has become perhaps an indispensable tool in cellular and molecular biology.
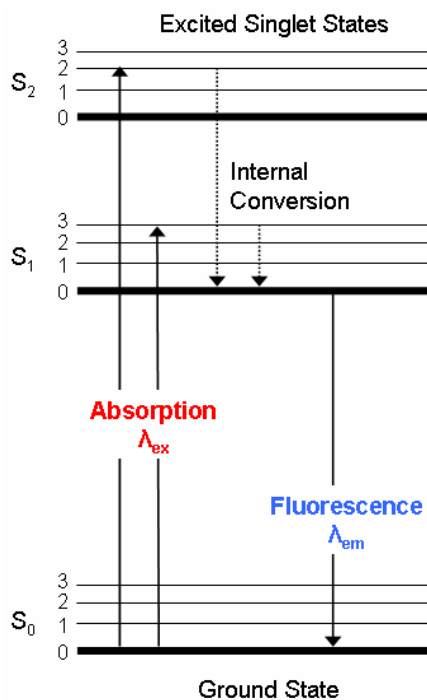
Figure 1-12: Modified Jablonski Energy Diagram. An incoming photon excites a susceptible molecule to a higher energy level (S_1 or S_2). Non radiative process, known as internal conversion, causes the molecule to relax to the lowest electronic energy level in

the first singlet state. After a finite interval, the molecule returns to the ground state and a fluorescence photon is emitted in the process.

Fluorescence results from a process that occurs when certain molecules, fluorescent probes, fluorochromes, fluorophores, or simply dyes absorb light. The absorption of light by these molecules raises their energy level to an excited state. After a brief interval, termed the fluorescence lifetime, they decay from this excited state, and emit fluorescent light. Lasers are commonly used for excitation due to their high irradiance at or near the exact energies required to excite the electrons of a particular molecule.

The various energy levels involved in the absorption and emission of light by a fluorophore are represented by a Jablonski energy diagram, shown in Figure 1-12 [79]. A typical Jablonski diagram illustrates the singlet ground (S_0) state, as well as the first (S_1) and second (S_2) excited singlet states. The thicker lines represent electronic energy levels, while the thinner lines represent the various vibrational energy states. When a molecule absorbs light, it is excited to a higher vibrational state, S_1 or S_2. The absorption of a photon of radiation happens in approximately femtoseconds. The molecule then quickly relaxes to the lowest vibrational level of S_1 through a process known as internal conversion. The rate at which vibrational relaxation of excited state electron to the lowest energy level happens is on the order of picoseconds. The excited molecule will subsequently relax from the lowest vibrational level of S_1 to any level within the ground state S_0 through the emission of a photon of light. This process is referred to as

31

fluorescence and takes on the order of nanoseconds. Some other relaxation pathways exist with varying degree of probability. For example, if the excited molecule collides with another molecule when relaxing to the ground state, transfer of energy takes places through a non-radiative process called 'quenching'.

1.7.2.2. Confocal Microscopy

The laser-induced confocal fluorescence is used to detect the DNA during microchip CE separations presented in Chapters 2 and 3. Confocal microscopy is a technique used to image a small area in the plane of focus as well as in the direction of focus at high resolution [80]. The basic idea of confocal microscopy is the use of spatial filtering techniques to remove out-of-focus light in specimens when the thickness of the specimen exceeds the plane of focus.
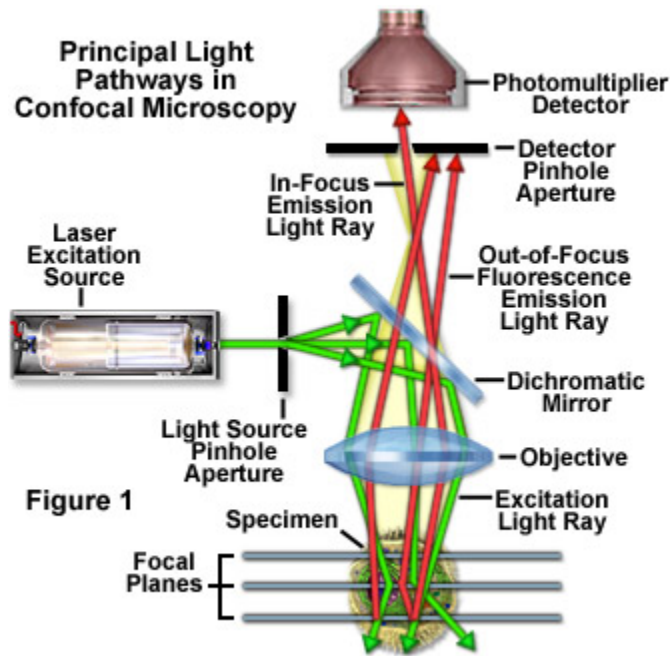
Figure 1-13: Confocal Microscopy setup employed for DNA detection during electrophoresis. Adapted from [81].

A schematic representation of a confocal fluorescence microscope is shown in Figure 1-13. A laser beam is used as an excitation source, which passes through a pinhole aperture. The light originating from an in-focus plane passes through the pinhole, whereas light coming from an out-of-focus plane largely gets blocked by the pinhole. The light coming from the pinhole is spectrally filtered and reflected from a dichroic beam splitter. A dichroic beam splitter has the property that it reflects one wavelength while transmitting others. It helps filter residual excitation light and facilitates the collection and excitation through the same microscope objective. The laser beam then enters the microscope objective, which focuses the laser beam onto a small spot on the sample. A fraction of the emitted fluorescence from the sample is collected

by the microscope objective and returned along the path of the incident beam onto the detector. The diameter of the pinhole in front of the detector determines the focal plane and rejects emitted rays that occur above and below the objective focal plane. The emitted light mostly from the sample focal plane is delivered through the pinhole aperture to a photodetector, a photomultiplier tube or a charge coupled device, resulting in very high vertical and lateral resolution providing three dimensional image and resolution.

1.7.3. Scattering (S) Parameter Measurements

Scattering (S) parameters are employed in Chapter 4 to analyze the performance and efficiency of CPW devices for micro-scale heating applications. S-parameters are measures of reflection and transmission of voltage waves through an N-port electrical network. They provide a complete description of the network as seen at its N ports. At microwave frequencies, as circuit size approaches the wavelengths of the operating frequencies, lumped-parameter models become inaccurate, and distributed circuit models and S-parameters are used to predict the behavior of components, circuits, and systems. For some components and circuits, the S-parameters can be calculated using network analysis methods; otherwise, the S-parameters can be measured directly with a vector network analyzer. For an N-port network, where V_n^+ is the amplitude of the voltage wave incident on port n, and V_n^- is the amplitude of the voltage wave reflected from port n, the scattering matrix is defined as

$$\begin{bmatrix} V_1^- \\ V_2^- \\ \vdots \\ V_N^- \end{bmatrix} = \begin{bmatrix} S_{11} & S_{12} & \cdots & S_{1N} \\ S_{21} & S_{22} & \cdots & \vdots \\ \vdots & & & \\ S_{N1} & \cdots & & S_{NN} \end{bmatrix} \begin{bmatrix} V_1^+ \\ V_2^+ \\ \vdots \\ V_N^+ \end{bmatrix} \qquad (1\text{-}5)$$

where S_{ij} is found by driving port j with an incident wave of voltage V_j^+, and measuring the reflected wave amplitude, V_i^-, coming out of port i. Here, S_{ii} is the reflection coefficient seen looking into port i when all other ports are terminated in matched loads, and S_{ij} is the transmission coefficient from port j to port i when all other ports are terminated in matched loads [82].

2. Capillarity Induced Solvent-Actuated Bonding of Polymeric Microfluidic Devices

As mentioned in Chapter 1, microfluidic devices are typically fabricated out of glass, silicon, polymers (elastomers and thermoplastics), or some combination of these materials [22, 57, 83, 84]. In the early 1990s, when the concept of μ-TAS ("miniaturized total analysis system") was first introduced, microfluidic devices were fabricated on a silicon wafer using standard lithographic and wet chemical etching procedures developed for the semiconductor industry [85]. However, the conductivity of silicon had proved problematic for the high electric field required for electrokinetic pumping for transporting liquid samples [86]. Then the development of microdevices focused on various type of glass substrates [87], primarily because the fabrication methods were similar and the chemistry of glass surfaces was well understood by the chromatography industry. However, there are certain disadvantages associated with the use of glass materials, such as high substrate cost, complex multi-step fabrication process that required the use of clean room facility, harmful chemicals used for wet chemical etching, and limitations in geometrical design posed by chemical etching procedures.

On the other hand, polymeric materials because of their reduced cost and simplified manufacturing procedures are rapidly gaining popularity as substrate material for microfluidic applications. Thermoplastics, such as PMMA, PC, PS, and PET, have functional material properties between those of glass/silica and elastomeric materials, and

exhibit low autofluorescence as well as good visible and near-UV transparency for optical detection strategies. These materials often have moderate Young's modulus and result in devices of mechanical robustness between that of glass/fused silica and more compliant elastomeric materials such as PDMS, which makes them suitable for applications requiring moderate operating pressures. However, one major challenge for thermoplastic devices is the availability of reproducible bonding techniques that are simple and cost effective to implement at room temperature.

2.1. Thermoplastic Microfluidic Device Bonding Background

Typically, thermoplastic microfluidic devices are bonded together by thermal welding; *i.e.*, placing them in contact under moderate pressure and incubating at a temperature near the polymer's glass transition temperature, Tg [88-91]. Heating the polymer interface to a temperature that is near its Tg causes the polymer chains on the surface of two substrates to interdiffuse, and cooling the assembly strengthens the bond [92]. The fabrication parameters, such as temperature, pressure, and time, are empirically tuned based on the properties of the thermoplastic in use and the equipment used for the process. Even though this general technique yields functional devices, lot-to-lot variability in the plastic and implementation of the process on new equipment requires the fabrication protocol to be fine-tuned for each lot [93] and for each bonding tool.

Solvent bonding of polymeric substrates is another widely used alternative to thermal welding. The contact surfaces of the polymer substrates are treated with a suitable solvent, and, after a short time, the two surfaces are brought into contact and clamped together under pressure. The solvent solubilizes the surface of the polymeric

material which facilitates the polymer chains of the two surfaces to interdiffuse at the interface while clamped together [94]. To date, there have been numerous reports on solvent bonding of polymeric substrates [95-99]. Liu *et. al.* [100] have reported solvent-assisted thermal bonding of PC substrates. They applied acetone on one side of the cover layer, which, after 1 min, was bonded to the substrate layer at 1.5 MPa of applied pressure and 196 ℃ temperature for 2 min. Other groups have introduced various bonding procedures that employ capillary forces to draw adhesives (either epoxy resin [101, 102] or UV curable adhesives [103]) from reservoirs adjacent to the microfluidic channel, requiring optimization of the gap between the two plates to be bonded.

More recently, Kelly *et. al.* [104] used a phase-changing sacrificial material (paraffin wax) for solvent bonding of PMMA substrates using acetonitrile as a bonding solvent. Their approach involves filling the unbonded microfluidic channel with wax prior to applying the bonding solvent at the contact surface. This prevents the solvent and softened PMMA from potentially occluding the microchannel. After bonding, the device is heated to melt the sacrificial wax layer, which is subsequently removed by application of vacuum and dissolution in cyclohexane. This technique allows solvent bonding of plastic devices with small channel dimensions while protecting the channel integrity, but requires the application and removal of the sacrificial layer which complicates the fabrication process and could potentially alter the chemical properties of the microfluidic channel surface.

The focus of this chapter is to develop and characterize a rapid solvent-actuated bonding technique for PMMA substrates at room temperature. This technique takes

advantage of the difference in capillarity of the microfluidic channel and the interstitial space between the surfaces of the two substrates to wick the bonding solvent into the gap between the substrates allowing them to bond. The technique is implemented by placing the two substrates under moderate pressure and applying a moderate pneumatic vacuum to the fluidic channel. Tens of microliters of solvent is applied to one end of the channel while a vacuum line is connected at the opposite end. The solvent then rapidly flows through the channel into the aspirator. As the solvent flows through the channel, capillary forces draw a small amount of solvent between the two substrates where it softens the surfaces causing the polymer chains to interdiffuse, resulting in bond formation. The effect of bonding solvent on the dimensions of the microchannel is carefully studied throughout the fabrication process, and the mechanical robustness of the bonded devices is also characterized. The importance of the quality of the bonding solvent for successful bond formation is shown and electrophoretic separation of single-stranded DNA (ssDNA) are performed to demonstrate the functionality of these devices.

2.2.   Materials and Methods

2.2.1. Materials and Reagents

Silicon wafers were obtained from Virginia Semiconductor (Fredericksburg, VA). PMMA (Vistacryl CQ) in 1.7 mm thickness was obtained as a sheet from Vista Optics (Widnes Cheshire, UK). PDMS (Sylgard 184) was obtained from Dow Corning (Midland, MI) and mixed and cured according to the manufacturer's specifications. A 70-base to 400-base ssDNA ladder containing 20 fragments was obtained from

BioVentures Inc. (Murfreesboro, TN) and was used as received without any pretreatment for sample preparation. Hydroxypropyl methylcellulose (HPMC; viscosity ~ 4 cP, MW_z 4.47×10^5) and sulforhodamine were obtained from Sigma-Aldrich Inc. (St. Louis, MO). Acetone (ACS grade) and nitric acid were obtained from Fisher Scientific (Pittsburgh, PA). Acetone was dried using 40 nm (4 Å) molecular sieves obtained from Fisher Scientific International Inc. (Hampton, NH). 1 × TTE [50 mmol/L tris(hydroxymethyl)aminomethane (Tris), 50 mmol/L N-tris(hydroxymethyl)methyl-3-aminopropane-sulfonic acid (TAPS), 2 mmol/L ethylenediaminetetraacetic acid (EDTA)] with 7 mol/L Urea was used as background electrolyte for the polymer and as an electrode buffer. A fast setting epoxy was obtained from Elementis Specialties, Inc. (Belleville, NJ).

2.2.2. Microchannel Fabrication
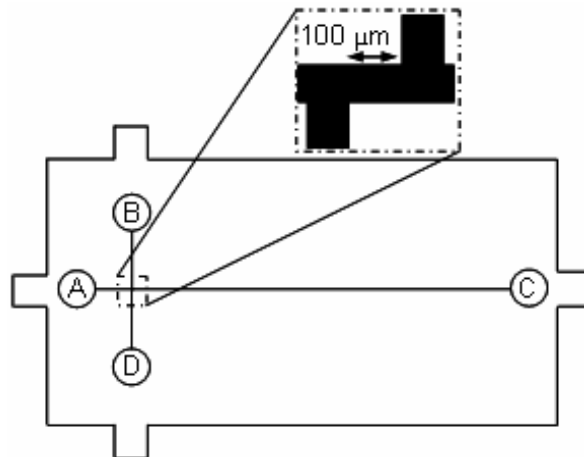
Figure 2-1: Schematic layout of polymeric thermoplastic microchip. The device geometry is rectangular with four rectangular tabs used for gross device alignment to high-voltage electrodes and optical detection system. The 100-μm offset "double-T"

injector region is shown in the figure inset. The PMMA substrate is 8.6 cm x 4.7 cm x 0.17 cm, channel A is 0.25 cm long, channels B and D are 0.7 cm long, separation channel is 7.7 cm long (effective separation length is 7.4 cm), and the fluidic wells are each 0.3 cm in diameter. The rectangular alignment tabs are 0.5 cm x 0.4 cm.
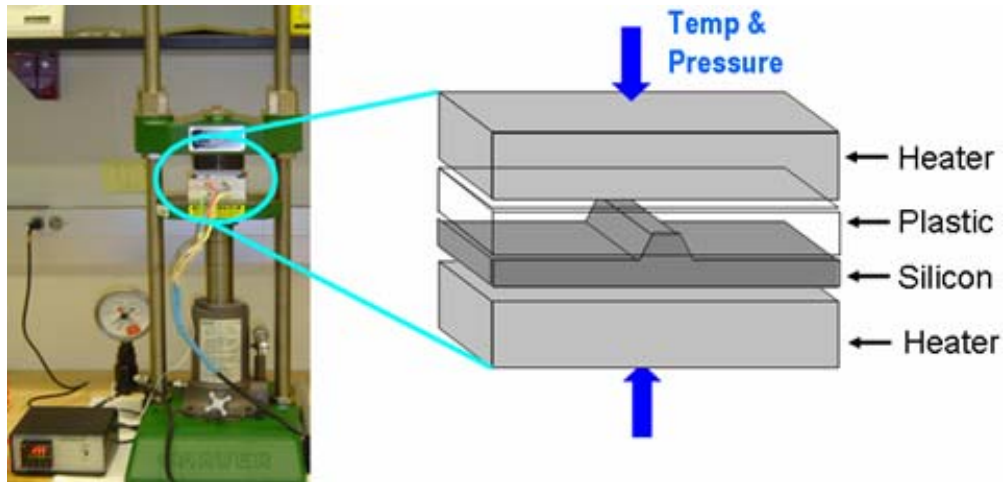
Figure 2-2: PMMA microchannel hot embossing (imprinting) process. Left panel shows a photograph of a hydraulic press used for hot embossing. Right panel shows expanded view of the silicon master/PMMA/Aluminum heater assembly used for microchannel imprinting.

A schematic of the device fabricated in this study is shown in Figure 2-1. Microfluidic channels were fabricated by hot embossing patterns into PMMA substrates using photo-lithographically patterned silicon masters similar to the procedures previously published [105]. The details regarding silicon master fabrication can be found in Appendix 1. Briefly, a 10.64 μm wavelength CO_2 laser (Synrad Inc., Mukilteo, WA) was used to cut the substrate material (PMMA sheet) to precise chip dimensions of 8.6 cm x 4.7 cm and to create fluidic access wells. The PMMA blank was then rinsed with

ethanol and dried under nitrogen. Next, the laser-machined substrate was aligned over a silicon master template (as seen in Figure 2-2) to ensure that the fluidic access ports coincided with the raised structures on the silicon template at desired locations. The PMMA/silicon template assembly was then placed between two custom-built aluminum blocks with embedded heaters connected to a temperature controller. Subsequently, the final assembly was mounted in a hydraulic press (Carver Inc., Wabash, IN), and the temperature was increased to 105 °C. Figure 2-2 shows a photograph of the assembly in the hydraulic press. Once the assembly reached the desired temperature (105 °C), the pressure was increased to 5.5 MPa. After approximately 30 min, the temperature was reduced to 80 °C before releasing the pressure. The PMMA/silicon template assembly was then removed from the aluminum heaters and allowed to cool to the room temperature.

2.2.3. Solvent-Actuated Microchannel Bonding
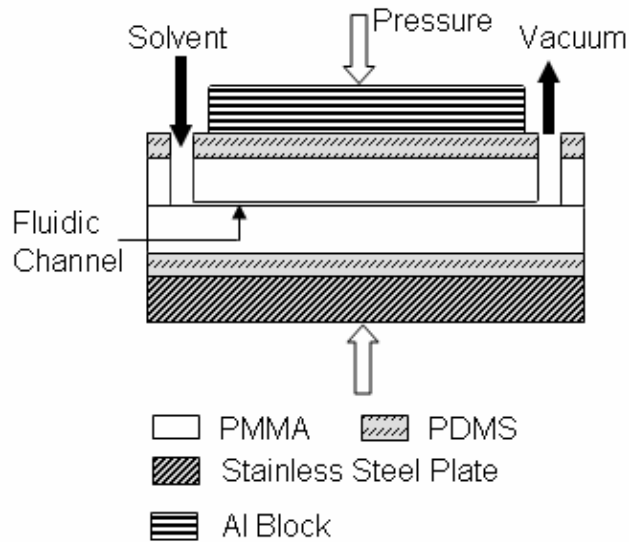
Figure 2-3: Solvent-actuated bonding assembly for the fabrication of a polymeric thermoplastic microfluidic device at room temperature. The assembly is held together under applied pressure of 1.1 MPa (160 psi). Acetone is introduced into well A and aspirated through the microchannel network by application of vacuum at well C (Figure 2-1). Wells B and D are left open to the atmosphere.

A clean, flat PDMS sheet was attached by contact adhesion to the bottom side of the PMMA cover plate and then placed on a stainless steel plate as shown in Figure 2-3. Another clean PDMS piece with access ports cut at appropriate locations to contact the fluidic access wells was attached to the unpatterned side of the imprinted PMMA substrate. The two PMMA assemblies were then brought into conformal contact and an aluminum block was placed on top of the PDMS piece with access ports (holes) to provide syringe and vacuum line access to the fluidic wells. Next, the assembly was held together using a hydraulic laboratory press at a pressure of 1.1 MPa. A vacuum line was

43

conformably attached to one end of the PDMS manifold (reservoir C) to draw air through the microfluidic channel, while slowly supplying the other end (reservoir A) of the fluidic channel with acetone. Reservoirs B and D were left open to the atmosphere. A total of 80 µL ± 5 µL of acetone was delivered drop by drop to the fluidic channel with a needle and syringe over a period of 2 min to 3 min. Thereafter, the device remained under pressure for approximately 5 min. The outside edges of the device were then sealed by applying a small amount of acetone, approximately 5 µL to 15 µL, at the interface between the two pieces of plastic and incubating the device at 1.1 MPa for approximately 5 min. The assembly was then removed from the press, and the PDMS pieces, the aluminum block, and the steel plate were removed from the device for further use.

2.2.4. Characterization of Silicon Template and Imprinted Microchannels

A Scanning Electron Microscope (SEM) (Hitachi S-4700, Brisbane, CA) and an optical interferometer (Optical Profiler, WYCO Corp., Tuscon, AZ) were used to examine various sections of the silicon template and imprinted microchannel. The dimensions of the raised structures in silicon and recessed structures in PMMA made by hot embossing were obtained by two-dimensional interferometry. The channels imprinted in PMMA by hot embossing were coated with 3 nm of titanium and 25 nm of gold using a high vacuum thermal evaporator (Denton DV-502A) and were then imaged using the SEM. The titanium/gold deposition was carried out to make the thermoplastic surface conductive in order to facilitate SEM imaging. Cross-sectional views of

imprinted channels were obtained using a phase contrast microscopy of microtomed sections of the microfluidic channel.

2.2.5. Characterization of Bonded Devices

To characterize the physical dimensions of the microchannels in the bonded devices, the microchannels were filled with a mixture of sulforhodamine dye and epoxy using a custom built gasket and jig and an applied pneumatic pressure differential of 345 kPa (50 psi). A hydraulic press was used to hold the gaskets and jig around the bonded device, allowing it to withstand large pneumatic pressure. Once the epoxy had cured, the sealed devices were cut using a microtome, and the resulting slices were imaged using a fluorescence optical microscope.

2.2.6. Bond Strength Determination

A hole was drilled and tapped into a Plexiglas cube to accept a brass fitting. The threaded piece was glued with toluene based acrylic cement to a solvent-bonded device such that the fluidic well C (in Figure 2-1) was aligned to the threaded hole. The wells A, B and D were filled in and sealed using epoxy. A brass fitting was then screwed into Plexiglas/PMMA device assembly, which connected the assembly to a N_2 gas cylinder via copper tubing. The regulator on the gas cylinder was gradually opened to pressurize the channel until the two PMMA substrates separated.

2.2.7. Microchip DNA Electrophoresis

All electrophoretic separations were conducted on the stage of a confocal laser-induced fluorescence microscope (Carl Zeiss MicroImaging, Inc., Thornwood, NY). A schematic of the confocal setup is shown in Figure 1-13. Specifically, excitation of the fluorescein labeled ssDNA was achieved by using 488 nm line of 30 mW Argon ion laser. A laser beam was focused approximately 4 mm from the end of the separation channel using a 20x, 0.4 NA objective. Fluorescence as a function of time at the end of the channel was monitored through a 505 nm long-pass filter and a photomultiplier tube. A high voltage power supply (HV488, LabSmith, Livermore, CA) was used to provide voltages from 0 V to 1500 V.

The microchannel was rinsed with 40 % nitric acid, followed by deionized ultra-filtered H_2O and then with 0.5 % (w/v) solution of HPMC dissolved in deionized water to adsorb a layer of HPMC on the channel surface and to minimize electroosmotic flow (EOF) and nonspecific interactions of the analyte with the channel wall. A solution consisting of 2.75 % (w/v) 5 × Nanogel (a polyacrylamide architecture) [106, 107] and 0.25 % (w/v) linear poly(acrylamide) (LPA; MWz ~ 638 kDa) dissolved in 1 × TTE with 7 mol/L urea was used as a sieving matrix and filled into the microchannel through reservoir C (Figure 2-1) using a hydraulic laboratory press with a custom-built jig and gaskets with an applied pressure differential of 345 kPa. Reservoir A was filled with sieving matrix, reservoir B was filled with sample, and reservoirs C and D were filled with buffer prior to analysis. Sample injection was accomplished by applying +400 V at reservoir D while keeping reservoir B at 0 V for 60 s (reservoirs A and C were left

floating during the injection), for an effective electric field of 285 V/cm. Sample separation was performed at room temperature by applying +1500 V to reservoir C, +160 V to reservoir B, and +170 V to reservoir D, while applying 0 V to reservoir A, for an effective electric field strength during separation of 190 V/cm. Resolution was obtained by fitting raw ssDNA separation data into Gaussian peaks using PeakFit v4.06 (SPSS Inc., Chicago, IL). Separation efficiency, η, (plates/m) was calculated according to Eq. (2-1):

$$\eta = \frac{N}{L} = \frac{t^2}{L \cdot (FWHM / 2.35)^2}$$

(2-1)

where N is the number of theoretical plates, L is the migration distance in meters, t is the migration time in seconds, and $FWHM$ is full temporal width of the peak at half maximum [108].

2.3. Results and Discussion

Figure 2-3 shows the fabrication assembly for solvent-actuated bonding of the PMMA substrates. Using PDMS, an elastomeric material, as a gasket on the top and bottom of the PMMA substrates allows for even distribution of pressure across the surface. During solvent application, a vacuum line was connected to the fluidic channel, and the assembly was kept under constant pressure. Under these conditions, the plug of acetone moved rapidly through the fluidic channel, and the capillary forces drew small amounts of acetone laterally into the interstitial spaces between the two PMMA

substrates. The acetone softened the PMMA interface causing interdiffusion of polymer chains resulting in bond formation within 5 min.

The acetone that was not drawn between the plastic pieces was quickly evacuated from the microfluidic channel into the vacuum line. It was observed as a result that there was insufficient time for the solvent to plasticize and deform the channel features. Results of this work show that this technique, thus, obviates the need for sacrificial materials to protect the channel during solvent-assisted bonding because rapid and residue-less evacuation of the acetone from the channel in the present work preserves the channel integrity.
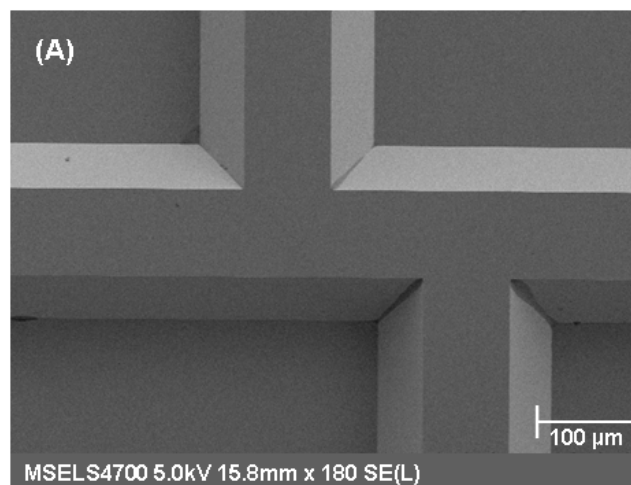
(Please see next page for figure caption.)
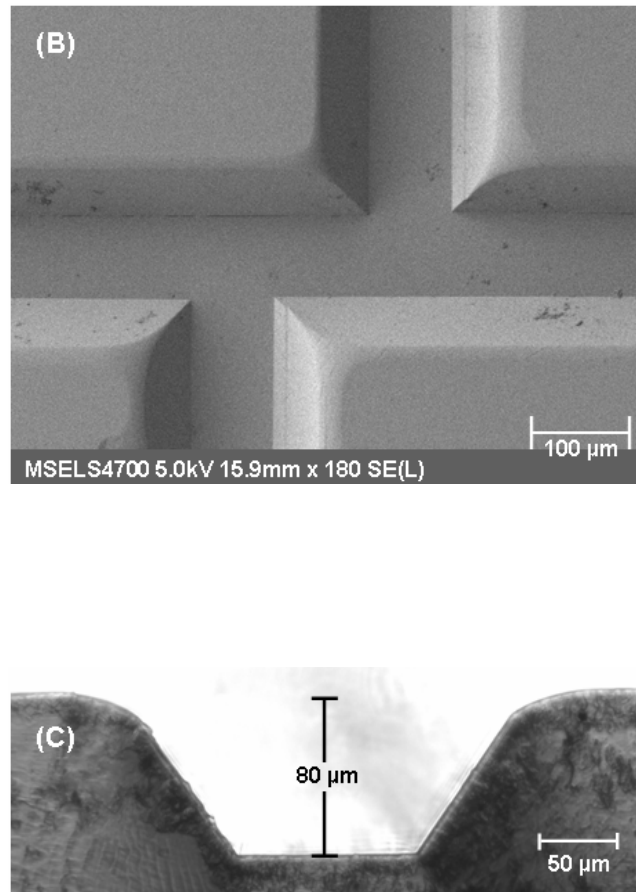
Figure 2-4: Characterization of imprinted microchannel in PMMA. (A) Top view SEM of a silicon template micromachined using photolithography and subsequent anisotropic wet chemical etching (scale bar, 100 μm). (B) Top view SEM of an exposed embossed channel fabricated in PMMA substrate (scale bar, 100 μm). (C) Phase contrast micrograph of a microtomed slice of an unbonded channel fabricated in PMMA (scale bar, 50 μm).

The SEM micrograph of a double–T injector region of the silicon template is shown Figure 2-4A, and the SEM micrograph of the same region imprinted into PMMA is shown in Figure 2-4B. The height of the raised structure in the silicon was measured to be 79 μm. The channel structure in the Si template was well defined, and the embossed channel surfaces in PMMA appeared smooth. However, the corners at the intersection of

the embossed microchannels appeared rounded. This may be because the imprinting time did not exceed required creep time in PMMA at the imprinting temperature and pressure. A cross-sectional view of the imprinted channel is shown in Figure 2-4C. The depth of the recessed structure in PMMA was measured to be 80 μm. The slight asymmetry of the channel walls seen in the figure may have been caused by uneven distribution of pressure or temperature during imprinting.
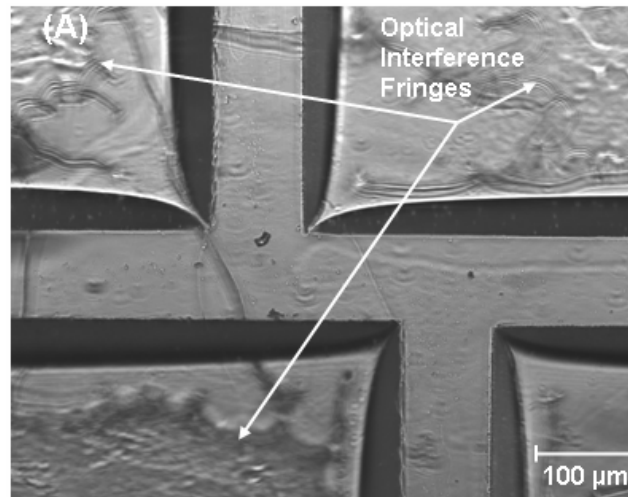
(Please see next page for figure caption.)
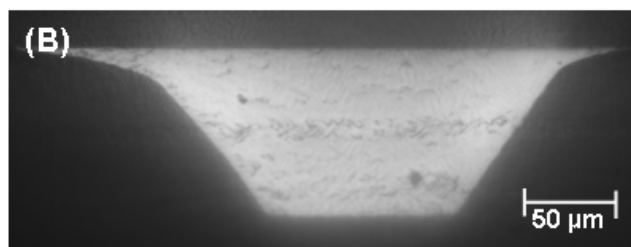
Figure 2-5: Characterization of a solvent-bonded channel. (A) Optical micrograph of the offset double-T injector of a typical polymeric microfluidic device bonded using the solvent-actuated bonding technique (scale bar, 100 μm). (B) Cross-sectional fluorescence micrograph of a microtomed slice of polymeric solvent-bonded microfluidic channel in PMMA that was filled with sulforhodamine dyed epoxy (scale bar, 50 μm).

An optical micrograph of the double-T injector region of a solvent-bonded device is shown in Figure 2-5A. As can be seen by the optical interference fringes, the bond formation was effective in immediate areas adjacent to the channel. The lateral distance penetrated by the solvent into the interstitial spaces between the PMMA substrates was measured to be 0.5 mm at minimum to 6 mm at maximum as evident by the presence of the optical interference fringes. Putatively, this distance depends on the surface roughness, surface cleanliness, and the applied force holding the substrates in contact. However, we suspect that unbonded areas may not occur on parallel multi-channel devices where the channel pitch is smaller than the solvent penetration distance.

A cross-sectional view of a solvent bonded device is shown in Figure 2-5B. The depth of the channel in the bonded device was measured to be 81 μm, which was in agreement with that of the silicon template and embossed channel and well within the tolerances expected from the differences in linear thermal expansion coefficients between Si and thermoplastics. Qualitative examination of the enclosed channel via microscopy

51

of the cross-section indicated that the channel dimensions were well preserved and there was no further distortion around the corners at the intersection of channels when compared to the embossed microchannel. Microscopic inspection of the separation channel at the detection end where the bonding solvent is drawn also indicated that there was no observable degradation of the channel features.

Bond strength determination of these devices indicated that the solvent-bonded PMMA devices regularly withstood internal pressure greater than 552 kPa (80 psi). Although the failure pressure of devices made by solvent-actuated bonding is low when compared to the failure pressure of glass [109] and silica microfluidic devices, it is sufficiently robust to allow loading and replacement of viscous sieving matrices typically used for electrophoretic DNA separations (data not shown). It seems that the solvent-actuated bonding technique is less susceptible to lot-to-lot variability in plastic materials in producing high device bond integrity than thermal bonding (data not shown).

The quantity, the water content, and the residence time of the acetone in the microchannel as well as adequate suction were found to be important parameters for this fabrication technique. Total occlusion of the channels was observed with excessive acetone, poor suction, or with acetone that had been rigorously dried. On the other hand, wet acetone, allowed to equilibrate with room humidity (91 % relative humidity), results in very weak or no bond formation. Rigorously dry acetone rehydrated with 0.001 % (v/v) to 0.0015 % (v/v) water was found to be optimal for effective bond formation while preserving the channel integrity. It was also observed that the drop of solvent left in the

channel for longer than two to three seconds, dissolved the plastic and resulted in deformed channels.

The functionalities of solvent-bonded microfluidic devices were assessed by performing ssDNA separation. The electrophoretic separation of the ssDNA ladder performed in solvent-bonded devices resulted in rapid separation with high efficiency and good resolution. The electrophoresis conditions (injection and separation voltages) are shown in Table 2-1.

Table 2-1: The injection and separation voltages for electrophoretic separation of ssDNA.

Step	Potential (V)			
	A	B	C	D
Injection	Float	0	Float	400
Separation	0	160	1500	170
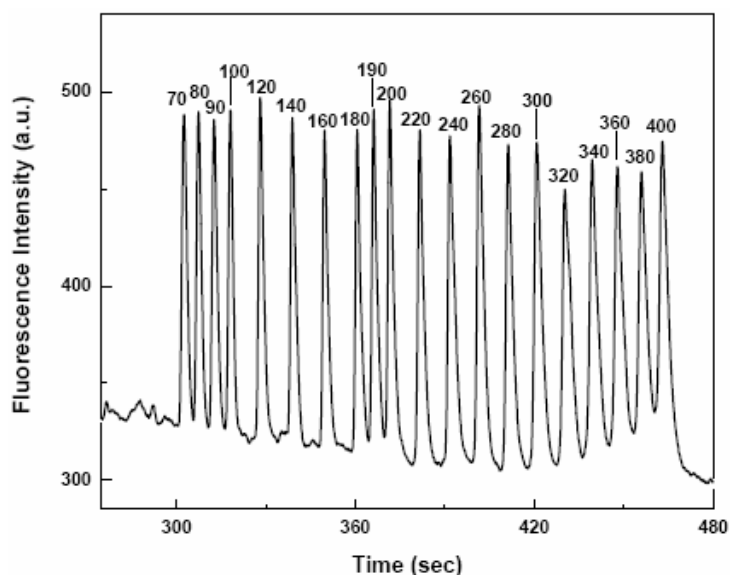
Figure 2-6: Electropherogram showing the separation of 20-base ssDNA ladder in a solvent-bonded polymeric microfluidic device performed at room temperature. Electrophoretic conditions: injection field, 285 V/cm; separation field, 190 V/cm; separation buffer matrix, 2.75% 5x Nanogel + 0.25% LPA (MW ~ 638 000) in a 1x TTE with 7 mol/L urea buffer.

Figure 2-6 shows a representative electropherogram of the separation of a 20-base ssDNA ladder. The number above each peak specifies the size of DNA that produced that peak. Peak efficiencies ranged from 1.15×10^6 plates/m to 3.38×10^6 plates/m with lowest efficiencies observed for large molecular weight DNA fragments. Resolution normalized to the difference in fragment size ranges from 0.155 base^{-1} to 0.048 base^{-1}. The average separation efficiency and resolution for two different runs are summarized in Table 2-2.

Table 2-2: Average efficiency, η (a), and resolution, $\mathscr{R}$ (b), of microfluidic electrophoretic ssDNA separation (n = 2). Electrophoresis conditions are given in Table 2-1.

(a)		(b)	
Fragment size (bases)	η (x 10^{-6}) (plates/m)	Fragments (bases)	Resolution
70	1.85	70/80	1.31
80	2.19	80/90	1.44
90	2.11	90/100	1.44
100	2.68	100/120	2.87
120	2.60	120/140	2.95
140	2.59	140/160	2.98
160	3.38	160/180	3.11
180	3.34	180/190	1.49
190	2.96	190/200	1.37
200	2.74	200/220	2.52
220	2.92	220/240	2.44
240	2.56	240/260	2.11
260	2.49	260/280	2.09
280	2.46	280/300	1.87
300	1.86	300/320	1.67
320	1.65	320/340	1.49
340	1.62	340/360	1.30
360	1.42	360/380	1.16
380	1.42	380/400	0.96
400	1.15		

The promising efficiencies achieved from ssDNA separations indicate that separation performance was not limited by the bonding method. The data presented here show that CE separations were mostly limited by the finite width of the injection plug,

and thus CE separations close to theoretical limits can be obtained on polymeric microchips fabricated using this bonding method. This bonding technique can also be used for fabrication of polymeric materials other than PMMA, when a solvent of appropriate polarity is selected. The quantity and the water content of the solvent can be controlled in an automated environment in which case the mass production of polymeric devices can result in high yields.

2.4. Conclusions

This chapter presents a solvent-actuated bonding technique for fabrication of polymeric thermoplastic microfluidic devices. This technique is inexpensive, simple, rapid, and produces bonded plastic devices capable of withstanding internal pressures of greater than 552 kPa (80 psi). The quantity and the water content of the solvent and the rate of acetone flow were found to have significant effects on the bond formation and the resulting microchannel dimensions on the devices fabricated using this method.

Solvent-actuated devices produced rapid electrophoretic separations of ssDNA up to 400 bases in length in less than 8 min with efficiency regularly exceeding 2×10^6 plates/m. Finally, this technique is affected less by lot-to-lot variation in plastic properties than thermal bonding and does not require the use of sacrificial layers, which may impact the surface properties of the microfluidic device. The simplicity of the solvent-actuated bonding technique should make it conducive for adaptation to a mass production environment.

3. Surface Modification of PMMA for Improved Adsorption of Wall Coating Polymers for Microchip Electrophoresis

3.1.   Introduction

In microfluidic devices, hydrophobic, electrostatic, or other interactions can cause undesired, nonspecific analyte adsorption onto the microchannel walls leading to asymmetry in analyte zones, increased peak widths, and sample loss [110]. The changes in the surface due to analyte adsorption from the running buffer can create a nonuniform distribution of the ζ-potential over the length of the microchannel. This results in nonuniform liquid flow profiles and local variation of electroosmotic flow (EOF), leading to additional band broadening and poor reproducibility of electrophoretic separations [111, 112]. Therefore, the development and optimization of surface coating strategies is of crucial importance for reliable, repeatable, and high-efficiency electrophoretic DNA separations [113, 114].

Conventionally, inorganic substrates such as glass and silica have been used for the fabrication of microfluidic devices, and numerous silane-based chemistries originally developed to passivate fused-silica capillary surfaces were relatively simple to transfer to silica-based microfluidic devices [115]. However, the devices made from glass and silica substrates are not as economical as polymeric microfluidic devices for mass production. Moreover, the low-cost of mass manufactured polymeric microfluidic devices could make the production of microfluidic devices feasible for applications in which cross

contamination can yield unacceptable results (*i.e.* single-use disposable devices) [116, 117].

The development of robust and simple surface modification techniques for polymeric substrates is challenging due to the wide variety of polymeric materials available for microfluidic device fabrication. To date, there have been numerous reports on surface modification techniques of various polymer surfaces, such as UV/ozone graft polymerization [118], graft copolymerization [119], laser activation [120], vacuum UV irradiation [121, 122], oxygen plasma treatment [75, 123], and ion bombardment [124]. Henry *et al.* [125] have demonstrated chemical modification of PMMA substrates *via* aminolyses of surface esters to yield amine-terminated PMMA surfaces. The same group also studied chemical modification of PC surfaces by treatment with sulfur trioxide gas, yielding hydrophilic sulfonated surfaces [126, 127]. Further, Johnson *et al.* [128, 129] reported that the surfaces of PMMA microchannels can be modified by pulsed UV excimer laser irradiation (KrF, 248 nm) resulting in carboxylate groups at the PMMA surface. Although considerable work has been carried out on the modification of various polymeric materials, simple, fast, and automatable techniques that enable high efficiency biopolymer separations in microfluidic devices have yet to be fully developed.

In this study, a few methods for the application of wall coating polymers to PMMA microchannels are characterized and compared. Even though experiments shown here explore a subset of the PMMA and coating polymer parameter space, the results identify several important parameters of the coating polymer protocols necessary to improve the aggregate separation performance. Specifically, the PMMA microchannels

58

were (i) flushed with an aqueous solution of poly(diethylacrylamide-co-dimethylacrylamide) (40 mol% diethylacrylamide and 60 mol% dimethylacrylamide) (40DEA-60DMA), and (ii) oxidized with an aqueous solution of HNO$_3$ or UV/ozone, and subsequently flushed with an aqueous solution of the coating polymer, hydroxypropyl methyl cellulose (HPMC), or poly(vinyl alcohol) (PVA).

Contact-angle measurements of the pristine and modified PMMA substrates are performed to quantify the change in wettability of the surface. High-efficiency electrophoretic separations of 20-base ssDNA ladder are demonstrated in the modified PMMA microchannels. By performing a comparative study among different methods, the importance of surface preparation and coating polymer on separation efficiency is highlighted. In addition, it is also shown that by optimizing the wall coating, significant increases in theoretical plate counts can be achieved. The methods presented in this chapter are rapid, facile, and can be performed in air or aqueous environments at room temperature. Therefore, these methods are amenable to automation, mass production and conducive to implementation in integrated microfluidic platforms.

3.2. Materials and Methods

3.2.1. Materials and Reagents

Silicon wafers were obtained from Virginia Semiconductor (Fredericksburg, VA). PMMA (Vistacryl CQ^{TM}, 1.7 mm thick) was obtained from Vista Optics (Widnes Cheshire, UK). PC (125 μm thick) was obtained from McMaster-Carr (Dayton, NJ). A

70-base to 400-base fluorescein-labeled ssDNA ladder containing 20 fragments was obtained from BioVentures Inc. (Murfreesboro, TN). HPMC (viscosity 4 cP) and PVA (87-89% hydrolyzed, average Mw = 31,000 g mol^{-1} to 50,000 g mol^{-1}) were obtained from Sigma-Aldrich Inc. (St. Louis, MO). HNO$_3$ and H$_3$PO$_4$ were obtained from Fisher Scientific (Pittsburgh, PA) and used for oxidation of the microchannel surface. TTE [89 mmol L^{-1} tris(hydroxymethyl)aminomethane (Tris), 89 mmol L^{-1} N-tris(hydroxymethyl)methyl-3-aminopropane-sulfonic acid (TAPS), 2 mmol L^{-1} ethylenediaminetetraacetic acid (EDTA)] with 7 mol L^{-1} urea was used as background electrolyte for the polymer and as an electrode buffer. Biaxially oriented poly(propylene) (BOPP), 12-μm thick, coated on one side with a 15-μm thick adhesive made of low density poly(ethylene)/ethylene vinyl acetate (LDPE/EVA) co-polymer resin was used as the laminating film for enclosure of microchannels and was obtained from Morane Ltd. (Oxfordshire, UK).

3.2.2. Microchip Fabrication

(a)

(b)
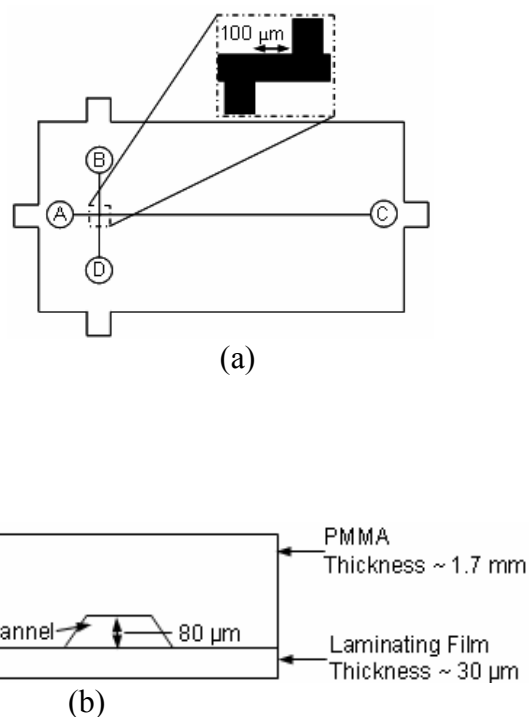
Figure 3-1: Schematic of PMMA micro capillary electrophoresis device: (a) top-down view and (b) cross-sectional view.

A top-down view of the device used in this study is shown in Figure 3-1(a). Microfluidic channels were fabricated by hot embossing patterns into PMMA substrates using photo-lithographically patterned silicon masters similar to the procedures previously published [105]. Briefly, a CO_2 laser-machined PMMA blank was aligned over a silicon master template ensuring that the fluidic access ports coincided with the raised structures on the silicon template at desired locations. The PMMA/silicon template assembly was then placed between two custom-built aluminum blocks with embedded heaters connected to a temperature controller. Subsequently, the assembly was mounted in a hydraulic press (Carver Inc., Wabash, IN) and the temperature was increased to 105 °C. Once the assembly reached the desired temperature, the pressure

was increased to 5.5 MPa. After approximately 30 min, the temperature was reduced to 80 °C before releasing the pressure. The PMMA/silicon template assembly was then removed from the aluminum heaters and allowed to cool to the room temperature. Figure 3-1(b) shows cross-sectional view of microchip used in the study. The imprinted channel was 80 μm deep and 200 μm wide at the bottom surface.

Sealing of the microchannel was accomplished by a thermal lamination process. First, the LDPE/EVA side of the laminating foil was placed over the microchannel side of the PMMA substrate. Then, the PMMA/laminating foil assembly was placed between a sheet of 75 gr/cm² (20 lb; 0.09 mm) paper and a sheet of PC and rolled through a lamination machine (HRL 4200, Think & Tinker Ltd., Palmer Lake, CO) at a temperature of 160 °C, and a velocity of 45.7 cm/min.

3.2.3. Microchannel Surface Modification

Method 1 (■) PMMA ⟶ 40DEA–60DMA

Method 2 (▼) PMMA $\xrightarrow[\text{15 min}]{\text{UV/Ozone}}$ PMMA* ⟶ HPMC

Method 3 (▲) PMMA $\xrightarrow[\text{10 min}]{\text{UV/Ozone}}$ PMMA* ⟶ HPMC

Method 4 (●) PMMA $\xrightarrow{\text{HNO}_3}$ PMMA* $\xrightarrow{\text{HPMC} + \text{H}_3\text{PO}_4}$ PMMA** ⟶ HPMC

Method 5 (♦) PMMA $\xrightarrow[\text{10 min}]{\text{UV/Ozone}}$ PMMA* ⟶ PVA
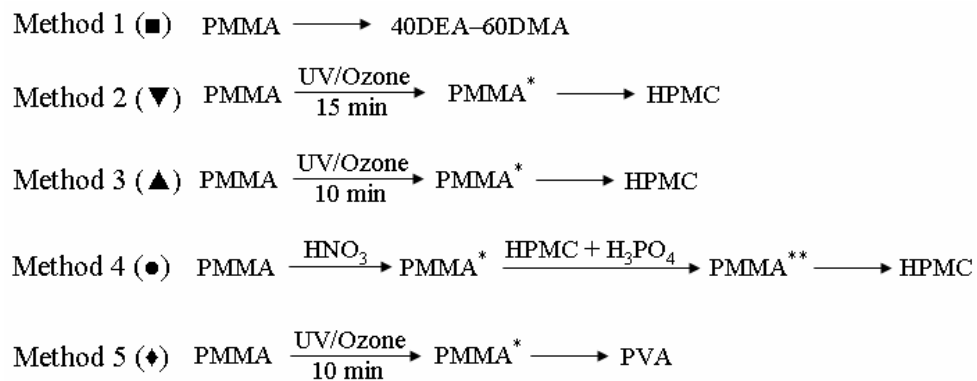
Figure 3-2: Schematic representation of the surface treatments investigated in the PMMA microchannel. Asterisks indicate modified surface.

Figure 3-2 shows various methods investigated in this study for the application of coating polymers to the microchannel surface. Specifically, in Method 1 (■), an aqueous solution of 0.5% w/v 40DEA-60DMA was flushed through a pristine PMMA microchannel. In Method 2 (▼), the PMMA substrate imprinted with the microchannel was exposed to UV irradiation (12 to 20 mW/cm^2; UVCOS Inc., Montgomeryville, PA) for 15 min. Then, an aqueous solution of 0.5% w/v HPMC was flushed through the microchannel. It should be noted that UV irradiation was carried out prior to enclosing the microchannels and that the laminating foil was not treated with UV/ozone. In Method 3 (▲), the PMMA substrate with the microchannel was irradiated with UV light for 10 min followed by flushing with an aqueous solution of 0.5% w/v HPMC. In Method 4 (●), the microchannel was first flushed with a 3 mol L^{-1} aqueous solution of HNO$_3$ and the residence time of HNO$_3$ in the microchannel was merely long enough to aspirate a plug of solution through the entire length of the microchannel. This was followed by rinsing with a 0.5% w/v solution HPMC dissolved in 20mM H$_3$PO$_4$, and finally with an aqueous solution of 0.5% w/v HPMC. It should be noted that the HNO$_3$ treatment was performed in a sealed microchannel. In Method 5 (♦), the PMMA substrate with the microchannel was first irradiated with UV light for 10 min. Then, a 2% w/v aqueous solution of PVA was applied to the microchannel according to the procedures partially adopted from the literature [114, 130]. The microchannel and reservoirs were first filled with PVA solution and incubated at room temperature for 10 min. Then, the reservoirs and channel were emptied by a vacuum pump. Thereafter, the adsorbed PVA coating was dried by heating at 110 °C for 15 min. The above procedure

was repeated for a total of two treatments resulting in a multilayer PVA coating. All of the microchannels were rinsed with deionized water before performing separations.

3.2.4. Contact Angle Measurements

Sessile drop-contact angle measurements utilizing approximately 6 μL drop of deionized water were performed with a contact angle analyzer (First Ten Ångstroms, Portsmouth, VA). Each of the contact angle values shown in this study were determined by averaging the values measured at three randomly chosen points on each sample surface. The samples were sonicated in ethanol for 10 min and dried using a N_2 gun prior to any treatment and the contact angle measurements were performed immediately after sample treatment.

3.2.5. Microchip Electrophoresis

All electrophoretic separations were conducted on the stage of a confocal laser-induced fluorescence microscope (Carl Zeiss MicroImaging, Inc., Thornwood, NY). Briefly, excitation of the fluorescein-labeled ssDNA was achieved by using the 488-nm line of a 30 mW Argon ion laser. The laser beam was focused approximately 4 mm from the end of the separation channel using a 20×, 0.4 NA microscope objective. Fluorescence as a function of time at the end of the channel was monitored through a 505-nm long-pass filter by a photomultiplier tube. A high voltage power supply (HV488, LabSmith, Livermore, CA) was used to provide voltages from 0 V to 1500 V.

A solution consisting of 3% (w/v) 5×Nanogel (a polyacrylamide architecture) [107] dissolved in TTE with 7 mol L^{-1} urea was used as a sieving matrix for the microchannel coated with 40DEA-60DMA. A solution consisting of 2.75% (w/v) 5×Nanogel ($M_w \sim 8.8$ MDa) and 0.25% (w/v) LPA ($M_w \sim 638$ kDa) dissolved in TTE with 7 mol L^{-1} urea was used as a sieving matrix for all other experiments. The sieving matrix buffer solution was pumped into the microchannel from reservoir C (Figure 3-1) using a hydraulic laboratory press with custom built gaskets and jig with an applied pressure differential of 345 kPa. Reservoir B was filled with the sample, and reservoirs A and D were filled with buffer solution prior to analysis. Sample injection was accomplished by applying + 400 V at reservoir D while keeping reservoir B at 0 V for 60 s (reservoirs A and C were left floating during the injection), for an effective electric field strength of 285 V/cm. Sample separation was performed by applying + 1500 V to reservoir C, + 160 V to reservoir B, and + 170 V to reservoir D, while applying 0 V to reservoir A, for an effective electric field strength during separation of 190 V/cm. The "pull-back voltages" applied to prevent extraneous sample leakage from wells B and D into the separation channel were different due to the presence of the injection offset region shown in Fig. 3-1.

Resolution was obtained by fitting Gaussian peaks to raw ssDNA separation data using PeakFit v4.06 (SPSS Inc., Chicago, IL). The separation efficiency, η, (plates m^{-1}) was calculated according to:

$$\eta = \frac{N}{L} = \frac{t^2}{L \cdot (FWHM/2.35)^2} \qquad (3\text{-}1)$$

where N is the number of theoretical plates, L is the migration distance in meters, t is the migration time in seconds, and *FWHM* is the full temporal width of the peak at half maximum. The selectivity, which is defined as the peak spacing in a separation, is a measure of the sieving power of the network and was calculated using $\Delta\mu_{1,2}\big/\overline{\mu}_{1,2}$ with $\Delta\mu_{1,2}$ being the difference in mobility between fragments 1 and 2, and $\overline{\mu}_{1,2}$ being the average value of the mobility of fragments 1 and 2.

3.3. Results and Discussion

Rapid, efficient electrophoretic separations of biomolecules are important for many applications including DNA sequencing, forensic DNA typing, and proteomics. The required electrophoretic separation resolution depends on the application, and as shown in eq (3-1), it is affected by selectivity and peak width. In microfluidic separations, the efficiency is mostly limited by analyte-wall interactions because of small injection plug width of analyte band. These parameters, in general, are governed by the channel geometry, electrophoretic conditions, sieving matrix, and polymeric wall coatings, to name a few. Therefore, peak broadening can often be minimized by a robust and effective wall coating protocol, and careful characterization enables optimization of the coating protocol for high-efficiency separations. Below, we quantitatively measure wall hydrophilicity by performing contact angle measurements for various coating protocols and correlate it to electrophoretic separation efficiency.

3.3.1. Microchannel Surface Oxidation

Oxidation of the PMMA surface creates hydrogen bond donors that aid in the spontaneous formation of polymer coating on the surface of the microchannel. The low pressure mercury vapor lamp used in this study for UV/ozone treatment at room temperature in air generates over 95% of the UV energy at 254 nm and the balance at 185 nm. The presence of these two wavelengths in air causes continuous formation and destruction of ozone resulting in the generation of atomic oxygen [131]. In particular, the radicals react with O_2 molecules as well as with activated species produced by photolysis, resulting in oxidation of the polymer surface [122]. Therefore, UV irradiation of PMMA causes scission of various chemical bonds in polymer chains including C—C, C—H, C==O, and results in the formation of oxygen-containing species such as carboxylate and hydroxylate groups [132]. HNO_3 is also a rapid oxidizer and likely introduces nitrate groups on the surface of the microchannel. In either case, oxidation of the PMMA surfaces provides hydrogen-bond donors for spontaneous adsorption of the wall coating polymers.

3.3.2. Contact Angle Measurements
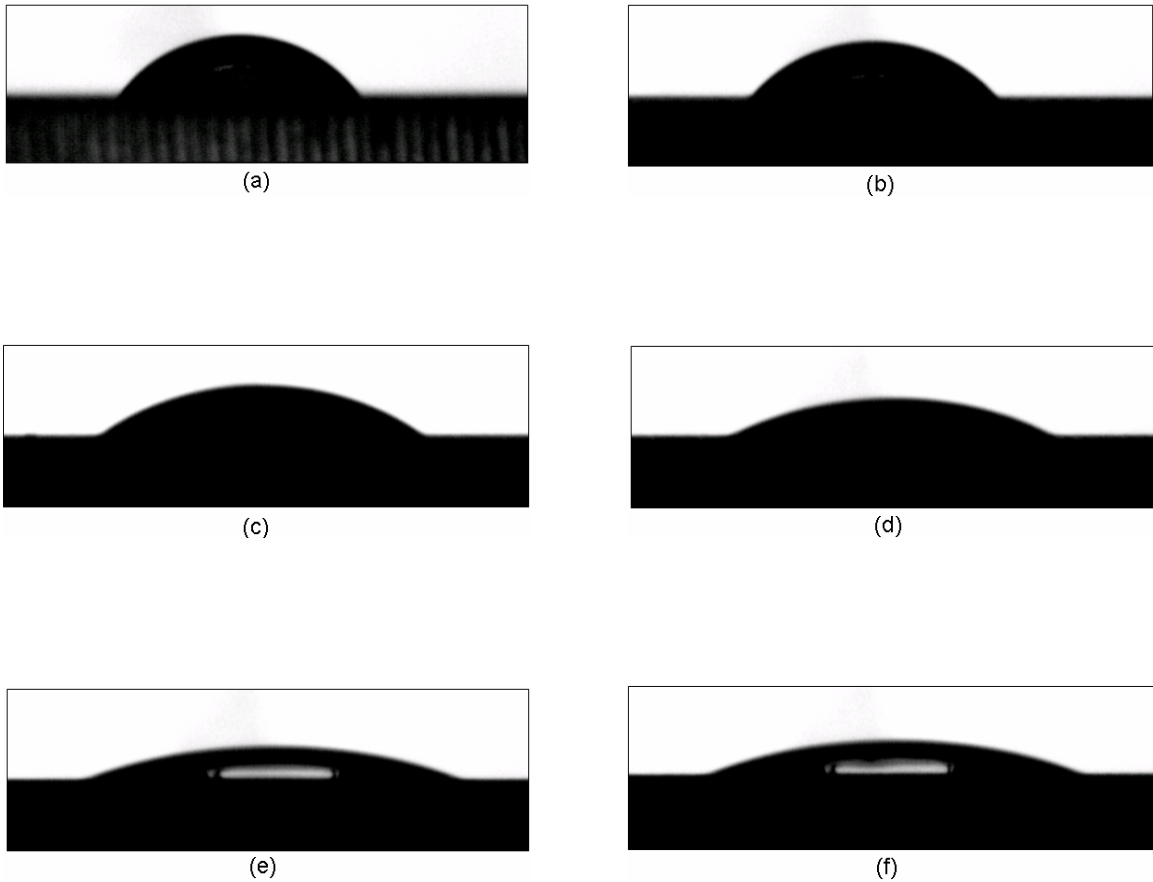
Figure 3-3: Sessile water drop contact angles of (a) pristine PMMA, (b) 4 min UV-irradiated PMMA, (c) 8 min UV-irradiated PMMA, (d) 12 min UV-irradiated PMMA, (e) 16 min UV-irradiated PMMA, and (f) 20 min UV-irradiated PMMA.

During the surface modification steps, sessile drop water contact angle measurements were taken on the PMMA surfaces as a simple measure of the changes induced on the surface as a result of the modification procedure. Figure 3-3 shows photographs of water drops on UV-irradiated PMMA surfaces with duration of UV exposure increasing from (a) to (f). It can be observed that wettability of the PMMA surface increases with increasing UV exposure time. For instance, the same volume of

water drop (6 µL) spreads out more on 20-min UV-irradiated PMMA surface (Figure 3-3(f)) compared to pristine PMMA surface (Figure 3-3(a)).
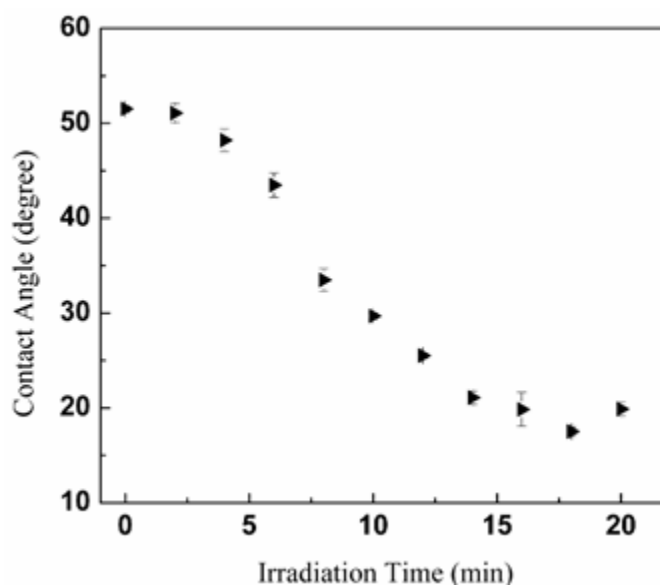
Figure 3-4: Water-contact angle measurements of UV-irradiated PMMA surface as a function of time. Error bars indicate the standard deviation of the contact angle measurement (n = 3).

Table 3-1: Contact angle values of modified PMMA surfaces. (■) PMMA surface coated with an aqueous solution of 0.5% w/v 40DEA-60DMA, (▼) PMMA surface irradiated with UV light for 15 min and coated with an aqueous solution of 0.5% w/v HPMC, (▲) PMMA surface irradiated with UV light for 10 min and coated with an aqueous solution of 0.5% w/v HPMC, (●) PMMA surface rinsed with 3 mol L^{-1} solution of HNO_3 acid and coated with an aqueous solution of 0.5% w/v HPMC, (♦) PMMA surface irradiated with UV light for 10 min and coated with 2% w/v solution of PVA. The standard deviation is calculated for a total of three measurements.

Surface Treatment	Contact Angle (degree)	Std Dev (n = 3)
Method 1 (■)	64.0	3.98
Method 2 (▼)	49.4	0.40
Method 3 (▲)	46.9	1.14
Method 4 (●)	31.6	1.44
Method 5 (♦)	18.9	0.83

Changes in the water contact angles of pristine and UV-irradiated PMMA substrates are plotted in Figure 3-4 and changes in water contact angle values of PMMA substrates treated with polymeric wall coatings are shown in Table 3-1. The surface wettability of the UV-irradiated PMMA substrates varied significantly with the exposure time. The contact angle of the UV-exposed PMMA surface decreased from approximately 52° to 30° upon 10 min exposure and plateaued at approximately 20° after 14 min of exposure to UV light. The slight increase in contact angle at 20 min exposure may indicate overtreatment of the surface [133], and may be caused by a change in surface roughness or to a partial removal of the oxidized region from the PMMA surface

[121]. UV irradiation of PMMA rendered it slightly yellow, especially for extended exposure to UV. However, it did not appear to have any adverse effect on the laser-induced fluorescence detection of ssDNA. The PMMA surface coated with 40DEA-60DMA (■) with a contact angle of 64° exhibited the highest degree of hydrophobicity. On the other hand, the PMMA surface coated with PVA (♦) resulted in a contact angle of 19° and exhibited the highest degree of wettability. Water contact angles of PMMA surfaces exposed to UV irradiation for 10 min or 15 min and subsequently coated with HPMC were found to be 47° (▲) and 49° (▼), respectively. The degree of hydrophilicity for both surfaces was approximately the same, which suggests that the wettability of the final surface depends on the coating polymer and not on further UV irradiation of the PMMA surface. The PMMA surface pretreated with HNO_3 and coated with HPMC (●) resulted in a contact angle of 32°. It is postulated that the H_3PO_4 trapped in HPMC pores is likely a factor contributing to the difference in contact angle from that obtained for the PMMA surfaces exposed to UV and coated with HPMC. The trend in contact angles obtained for polymer coated surfaces was in agreement with theory as it is known that PVA is more hydrophilic than HPMC, which in turn is more hydrophilic than 40DEA-60DMA.

Oxidation, with UV/ozone or HNO_3, of PMMA renders the surface hydrophilic, and yields charged groups at the surface. Although hydrophilic surfaces are less prone to hydrophobic analyte-wall interactions, charged species would engender EOF and cause electrostatic analyte-wall interactions. Therefore, such surfaces are not directly suitable for high performance electrophoretic separation of ssDNA, and necessitates the

application of charge-neutral, hydrolytically stable coating polymers on the microchannel walls [134]. Additionally, it should be noted that the charged groups on the PMMA surface are required for effective hydrogen bridge bonding between the substrate and the coating polymer for enhanced physical adsorption of the coating polymer.

3.3.3. DNA Separation Performance
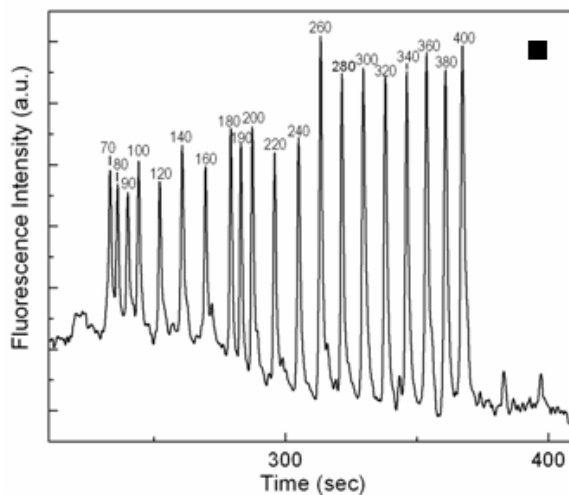
(A)
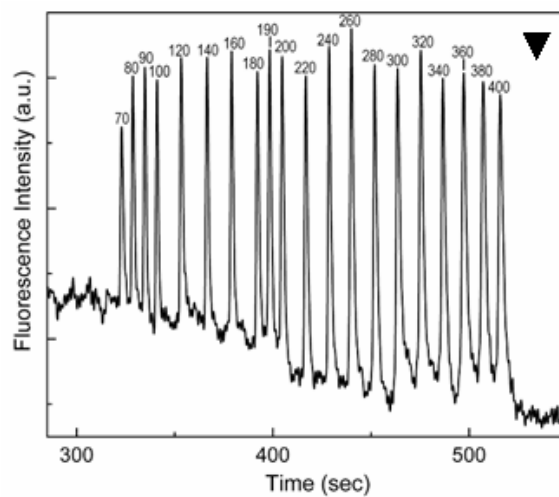
(B)
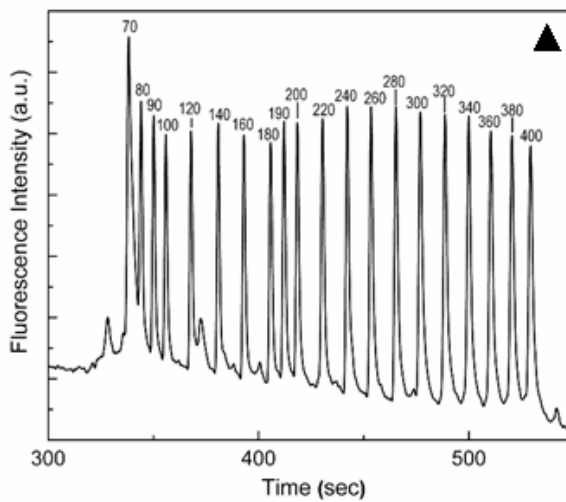
(C)

(This figure is part of Figure 3-5. See following page for caption).
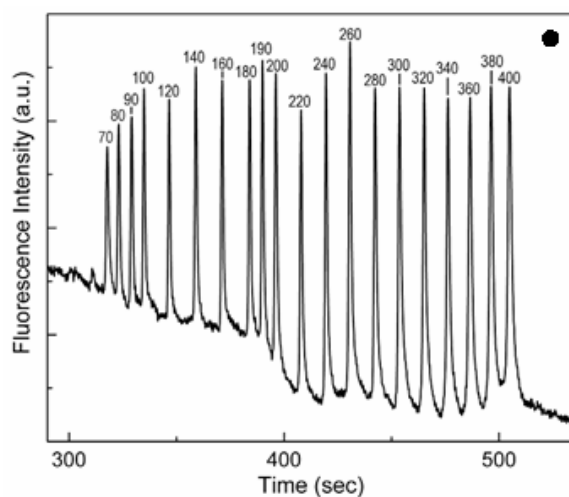
(D)
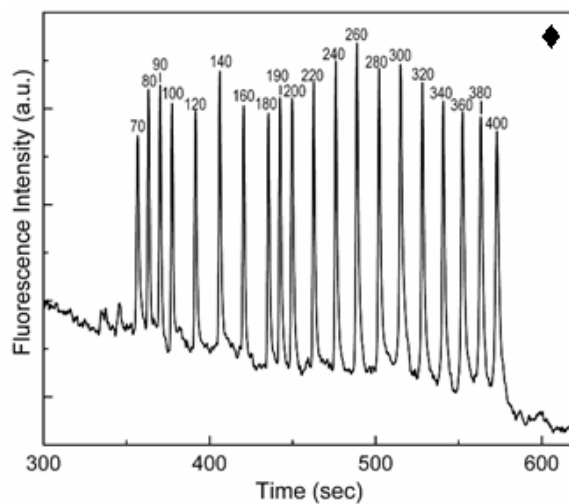
(E)

Figure 3-5: Typical electropherograms showing the separation of a 20-base ssDNA ladder. Electrophoretic conditions: Injection Field = 285 V/cm, Separation Field = 190 V/cm; Separation buffer matrix: (A) 3% w/v 5×Nanogel in a TTE (89mmol L^{-1} Tris, 89 mmol L^{-1} Taps, 2mmol L^{-1} EDTA) + 7 mol L^{-1} urea buffer; (B − E): 2.75% w/v 5×Nanogel + 0.25% LPA (MW ~ 638 kDa) in a TTE + urea buffer. (■) 40DEA-60DMA coating, (▼) 15 min UV irradiation followed by HPMC coating, (▲) 10 min UV irradiation followed by HPMC coating, (●) HNO$_3$ followed by HPMC coating, (♦) 10 min UV irradiation followed by PVA coating.

The effect of wall coating hydrophilicity on DNA separation performance was examined for a 20-base ssDNA ladder. Figure 3-5 shows representative electropherograms illustrating the CE separation for different surface treatments and polymer wall coatings. It should be noted that the coating polymers were not included in the sieving matrix solution and the surface was not recoated or reconditioned between consecutive runs. All the coating polymer protocols investigated in this work resulted in baseline separation of all ssDNA fragments.

It can be seen from Figure 3-5■ that separations in untreated PMMA surfaces coated with 40DEA-60DMA suffered from significant tailing, putatively due to hydrophobic interactions between ssDNA fragments and a relatively hydrophobic 40DEA-60DMA coating. Thus, 40DEA-60DMA was not investigated with oxidized surfaces as it is believed that it adsorbs to the microchannel surface via hydrophobic interactions [135]. The width of the peaks in the microchannel that was exposed to 15 min UV irradiation (Fig. 3-5▼) and coated with HPMC was greater than that in the microchannel exposed to 10 min UV irradiation and coated with HPMC (Fig. 3-5▲). As mentioned earlier (section 3.3.1), it is possible that the surface roughness increases as the UV irradiation time increases, and that the sample interactions with rougher surface tend to widen the peaks (Fig. 3-5▼). In comparison with Figures 3-5▼ and 3-5▲, the PMMA microchannel oxidized with an aqueous solution of HNO_3 and subsequently coated with HPMC (Fig. 3-5●) showed reduced peak tailing. Similarly, the PVA coated PMMA surfaces with prior exposure to UV for 10 min (Fig. 3-5♦) clearly suppressed

analyte adsorption and also resulted in superior separation performance in agreement with the results reported for fused silica capillaries.

3.3.4. Theoretical Plate Count
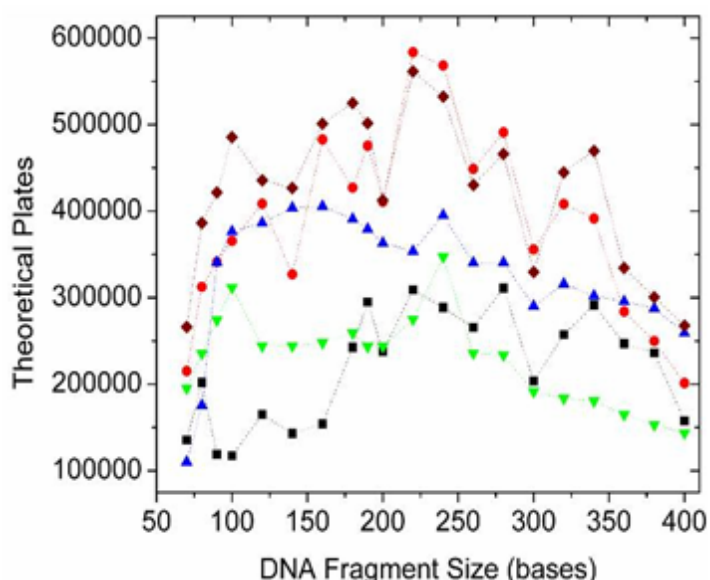
Figure 3-6: Theoretical plate count of ssDNA fragments, obtained for different surface treatment protocols. (■) 40DEA-60DMA coating, (▼) 15 min UV irradiation followed by HPMC coating, (▲) 10 min UV irradiation followed by HPMC coating, (●) HNO₃ followed by HPMC coating, (♦) 10 min UV irradiation followed by PVA coating. The lines are drawn to guide the eye.

Theoretical plates, N, obtained for an average of two runs for various surface treatment protocols are shown in Figure 3-6. The microchannel coated with 40DEA-60DMA (■) resulted in the lowest number of theoretical plates of all surface treatments investigated with N ranging from 117 000 to 311 000. There was a pronounced

difference in the ssDNA separation performance (theoretical plates) between the microchannels coated with 40DEA-60DMA (■) and PVA (♦). The number of theoretical plates for the PVA coated microchannels (♦) varied from 266 000 (3.6×10^6 plates m^{-1}) to 561 000 (7.7×10^6 plates m^{-1}) indicating as much as a twofold increase from that obtained with the application of 40DEA-60DMA coating for most of the fragments analyzed. The number of plates from the microchannels irradiated with UV for 10 min and coated with HPMC (▲) were found to be between 110 000 and 406 000, whereas the number of plates from 15 min UV irradiated and HPMC coated (▼) microchannels ranged from 144 000 to 347 000. Even though the range of values obtained for ▼ fall within the range of values obtained for ▲, careful examination of Figure 3-6 shows that ▲ produced overall greater efficiency. Specifically, the mean of the ratio of ▲ to ▼ for the number of theoretical plates was found to be 1.44 for a standard deviation of 0.33. Significantly diminished N for ▼ may be attributed to increased roughness of the PMMA surface due to longer UV exposure times. The microchannels oxidized with HNO_3 and coated with HPMC (●) resulted in greater N, ranging from 201 000 (2.8×10^6 plates m^{-1}) to 583 000 (8.0×10^6 plates m^{-1}), compared to those treated with UV/ozone and coated with HPMC. These results are consistent with the decreasing contact angle measurements.

Although the difference in contact angle between ● and ♦ is significant, it is interesting to note that N is comparable for both cases. This is in agreement with the previously stated speculation that the HNO_3 treatment resulted in all four of the channel walls being oxidized and coated rather than just the three PMMA walls as is the case for UV/ozone treatment of the microchannels. UV irradiation of the microchannel cover

plate was not performed because contact angle measurements of the UV exposed LDPE/EVA surfaces for varying UV exposure times did not produce significant change in hydrophilicity (data not shown). More importantly, UV exposure of the LDPE/EVA surface significantly reduced bond integrity, which precluded longer exposure times. Even though the interactions of the various coating polymers with the LDPE/EVA surface may contribute to improving the separation performance, they are not believed to dominate the improvement in separation performance as the LDPE/EVA surface only amounts to approximately 40% of the total surface area of the microchannel.

3.3.5. Selectivity
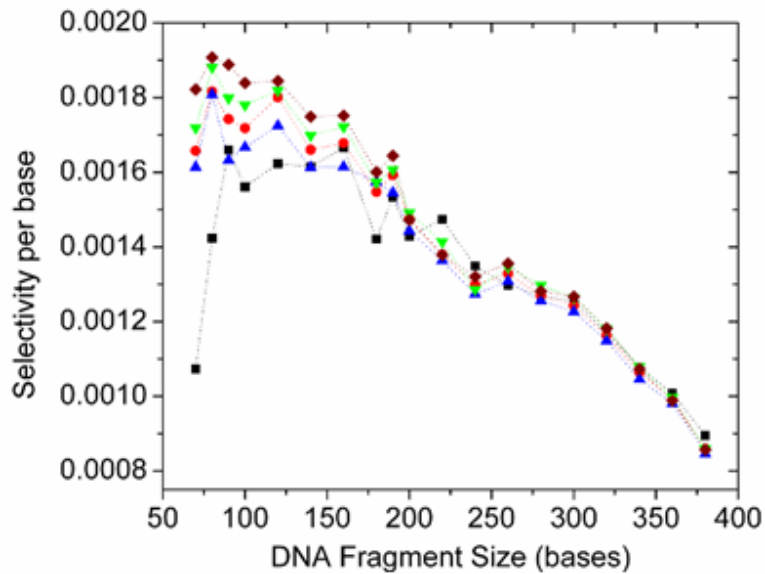
Figure 3-7: Selectivity of ssDNA fragments as a function of DNA fragment size, obtained for different surface treatment protocols. (■) 40DEA-60DMA coating, (▼) 15 min UV irradiation followed by HPMC coating, (▲) 10 min UV irradiation followed by HPMC coating, (●) HNO$_3$ followed by HPMC coating, (♦) 10 min UV irradiation followed by PVA coating. The lines are drawn to guide the eye.

The average selectivity for various surface treatments for two observations is plotted in Figure 3-7. The selectivity was found to vary from 0.001 to 0.002 for all of the wall coating protocols investigated in this study. Hence, it can be inferred that the selectivity is largely independent of the microchannel coating protocol, and that there is no incompatibility between any of the wall coatings and the sieving matrix solution.

3.3.6. Resolution
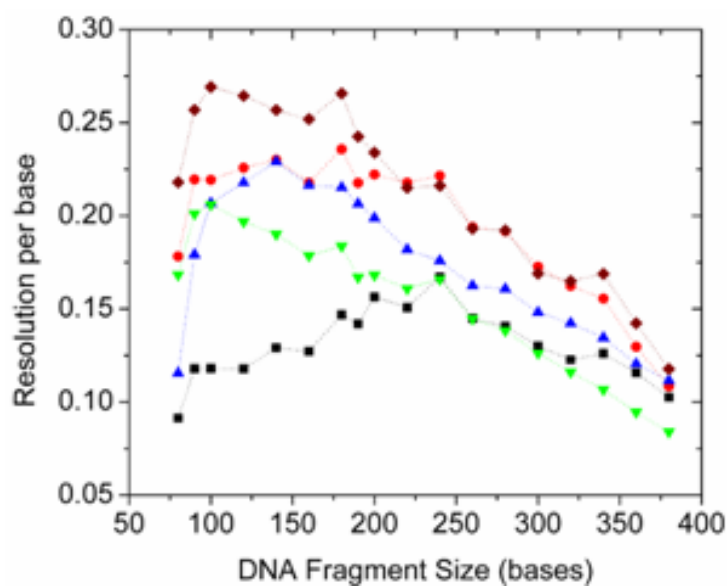
Figure 3-8: Resolution of ssDNA fragments as a function of DNA fragment size, obtained for different surface treatments and polymer coatings. (■) 40DEA-60DMA coating, (▼) 15 min UV irradiation followed by HPMC coating, (▲) 10 min UV irradiation followed by HPMC coating, (●)HNO_3 followed by HPMC coating, (♦) 10 min UV irradiation followed by PVA coating. The lines are drawn to guide the eye.

Figure 3-8 shows the average resolution, $\Re$, for two observations normalized to the difference in fragment size for all surface treatments investigated in this study. The average resolution obtained for the 40DEA-60DMA coated microchips varied from 0.08 base^{-1} to 0.17 base^{-1}. As seen from Figure 3-8, electrophoretic separation of ssDNA in the microchannel irradiated with UV for 15 min and coated with HPMC yielded $\Re$ from 0.08 base^{-1} to 0.21 base^{-1}. In contrast to 15 min UV/ozone treatment, 10 min UV/ozone treatment using the same coating resulted in a higher $\Re$, 0.11 base^{-1} to 0.23 base^{-1}. These results are qualitatively consistent with those obtained for η. The resolution obtained using the microchannels treated with HNO_3 as an oxidizing agent and coated with HPMC resulted in $\Re$ from 0.11 base^{-1} to 0.24 base^{-1}. Finally, 10 min UV treatment along with PVA coating yielded the highest resolution of all treatments studied with $\Re$ ranging from 0.12 base^{-1} to 0.27 base^{-1}. The increase in resolution from the 40DEA-60DMA coating to the PVA coating was due to a reduction in peak width and not peak spacing indicating that the reduction in analyte-wall interactions due to a more hydrophilic wall coatings is likely the reason for improved resolution.

In summary, it is shown that the efficiency of ssDNA fragments and hence the resolution increases as the coating polymer hydrophilicity increases. HNO_3 treatment of the interior of a channel appears to activate significantly more channel surface area and does not require specialized laboratory equipment. On the other hand, UV/ozone treatment of PMMA substrates produces a significantly more hydrophilic surface than UV/ozone treatment of LDPE/EVA surfaces. Hence, the microchannels which are entirely composed of PMMA such as those fabricated with thermal bonding or solvent

80

bonding method would be expected to produce a superior separation performance [136]. The UV/ozone treatment is also simple to implement and could be easily localized to specific areas of integrated microchips with complex architecture by using photo masks allowing for spatial patterning of different surface chemistries.

3.4.   Conclusions

Several methods for the chemical modification of PMMA surfaces for the application of wall coating polymers to suppress EOF and to reduce analyte-wall interactions are presented in this study. The hydrophilicity of the PMMA surface was altered by UV irradiation and HNO_3 treatment in air at atmospheric pressure and at room temperature. Contact angle measurements were conducted to determine the change in wettability of the surface. Electrophoretic separations of ssDNA were successfully performed in microchips prepared using these methods. It was empirically observed that the 10 min UV irradiated surfaces coated with HPMC yielded better separation performance than the surfaces irradiated with UV for 15 min and coated with HPMC. Further, the UV/ozone treated surfaces coated with PVA and the HNO_3 treated surfaces coated with HPMC resulted in the highest separation performance with plate efficiency regularly exceeding 413 000 plates. Subsequently, the two coating protocols have been successfully used for ssDNA separations in longer channels (data not shown) to further improve resolution. It has been shown that the hydrophilicity of the wall coating polymer can increase the separation efficiency and resolution.

This approach to wall coating should be versatile and transferable to other polymeric substrates as well. Additionally, the methods presented in this study are less time-

consuming and less laborious than those published previously and are conducive to automation for mass production of disposable microfluidic devices.

4. Microwave Dielectric Heating of Microfluidic Devices

4.1. Introduction

Rapid, selective, and uniform heating of fluid volumes ranging from a few microliters to as low as a few nanoliters is vital for a wide range of microfluidic applications. As mentioned in Chapter 1, DNA amplification by polymerase chain reaction (PCR) is critically dependent on rapid and precise thermocycling of reagents at three different temperatures between 50 °C and 95 °C [137]. Another important and related application, temperature induced cell lysis, necessitates fluid temperature in the vicinity of 94 °C [138]. Other potential applications of heating in a microchip format include organic/inorganic chemical synthesis, the investigation of reaction kinetics, and biological studies, to name a few.

A number of conduction-based heating approaches have been reported for microfluidic systems that include embedded resistive heaters, peltier elements, or joule heating under electroosmotic flow conditions [19, 139-141]. Generally speaking, these methods require physical contact between a fluid and a heated surface to transfer heat from that surface to the fluid. In microfluidic devices, when the fluid volumes approach nanoliters, heating rates will be potentially limited by the added thermal mass of the substrates used for heat transfer, and not by the fluid volume. The transfer of heat in such manner can also result in heating of large, undesired substrate areas creating spatial limitations for integration of multiple analysis functions on a single substrate.

Additionally, the implementation of these heating methods will be limited to high thermal diffusivity substrates, such as silicon and glass, to maximize heat transfer rates. However, such substrates due to their high cost and complexity of the fabrication process are unsuitable for use in disposable devices.

Due to a number of inherent problems associated with contact-mediated temperature cycling, a number of research groups have focused on the development of non-contact heating approaches. These non-contact heating approaches include heating based on hot air cycling [142, 143], heating based on IR light [28], laser-mediated heating [144], halogen lamp-based heating [145], induction heating [146], and heating based on microwave irradiation. Hot air based heating method utilizes rapidly switching air streams of the desired temperature and transfer of air onto either polypropylene tubes or glass capillaries. However, the control and application of hot air streams on microfabricated integrated systems may not be easily accomplished without an impact on other structures or reactions to be executed on the chip [28]. Oda *et. al.* [28] have demonstrated the use of an inexpensive tungsten lamp as an IR source for rapidly heating small volumes of solution in a microchip format. Although fast cycling times have been attained, the task of achieving high throughput with this approach still remains a challenge. Moreover, the tungsten lamp is a non-coherent and non-focused light source leading to a relatively large focus projection, which can potentially limit the heating efficiency when applied to microchips with smaller cross-section [137]. Other light based heating methods have been demonstrated for microfluidic heating, but such systems, generally speaking, require lenses and filters to eliminate wavelengths that could

interfere with the reaction, and accurate positioning of the reaction mixture at the appropriate focal distance from the lamp, which further complicates their implementation.

Microwave dielectric heating is a candidate to address these issues because of its preferential heating capability and non-contact delivery of energy. It is based on direct volumetric delivery of heat, *i.e.* microwave energy can be delivered to the sample with no interference from the substrate material [147]. Enhanced thermocycling rates and reduced reaction times compared to conventional techniques can be achieved because of the inertialess nature of microwave heating [148]. Heating can also be made spatially selective by confining the electromagnetic fields to specific regions in the microfluidic network. Further, the dielectric properties of the fluid can also be exploited to deliver heat using signal frequency as a control parameter in addition to the power. The microwave power absorbed per unit volume in a dielectric material is given by:

$$P_v = \sigma E^2 \qquad\qquad (4\text{-}1)$$

where $\sigma = 2\pi f \varepsilon_o \varepsilon''$ is the dielectric conductivity of the material, f is the frequency in hertz, ε_o is a constant called the permittivity of free space, ε'' is the imaginary part of the complex permittivity of the material that depends on the frequency and temperature, and E is the electric field strength in volts per meter within the material [147]. Interestingly, the conductivity of some electrolytes is relatively independent of ion concentration over a small region of microwave frequencies [149]. Therefore, such solutions can be heated with microwaves independently of their ionic strength. This characteristic of microwave

dielectric heating is particularly advantageous when the salt concentration of the solution is not known *a priori* as would be a common case.

The use of microwave heating has been demonstrated for a variety of applications including drug discovery [150], PCR [151, 152], isolation of DNA [153], and heating of biological cells [154]. Macroscale microwave applicators were commonly utilized for the delivery of microwave power to sample contained in the plastic reaction tubes. However, recent interests lie in integrating miniaturized microwave heating elements, in the form of transmission lines, with microfluidic channels for on-chip heating applications [155, 156]. The reported results provide strong foundation for further development of this technology, but much work is required to make this technology commercially-viable.

The work in this study investigates the possibility of utilizing both (macroscale and microscale) types of microwave applicators for microfluidic heating applications. In the first case, a rectangular waveguide with a slot drilled in for the introduction of a microfluidic device is used as a macroscale microwave applicator to deliver microwave power. Thermocycling of deionized water is demonstrated between room temperature and 95 ˚C. Heating rate and cooling rate obtained using this system are compared to those obtained with commercial heating block-based thermocycler.

In the latter case, microwave power is delivered to an elastomeric microchannel via an integrated thin film microwave transmission line. A coplanar waveguide (CPW) has been previously integrated with a fluidic microchannel for on-chip dielectric permittivity and spectroscopy measurements [157, 158]. In this study, the use of CPW

for on-chip microwave heating of fluids in the microchannel is investigated over a wide range of frequencies. The types of fluids used include deionized water as well as buffer solutions with differing salt concentrations. Two-port scattering (S)-parameter measurements of the device when the microchannel is empty and filled with various fluids are performed. The results are subsequently used to characterize the absorption of the microwave power by the device as a function of frequency. The S-parameter data is also used to develop first-order analytic model of the microwave power absorption in low reflectance, lossy transmission lines such as the one utilized in this work. Several parameters such as the microwave power absorbed by the fluid and by the CPW conductors are extracted from the analytic model and used to evaluate the efficiency of this heating method for microfluidic applications. Finally, the fluid temperature at various microwave frequencies is measured using the fluorescence detection technique, and a fit of the predicted temperature obtained using the model developed in this work to the measured temperature is performed.

4.2. Preliminary Work towards Microwave Heating using a Macroscale Rectangular Waveguide

4.2.1. Experimental Details
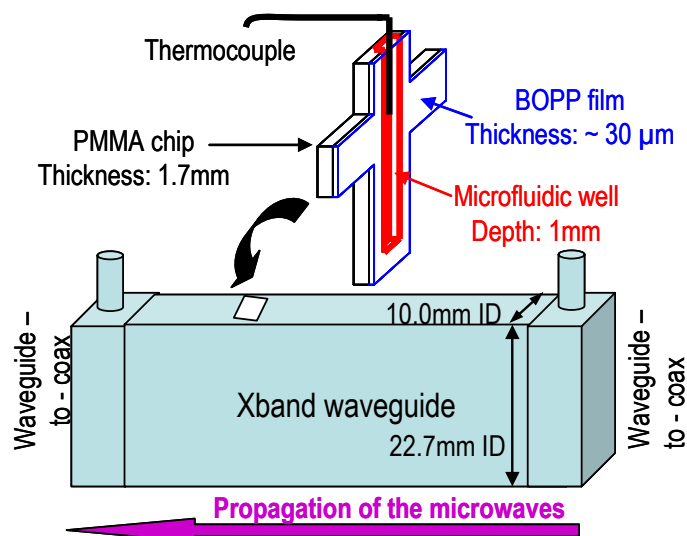
Figure 4-1: A schematic of an x-band rectangular waveguide heating system. A slot was machined into one of the walls of the waveguide to allow the introduction of a microchip. An amplifier coupled to a microwave signal generator was used to provide the desired microwave power and a thermocouple inserted into the microchip was used to measure the fluid temperature.
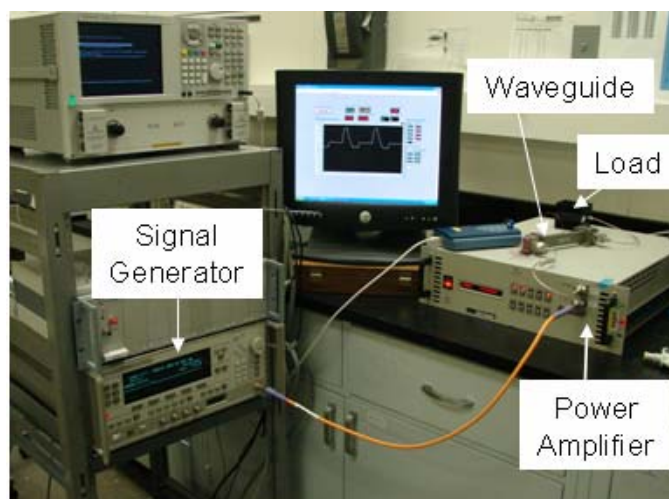
Figure 4-2: Experimental setup for rectangular waveguide based microfluidic heating system. A microwave signal generator was connected to a traveling wave tube amplifier (TWT) to enable the delivery of up to 25W of power over the 8-12 GHZ bandwidth of the x-band rectangular waveguide. A 25W load was attached to the waveguide to terminate microwave power and to ensure unidirectional microwave propagation.

A schematic of an x-band rectangular waveguide used in this study to deliver microwave power is shown in Figure 4-1. A slot was machined into one of the walls of the waveguide to allow the introduction of a microchip. The position of the slot was chosen such that the microchip was placed perpendicular to the direction of the field propagation to maximize coupling of microwave power to fluid. The fluidic channel was micromachined into PMMA substrate of 1.7 mm thickness using a milling machine. The microchannel was 1 mm deep, 2 mm wide and 2 cm long. The channel enclosure was accomplished via thermal lamination technique with PP film according to the procedure specified in Chapter 3. Temperature was monitored using a type-T thermocouple inserted into the microchip. Experiments were performed to verify that the effects from microwave interaction with the thermocouple were minimal (data not included) [152]. The photograph of experimental setup used in this study is shown in Figure 4-2. A HP 83650B signal generator was used to source the microwave power. The signal generator was connected to a traveling wave tube (TWT) amplifier capable of amplifying the input power up to 50W over the 8 GHz to 18 GHz frequency range. The transmitted power out of the waveguide was terminated into 25W load. Microwave adapters, type N to waveguide, were used to convert from the coaxial geometry of the test set to the rectangular geometry of the waveguide.

4.2.2. Results and Discussion
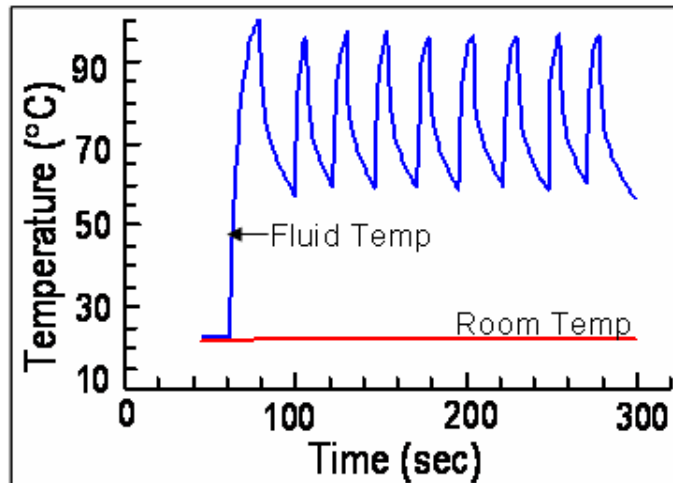
Figure 4-3: On-chip thermocycling of de-ionized water obtained using rectangular waveguide heating system. The fluid volume was approximately 68 μL with applied microwave power of 20W. The average heating rate for this system was 5.96 °C/s and the cooling rate was 2.23 °C/s.
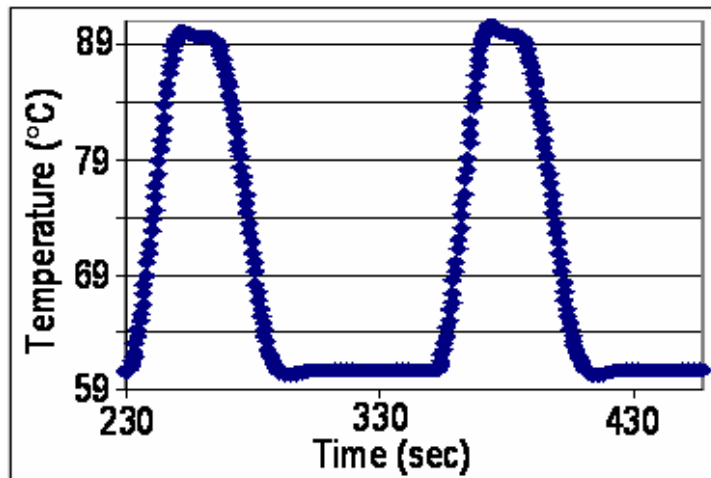
Figure 4-4: Thermocycling of de-ionized water using macroscale conventional thermocycler. The PCR tubes were used to hold 25 μL of fluid. The average heating rate for this system was 1.69 °C/s and the cooling rate was 1.36 °C/s.

Figure 4-3 shows thermocycling of de-ionized water between 60 ˚C and 95 ˚C. As mentioned earlier, DNA amplification by PCR relies on temperature cycling of the reaction mixture through three different temperatures between 50 ˚C and 95 ˚C. Hence, the temperatures for thermocycling in this study were chosen to depict those required for the PCR amplification. The applied microwave power was constant at 20W and it was turned on and off manually. The average heating rate for this system was calculated to be approximately 6 ˚C/s and the cooling rate was found to be 2.2 ˚C/s for a fluid volume of 68 μL. Figure 4-4 shows thermocycling of de-ionized water using conventional metal block-based thermocycler. The sample was held in 25 μL plastic PCR tube, and the heating rate for this system was found to be 1.7 ˚C/s and the cooling rate was calculated to be 1.4 ˚C/s. The data confirms that microwave heating is a viable alternative for on-chip microfluidic systems, and that it can be used to obtain superior thermocycling rates compared to those obtained with conventional macroscale thermocyclers. This preliminary data also provides solid foundation for the development of miniaturized microwave heating elements and to improve the efficiency of this heating method.

4.3. Miniaturized System for Microwave Heating of Fluids

4.3.1. Experimental Details

4.3.1.1. Materials

Silicon wafers were obtained from Nova Electronic Materials, Ltd. (Carrollton, TX). PDMS (Sylgard 184) and Pyrex® 7740 borosilicate glass wafers were obtained

from Dow Corning (Midland, MI). PDMS was mixed and cured according to the manufacturer's specifications. Glass wafers were used as substrate for fabrication of microwave transmission line and PDMS was used as a substrate for fabrication of microfluidic channel. Rhodamine B (laser grade) was purchased from Acros Organics USA (Morris Plains, NJ) and was used for temperature measurements.

4.3.1.2. Device Fabrication

Note: The device fabrication and data collection in this study were carried out by Siddarth Sundaresan of George Mason University.
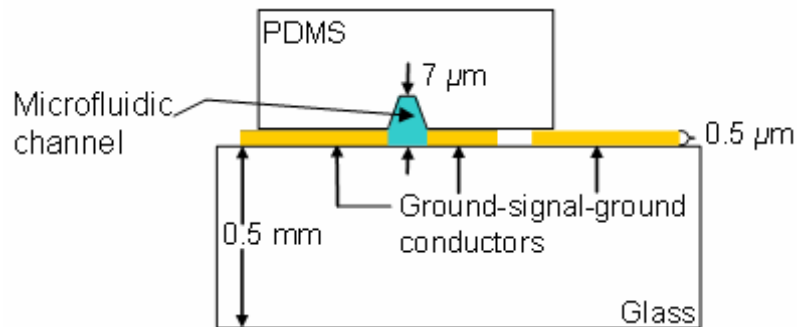
Figure 4-5: Schematic of a cross-section of a coplanar waveguide (CPW) transmission line integrated with a poly(dimethylsiloxane) (PDMS) microchannel for microwave dielectric heating of fluids. The CPW conductors are 1.5 cm long; the single conductor is 140 μm wide and it is separated by a 25 μm gap on either side from 300 μm wide ground conductors. The microchannel consists of a trapezoidal cross section defined by a silicon template and it is 7 μm deep, 25 μm wide at the bottom, and 3.62 mm long.

A schematic of a cross-sectional view of the device fabricated in this study is shown in Figure 4-5. It consisted of a CPW integrated with an elastomeric microfluidic channel. The CPW comprised of a 140 μm wide signal conductor separated by a 25 μm gap on either side from 300 μm wide ground conductors. The CPW conductors, 1.5 cm long, were formed by thermally evaporating Cr/Au (10 nm/500 nm) on a 0.5 mm thick glass wafer and using a standard lift-off metallization process. The microchannel was patterned into poly(dimethylsiloxane) (PDMS) by soft lithography [159]. It consisted of a trapezoidal cross section defined by a silicon template and was 7 μm deep, 25 μm wide at the bottom, and 3.62 mm long. The microchannel was attached by contact adhesion on top of the CPW and approximately centered along the length of the CPW conductors. The microchannel was carefully aligned in the lateral direction over the CPW such that its bottom surface coincided with the separation between the signal conductor and one of the ground conductors (the region of high electric field strength).

4.3.2. Device Characterization

Two types of measurements were taken to characterize the device: scattering (S) parameter and temperature. Precision air coplanar probes obtained from Cascade Microtech, Inc. (Moorestown, NJ) were used to convert from the coaxial geometry of the test set to the coplanar geometry used for the CPW transmission line. S-parameters relate the forward and reflected traveling waves in a transmission medium and can be used to understand the power flow as a function of frequency. In this study, S-parameters are used in conjunction with the conservation of energy to model absorption of microwave

93

power and to predict the fluid temperature based on the absorbed power. The predicted temperature was then fitted to the measured temperature to determine heating efficiency.

4.3.2.1. S-parameter Measurements

S-parameters, the transmission and reflection coefficients, of the device (Figure 4-5) were obtained using a HP 8510C vector network analyzer connected to a HP 8517B S-parameter test set. A HP 83650B signal generator was used to source the microwave continuous wave (CW) signal. The measurements were calibrated using commonly used thru-reflect-line (TRL) calibration utilized for on-wafer characterization of CPW based devices [160]. The experiments in this work were performed with deionized (DI) H_2O and with fluids of two different salt concentrations: 0.9% NaCl solution and 3.5% NaCl solution.

4.3.2.2. Temperature Measurements

The fluid temperature was obtained by measuring the temperature dependent fluorescence intensity of a dilute fluorophore added to the fluid and comparing it to the calibrated fluorescence intensity at a known temperature according to the procedures previously published [161]. Specifically, an aqueous solution of 0.2 mmol/L Rhodamine B prepared in a 19 mmol/L carbonate buffer was used for making temperature measurements. The chemical properties of Rhodamine B have been studied extensively [162, 163], and its temperature-sensitivity has been utilized in a variety of applications [164, 165]. Fluorescence imaging of the Rhodamine B solution in this work was

performed using an inverted laser-induced fluorescence microscope equipped with a long working distance 20× objective, a mercury arc lamp, an appropriate filter set (excitation, 500-550 nm; emission, > 565 nm), and a video camera. All temperature measurements were conducted on the stage of a microscope. A constant microwave power was applied at the input port of the CPW using a signal generator. Microwave power was terminated by connecting a HP 8485B power sensor at the output port of the CPW device while a HP 437B power meter connected to the power sensor was used to measure microwave power. The fluorescence intensity was calibrated using the following technique. A thin-film resistor (8 nm Cr/260 nm Au) of an equivalent footprint (25 microns wide and 3.6 mm long) as the microfluidic channel was patterned on a glass substrate using photolithographic techniques. The microfluidic channel was then aligned on the top of the resistor and filled with an aqueous solution of Rhodamine B dye. The resistor was then heated using a DC power source (Keithley 2001) while the fluorescence intensity of the dye and the resistance of the resistor were recorded. The temperature coefficient of resistance, which had been determined empirically, was used to determine temperature-intensity relationship.

4.3.3. Results and Discussion

Two experiments were performed to evaluate the performance of the CPW devices for heating in the microchannel environment: the first characterizes the frequency response of the device, which is also used to obtain absorption ratios of the devices with empty and fluid-filled microchannels, and the second measures fluid temperature at

various microwave frequencies. The results obtained from the first experiment are used to derive a power absorption model to find the distribution of the incident microwave power in different absorbing structures of the device.

4.3.3.1. S-parameter measurements
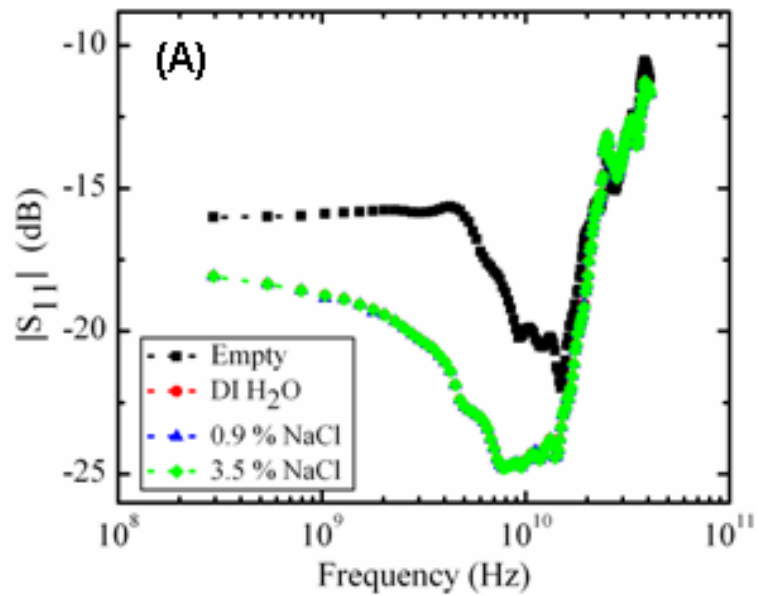
(Please see next page for figure caption.)
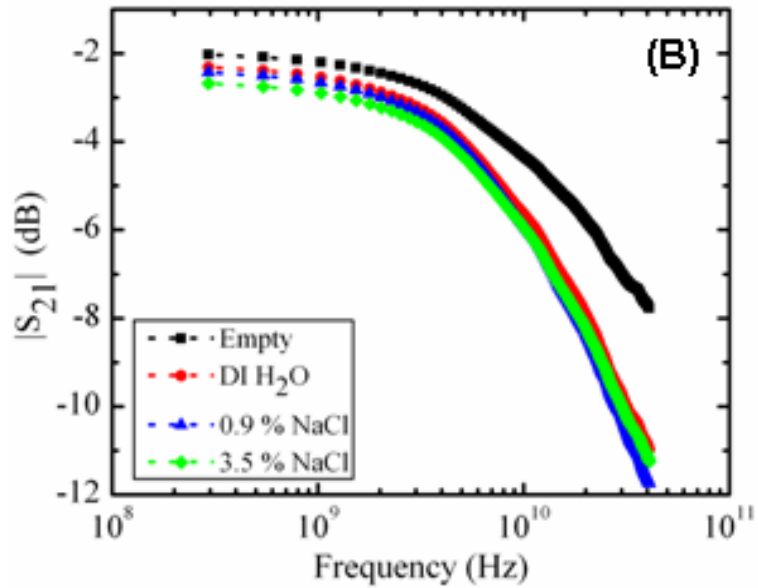
Figure 4-6: (A) Measured reflection coefficients ($|S_{11}|$) of the device. (B) Measured transmission coefficients ($|S_{21}|$) of the device. (■) Empty microchannel, (•) microchannel filled with deionized H_2O, (▲) microchannel filled with 0.9% NaCl, (♦) microchannel filled with 3.5% NaCl.

The amplitude of the reflection coefficients (S_{11}) and transmission coefficients (S_{21}) from 0.3 GHz to 40 GHz for the device with an empty channel as well as for the fluid-filled channels are shown in Figures 4-6(a) and 4-6(b), respectively. In comparison with the empty channel device, S_{11} is reduced for the device with fluid-filled channel and it approaches that of an empty channel for frequencies above 10.5 GHz. The decrease in S_{11} of the fluid-filled devices below 10.5 GHz which indicate good impedance matching conditions are apparently fortuitous. S_{11} is also found to be almost independent of the ionic concentration of the fluid. The localized peak and trough features observed in S_{11} are likely interference effects due to reflections at the probe-CPW interfaces and the

97

CPW/air-CPW/fluid interfaces [158]. S_{21}, as seen from Figure 4-6(b), decreases with increasing frequency for the devices with both the empty and fluid-filled channels. It is believed that the apparent low transmission coefficient of the empty-channel device is likely due to the smaller than optimum thickness of the CPW conductors (0.5 μm). The difference in S_{21} between the empty and fluid-filled channels becomes more pronounced at higher frequencies (> 5 GHz). S_{21} of the fluid-filled devices is smaller compared to the empty-channel device due to the additional attenuation caused by the absorption of the microwave energy in the water.
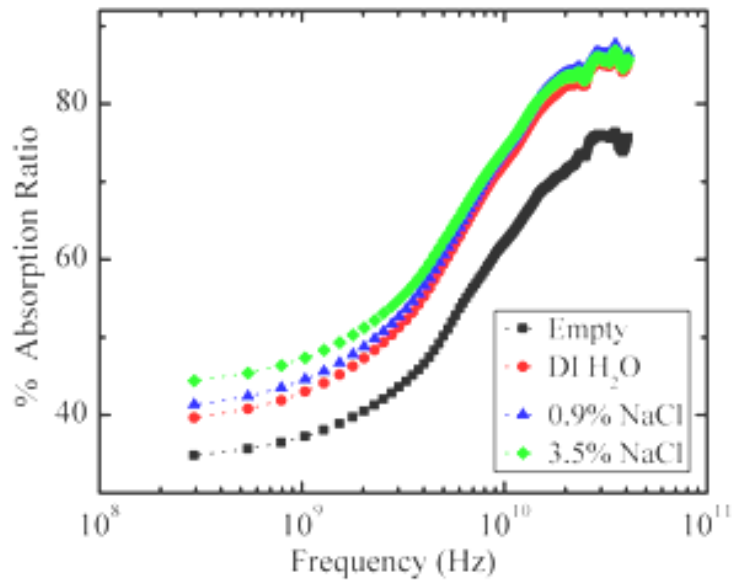
Figure 4-7: The percent absorption ratios (the fraction of the incident microwave power absorbed by the device) as a function of frequency. The absorption ratio, *A*, was calculated from the measured transmission and reflection coefficients using $A = 1 - R - T$. (■) Empty microchannel, (●) microchannel filled with deionized H_2O, (▲) microchannel filled with 0.9% NaCl, (♦) microchannel filled with 3.5% NaCl.

Figure 4-7 shows percent absorption ratios (the fraction of the incident power absorbed by the device) as a function of frequency for the devices with empty and fluid-filled microchannels. The absorption ratio, A, is calculated from the S-parameter data shown in Figure 4-6 and using the following equation:

$$A = 1 - R - T \qquad (4\text{-}2)$$

where R (the reflection coefficient) $= |S_{11}|$, T (the transmission coefficient) $= |S_{21}|$, and S_{ij} $(dB) = 10log_{10}|S_{ij}|$. It should be noted that the absorption ratio is dependent on the position of the microchannel over the length of the waveguide. In other words, S_{21} would not equal to S_{12} and the device would function as a non-reciprocal two-port network unless the microchannel is precisely centered over the length of the waveguide.

The absorption ratio obtained for the device with empty channel (■) is due to ohmic dissipation in the thin-film CPW, which can be modeled by an attenuation constant, α_{cpw}, which corresponds to 2.86 dB/cm at 10 GHz. The attenuation constant of PDMS is assumed to be negligible because of the relatively low values of loss tangent (the ability of a material to convert stored electrical energy into heat) at microwave frequencies [166]. An increase in A observed with increasing frequency for the empty channel device (■) is expected from the dependence of skin depth on frequency. The absorption ratio for the fluid filled devices (●, ▲, and ♦) is greater for all frequencies measured in comparison with the empty channel device (■), due to microwave absorption in water and also ionic absorption in the ionic solutions. The data also exhibit a dependence of A on ionic concentration at lower frequencies as would be expected due to ionic conductivity, while the data at higher frequencies show that A is approximately

independent of ionic concentration as would be expected due to dielectric conductivity. This trend is in agreement with theory [149].

4.3.3.2. Power Absorption Model

It seems from Figure 4-7 that the simplest approximation to the fraction of the incident microwave power absorbed in the fluid is the difference between the power absorbed by the full-channel and empty-channel devices (for the case of water-filled device, $A_{H_2O} - A_{empty}$ in Figure 4-7). However, various microwave power absorption models described in [167] and included in Appendix II show that this simple approximation greatly underestimates the actual fraction absorbed in the fluid.
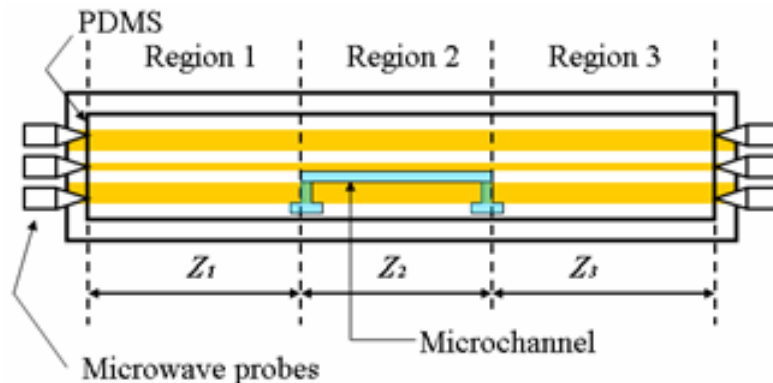
Figure 4-8: Top view of a CPW integrated with an elastomeric microchannel consisting of three regions, center region with the microchannel and the two end regions without the microchannel.

In this work, a simple model is chosen, alpha absorption model, to extract the fraction of the incident power absorbed in the fluid. This model is also used to differentiate microwave heating of the fluid from conductive heating due to ohmic heating of the CPW conductors. As shown in figure 4-8, the model is constructed by assuming that the PDMS completely covers the CPW and by partitioning the CPW into three regions: a center region that interacts with the fluid in the microchannel and two ends that have no microchannel over them. The lengths of each of the three regions are defined by the center region, z_2, 0.36 cm long and two end regions, z_1 and z_3, 0.57 cm long. The reflectance at the interface between the regions is assumed to be negligible, and the transmission coefficient, T, is modeled as follows:

$$T = (1-R) \times e^{-2\alpha_{cpw} z_1} \times e^{-2\alpha_{cpw} z_2} \times e^{-2\alpha_w z_2} \times e^{-2\alpha_{cpw} z_3} \qquad (4\text{-}3)$$

The derivation of this equation is based on exponential attenuation of microwave power in the direction of propagation where the rate of decay with distance is described by the attenuation constant, α. Because of the presence of water in the center region, it should be noted that the attenuation due to water, α_w, is added to the attenuation due to CPW, α_{cpw}. Equation (4-3) is then used to derive α_{cpw} and α_w as follows. First, α_{cpw} is derived for the empty channel device by setting α_w equal to zero into eq. (4-3) and substituting the measured values of T and R for the empty channel device. Next, this value of α_{cpw} is substituted into eq. (4-3) along with the measured values of T_f and R_f, which are T and R for the water filled device. The resulting equation is solved for α_w,

which is found to be 3.68 dB/cm at 10 GHz. The absorption ratio for the central region of the water filled channel, A_2, is calculated as

$$A_2 = (1 - R_f) \times (e^{-2\alpha_{cpw} z_1}) \times (1 - e^{-2(\alpha_{cpw} + \alpha_w) z_2}) \qquad (4\text{-}4)$$

Finally, the absorption ratios of the water, A_w, and CPW conductors, A_{m2}, in the center region are calculated by eq. (4-5) and eq. (4-6), respectively.

$$A_w = \left[\frac{\alpha_w}{\alpha_{cpw} + \alpha_w} \right] A_2 \qquad (4\text{-}5)$$

$$A_{m2} = A_2 - A_w \qquad (4\text{-}6)$$
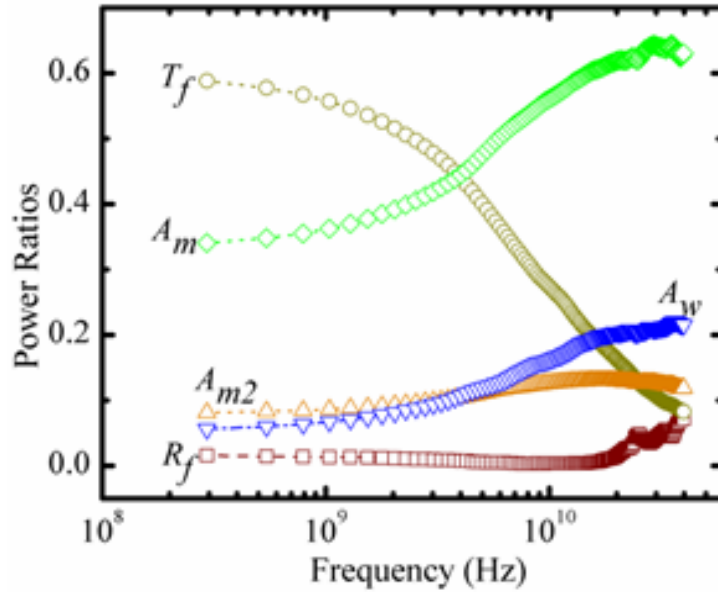
Figure 4-9: The distribution of the incident microwave power in different absorbing structures of deionized H_2O filled device as obtained from the alpha absorption model. T_f, R_f are the transmission and reflection coefficients of the water-filled device, respectively; A_m, A_{m2}, A_w are the absorption ratio of the CPW conductors, the absorption ratio of the CPW conductors in the region with the microchannel, and the absorption ratio of the water, respectively.

Equations 4-3 through 4-6 are first order approximations. For impedance matched conditions, the equations show that A_w is dependent on position of the microchannel along the length of the CPW with a maximum occurring at the source end because the transmitted power attenuates exponentially along the transmission line. Further, A_w decreases exponentially along the length of the microchannel. Therefore, there is a design tradeoff between the microchannel length, its position relative to the source, and the frequency of operation to obtain a uniform temperature rise and efficient absorption of microwave power. Figure 4-9 shows the distribution of the incident

microwave power in different absorbing structures of deionized H_2O filled device. It shows that A_w increases with frequency in agreement with theory because the power absorbed by water per unit volume is proportional to $f\varepsilon''$ as calculated from Franks [168]. It also shows that the absorption by the metal in the central region (A_{m2}) competes with the absorption by the water (A_w). At low frequencies (< 3.5 GHz), A_{m2} is slightly higher than A_w. The difference between the two becomes negligible as the frequency increases further, and A_w starts to dominate as the frequency exceeds approximately 8 GHz. This can be explained by the differences in the attenuation constants. For instance, α_w is 1.3 times as high as α_{cpw} at 10 GHz. It can be observed from figure 4-9 that the fraction of the incident power absorbed by the CPW conductors, A_m, is noticeably high over the entire frequency range measured. This results in ohmic heating of the CPW conductors, which is also expected to contribute to the temperature rise of the fluid. However, based on the incident power absorbed by the CPW conductors in the center region, A_{m2}, a worst-case first order analytic calculation [169] of the contribution of the metal heating to water heating shows that the power dissipated in the CPW contributes less than 20 % of the total heating observed in the microchannel.

4.3.3.3. Temperature Measurements
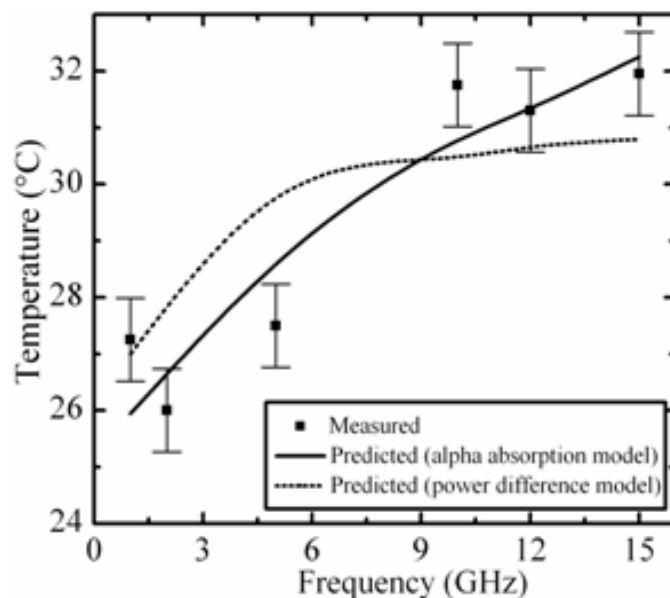
Figure 4-10: The measured temperature (■) of an aqueous solution of 0.2 mmol/L Rhodamine B in a 19 mmol/L carbonate buffer as a function of frequency. The solid line indicates predicted temperature calculated from the alpha absorption model, and the dashed line was calculated by employing the power difference model.

The points (■) in Figure 4-10 show the fluid (aqueous solution of Rhodamine B) temperature measured at various microwave frequencies. The applied power was kept constant at 10 mW. The temperature was measured ~ 250 ms after turning on the microwave power, which was approximated to be within 5% of quasi-thermal equilibrium. The error bars indicate the pooled standard deviation over all measurements for two instances at each frequency added with the estimated standard deviation (0.5 °C) of the room temperature (22.5 °C). The observed temperature rise was 0.88 °C/mW at 12 GHz and 0.95 °C/mW at 15 GHz.

The temperature can also be calculated from the energy absorbed in the water during the heating period dt using equation (4-7)

$$dT = \frac{P_v dt}{\rho C_p V} = \frac{K_e I A_w dt}{\rho C_p V}$$ (4-7)

where ρ and C_p are the density and heat capacity of water, respectively, at appropriate temperature, I is the incident microwave power, A_w is the fraction of the incident power absorbed in the water as shown in figure 4-8, and V is the volume of water in the microchannel. K_e is the channel-heating efficiency, which is defined as the fraction of energy absorbed in the water during the time dt that remains in the water. The rest of the energy absorbed in the water during the time dt is conducted into the substrate. The value of K_e can not be easily obtained from the geometry and thermal properties of the channel and substrate due to the unknown contact thermal resistance (Kapitza resistance) between the water and the hydrophobic surface of the substrate [170]. Rather than attempt to calculate the value of K_e, it was adjusted in a least-squares fit of the predictions of equation (4-7) to the measured data points (■) in Figure 4-10. The solid line in Figure 4-10 indicates the predicted temperature calculated using A_w obtained from Figure 4-8 (alpha absorption model), and the dashed line indicates the predicted temperature calculated using A_w obtained from the power difference model ($A_{H_2O} - A_{empty}$). It is clear from the results of fitting the predictions of the two different absorption models that the alpha absorption model provides a better fit to the measured data. Further, the heating efficiency obtained from the alpha absorption model indicates that only 5 % of the total heat (time integral of the absorbed power) was stored in the fluid while the rest was lost

to the surroundings (PDMS and glass). Because the ratio of stored heat to lost heat increases with decreasing heating time, it is possible to confine most of the heat to the fluid and heat it to a higher temperature by increasing the microwave power and decreasing the heating period simultaneously.

4.4.   Conclusions

The ability to rapidly and selectively control temperature within microchannel environment is crucial for many fluidic applications including high-efficiency PCR and temperature induced cell lysis. In this study, localized microwave dielectric heating of fluids at micrometer scale geometry using an integrated planar microwave transmission line as a power source has been demonstrated. The measured temperature is shown to increase with increasing frequency in agreement with theory. The device used in this study offers several advantages. It is simple, easy to use and fabricate. The planar structure of the transmission line used as a power source lends itself to easy integration with the microchannel and allows for optical interrogation of the microchannel with widely used fluorescence microscopy techniques. The performance of the CPW for heating could be substantially improved by: applying high power pulses over shorter heating times, using a lower thermal diffusivity substrate than glass, and increasing the gap width and thickness of the CPW conductors.

A microwave power absorption model to understand power distribution through the device and to differentiate microwave heating of the fluid from conductive heating of the fluid because of microwave power absorption in thin-film CPW conductors has been developed. This power absorption model has been used to analyze the experimental data

107

and to demonstrate that the temperature rise of fluid is predominantly due to the absorbed microwave power. It is believed that this model can be useful for evaluating the performance of various complex and lossy transmission line configurations, such as CPW, microstrip lines, or striplines, for heating fluid in the microchannel environment.

Finally, it is believed that the microwave dielectric heating approach will be of particular use in rapid thermocycling applications and will lead to new applications exploiting heating in microfluidic environment. Further studies are addressing the use of such heaters for single use, disposable, and integrated microfluidic systems.

5. Summary and Future Directions

5.1. Summary

The advancement of microfluidic technology for providing "sample in – answer out" capabilities to address massive national backlog of unanalyzed DNA samples and ever increasing demand for these assays is critically important. Automation and miniaturization of existing bench-top systems holds the potential to reduce analysis time and cost of performing analysis [7]. Integration of sample preparation steps with electrophoretic separation through miniaturization can solve any external contamination issues that exist due to multiple handling and transfer of samples required by the existing systems. Further, the use of polymeric materials as substrates due to their low material cost and fabrication cost can make the development of disposable microfluidic devices economical, which can not only eliminate cross contamination but also reduce the cleaning time required between subsequent sample runs.

To this effect, the work presented in this dissertation advances several aspects of polymeric microfluidic device for forensic DNA analysis. The overview and background information on forensic DNA analysis along with the motivation of this thesis work is presented in Chapter 1. The technological development regarding DNA analysis for forensic application from its beginning to present is also included in the chapter. Theoretical aspects of electrophoresis - the method of choice for separating billions of nucleotides in human genome - the development of microfluidic devices for PCR

109

amplification, and the development of microfluidic devices for CE separation were presented in the chapter. The review of fabrication methods for microfluidic devices along with the overview of fluorescence detection method was also included in the chapter.

Rapid and robust method for fabrication of microfluidic devices is imperative for successful development of genetic analysis system for forensic application. The work in chapter 2 focuses on the development and characterization of fabrication protocol for solvent bonding polymeric microfluidic devices. A commonly employed hot embossing technique is utilized in this work to form microfluidic channels in PMMA substrate. For microchannel enclosure, this imprinted substrate is clamped together with a blank substrate followed by introduction of small amount of solvent into the microchannel. The difference in capillarity of the microfluidic channel and the interstitial space between the surfaces of the two substrates wicks the bonding solvent into the gap between the substrates causing them to bond. The work presented in the chapter carefully evaluates the effect of the quality and quantity of the bonding solvent on dimensional integrity of the microchannels. Important aspects of the bonding parameters are highlighted for a successful bond formation. The mechanical robustness of the devices bonded using this fabrication protocol is demonstrated by performing bond strength measurements. The functionality of these devices is demonstrated by performing ssDNA separation. The results show that this technique is inexpensive, simple, rapid, and conducive for adaptation to a mass production environment.
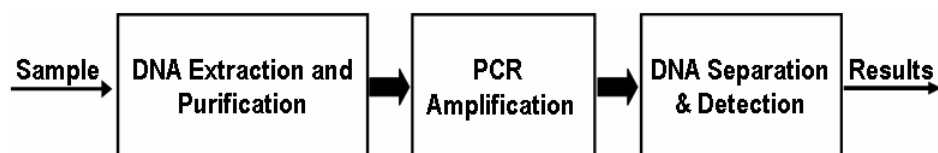
Figure 5-1: Functionalities involved in forensic DNA analysis.

As shown in Figure 5-1 and mentioned in Chapter 1, complete genetic analysis for forensic application depends on successful electrophoretic separation and detection of DNA fragments. It was mentioned in Chapter 2 that electrophoresis has been typically carried out in glass substrates due to extensive information available on these substrates from chromatography and due to well established, well understood surface characteristics, particularly to enhance modifications for improving biomolecular separations. Polymer-based microfluidic devices have been presented as a less expensive alternative to glass substrates; however, due to wide variety and classes of polymeric materials, reports on the surface chemistry and surface interactions with biological molecules have been less extensive. Chapter 3 presented several protocols to modify PMMA surface though chemical and photochemical methods in an attempt to improve ssDNA separation performance. It was demonstrated that twofold improvement can be achieved in DNA separation performance by optimizing wall coating strategies to prevent wall-analyte interactions. The results demonstrated that (1) the ssDNA separation efficiency increases with increasing hydrophilicity of the coating procedures and coating polymers, and (2) the efficiency was limited by the width of the injection plug (theoretically optimal zone for microchip electrophoresis) and that further improvement

would rely on either increasing effective separation channel length or decreasing injection plug width. Finally, these methods are also less time-consuming and less laborious than previously published methods, and they are also conducive to automation for mass production of disposable microfluidic devices.

As mentioned in earlier chapters, the ability to selectively and rapidly control fluid temperature in microfluidic networks is a necessary requirement for PCR amplification and consequently for successful DNA analysis. To this end, the work in Chapter 4 attempts to focus up-stream on genetic analysis functionalities and evaluates the use of microwaves for microfluidic heating applications. This is accomplished by using a thin-film, planar microwave transmission line, coplanar waveguide, as a miniaturized heating source, which was integrated with a polymeric microchannel. The results show that (1) the temperature rise was predominantly due to microwave heating of the fluid, (2) for constant input power the temperature of fluid increased with increasing frequency, as expected from theory, and (3) microwave heating is a viable alternative to resistive-based heating methods for micro scale geometries. A microwave power absorption model was developed to understand power distribution through the device and to characterize the temperature rise of the fluid. A fit of the measured temperature to the predicted temperature obtained using the model was found to be in good agreement. The data also shows that further improvement in temperature would require CPW design to be optimized. It is believed that the microwave power absorption model should be useful for evaluating the performance of various complex and lossy transmission line

configurations such as CPW, microstrip lines, or striplines, for heating fluid in the microchannel environment.

5.2.   Suggestions for Future Work

Generally speaking, future work needs to be directed towards developing modular systems for other functionalities involved in forensic DNA analysis such as cell lysis, DNA purification, and purification of PCR-end product. More importantly, efforts should focus on developing fully integrated microfluidic device.

The solvent-actuated bonding technique presented in Chapter 2 can be used to enclose microchannels of different geometries for many fluidic applications. Based on this work, it is feasible to envision that academic research laboratories with limited resources can study biological and chemical assays in microfluidic channels with ease. One obvious extension of the work presented in Chapter 2 is to extend the method for various commonly used fluidic substrates by finding the appropriate bonding solvent. Another possibility is to bond parallel multi-channel devices where the channel pitch is smaller than the distance penetrated by solvent to ensure that unbonded areas do not occur on such devices.

Future work on surface modification of PMMA microchannels for improved adsorption of wall coating polymers should focus on detailed characterization of surfaces following oxidation. X-ray photoelectron spectroscopic (XPS) [171] analysis should be performed to determine elemental composition of the surface, electronic state of each element at the surface, and uniformity of elemental composition across the surface. The degree to which oxygen is introduced into surfaces will help determine the efficacy of

particular oxidation method in use. Following oxidation and surface coating, atomic force microscopic measurements should be performed to produce three-dimensional surface profile to determine thickness and uniformity of coated surfaces. Both XPS and AFM analyses can be used together to carefully characterize surface passivation schemes for reproducible, high efficiency ssDNA separation, which could be potentially extended to other microfluidic substrates.

One possible extension of microwave dielectric heating for on-chip DNA analysis is temperature induced cell lysis. It was hypothesized in 1954 that a temperature gradient of 0.01 °C across the cell membrane could result in a trans-membrane pressure difference greater than 1 atmosphere, enough for substantial membrane perturbations [172]. It is anticipated that the difference in conductivity of the cytoplasm, from that of the extra cellular fluid, would generate unequal absorption of microwave power and thus non-uniform temperature rise. Moreover, if the incident microwave pluses are of high peak power and short duration such that the cell membrane acts as a capacitor to diffusion of heat, trans-membrane temperature gradients could be set up to burst cell membranes. This should be characterized as rapid cell lysis technique. More importantly, efforts should focus on developing a microfluidic device, capable of microwave actuated thermal cycling, for DNA amplification. Different transmission line designs should be investigated to understand the tradeoff between heating efficiency and temperature uniformity, to support various fluid volumes as well as to understand potential temperature gradients that could be induced due to exponentially decreasing nature of microwave power.

114

Appendix I

Microfabrication Protocols for Silicon Templates

- Start with prime grade, four-inch diameter, <100>-oriented silicon wafer
  - Grow a 100-nm thick wet thermal oxide in a wet tube furnace
- Dehydrate wafer on hotplate
  - 2 or more minutes at 200 ˚C
- Spin adhesion promoter and positive photo resist onto wafer
  - Adhesion promoter: hexamethyldisilazane (HMDS)
  - Photo resist: Shipley Microposit S1813
  - Program spinner:
    - Step 1: 10 seconds at 2500 RPM and 018 ACL
    - Step 2: 20 seconds at 0 RPM and 123 ACL
    - Step 3: 10 seconds at 300 RPM and 010 ACL
    - Step 4: 5 seconds at 500 RPM and 016 ACL
    - Step 5: 40 seconds at 4000 RPM and 030 ACL
  - Deposit about 1 mL HMDS in center of wafer
  - Run program
  - Deposit about 1 mL S1813 in center of wafer during Step 2
- Pre-bake (soft bake) wafer on hotplate
  - 60 seconds at 115 ˚C
  - Remove any resist on wafer back surface inside 3 mm from outside edge
- Expose photo resist with photomask containing the microfluidic channel features
  - Karl Suss MA8 Mask Aligner
  - Dose = 136 mJ/cm^2 = 8 seconds x 17 Watts/cm^2
- Post-bake exposed wafer on hotplate
  - 60 seconds at 115 ˚C
- Develop to remove exposed photo resist
  - Shipley Microposit MF319 Developer
  - Visually determine when development is complete (actual time varies)
  - Rinse thoroughly in DI water
- Examine photo resist pattern under microscope for defects
  - Reject if there is an obvious defect in any channel
- Remove thermal oxide not protected by photo resist
  - JT Baker 6:1 BOE (Buffered Oxide Etch)
  - 1.5 minutes (nominal etch rate of 80 nm per minute plus margin)
  - Rinse thoroughly in DI water
- Remove unexposed photo resist
  - Shipley Microposit Remover 1165

- Visually determine when removal is complete
- Rinse thoroughly in DI water
- Saw wafers to fit silicon etching vessel if necessary
  - Cure oversize (~10 mm) to provide margin for final cuts
- Remove silicon not protected by thermal oxide
  - 1 part 25% (wt) tetramethylammonium hydroxide (TMAH) to 2 parts DI water
  - 65 minutes at 80 ˚C to remove about 60 µm
  - Rinse thoroughly in DI water
- Remove thermal oxide from unetched silicon
  - Shipley Buffered oxide etch (BOE)
  - 1.5 minutes
- Saw template to final size

APPENDIX II

Microwave Power Absorption in Low-Reflectance, Complex, Lossy Transmission Lines

1   Introduction

The possibility of microwave heating of lossy fluids in microfluidic devices with integrated transmission lines has been demonstrated recently [155, 156]. To optimize the performance of microwave heating in these types of devices, it will be necessary to distinguish between the absorption of microwave power in fluids in the microchannel and the absorption of microwave power in the metal components of the transmission line.

The standard way to calculate the power absorbed in a transmission line [173] requires knowledge of the real and imaginary components of the propagation constants of the transmission lines connected to the transmission line being modeled. But it is possible that this type of information will not be available for transmission lines that are integrated with microfluidic devices. Therefore, it may be desirable to be able to analyze S-parameter measurements of this type of device without access to the type of data needed for the model described in [173].

In general, the reflection and transmittance spectra of a complex transmission line will have interference fringes due to inter-reflections between discontinuities in the transmission line. However, the fringes will be small perturbations on the spectra when all of the reflection coefficients are small, which is usually a design goal. In this case, it

should be possible to ignore the phase information that is necessary to describe the amplitude and spacing of the interference fringes.

The purpose of this study is to develop approximations for the microwave power absorbed in lossy components of a three-region transmission line just from S-parameter reflectance and transmittance amplitude measurements. It is expected that the results will be useful when the amplitude of the fringes on the absorption spectra are small compared to the effects of interest as illustrated by application of the results derived here to experimental data on a real device.

Section 2 of this study derives equations for the fractions of power reflected from, transmitted through, and absorbed in each region of a transmission line made up of three different homogeneous regions with a single reflective boundary. In other words, the reflection coefficients at all but one of the region boundaries are assumed to be zero. Section 3 derives equations for the same quantities when symmetric pairs of the four boundaries are equally reflective. These equations express the S-parameter data in terms of attenuation coefficients within the different regions of the transmission line and the reflection coefficients at the boundaries of the transmission-line regions. Section 4 inverts these equations to express the reflection and attenuation coefficients in terms of the S-parameter data. The resulting equations are then used to analyze experimental data from a three-region transmission line that contains a microfluidic channel in its middle region.

2   Absorption in transmission lines with a single reflective boundary
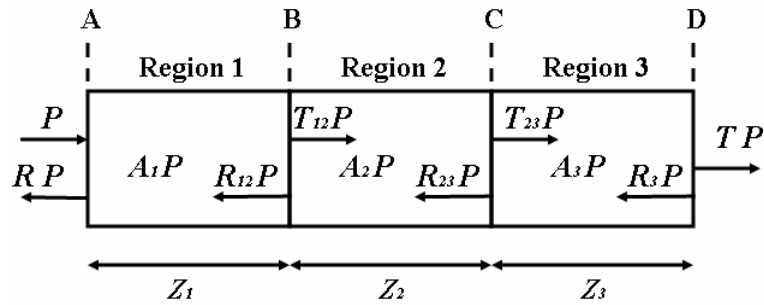
Figure A-0-1: A complex transmission line consisting of three regions showing power propagation in each direction.

Figure A-0-1 illustrates a generic transmission line that consists of three regions of length Z_1, Z_2, and Z_3, respectively, which are separated by boundaries labeled by A, B, C, and D. The geometry and dielectric constants of all of the structures that make up each of the regions are assumed to be uniform within each region. It is also assumed that microwave power propagates along the transmission line with no loss due to emission of radiation. Finally, it is assumed that regions 1 and 3 have identical microwave properties and that the two transmission lines (not shown) to which the microwave probes are connected have identical microwave properties.

Let P be the power incident on Boundary A from the left, and let RP be the power leaving Boundary A to the left. Similarly, let TP be the power transmitted to the right from Boundary D. Now assume that R and T, which will be called the reflection and transmission, respectively, are the only experimental data available for the device of Fig. A-0-1. Further assume that the real and imaginary parts of the propagation constants of the transmission lines (not shown) that are connected to the device shown in Fig. A-0-1 as well as those of the three regions in that device are not known. In this case, there is

not enough information available to invert Maxwell's equations to determine the propagation and attenuation constant in the regions of the device (Fig. A-0-1) and in the transmission lines to which it is attached. This remains true even if Regions 1 through 3 are assumed to be have identical properties and the transmission lines attached to the device (Fig. A-1) are assumed to be identical.

In this case it is convenient to treat the transmission line in Fig. A-0-1 as a power-flow problem [174]. A fraction RP of the incident power is reflected at Boundary A, a fraction A_1P is absorbed in Region 1, a fraction $T_{12}P$ is transmitted across Boundary B, and a fraction $R_{12}P$ is reflected at this boundary. Similar descriptions apply to Regions 2 and 3, and finally a fraction TP is transmitted out the right side of the transmission line at Boundary D. By conservation of energy, $A = A_1 + A_2 + A_3 = 1 - R - T$ is the fraction of the power incident on the transmission line that is absorbed by the transmission line. R and T can be obtained directly from S-parameter measurements, and A can be calculated from R and T.

On the other hand, A_1, A_2, and A_3 are complex functions of the microwave power-reflection coefficients and the phase differences between the microwave amplitudes reflected at and transmitted across the different boundaries. In general, these quantities are described by Maxwell's equations. However, if interference between multiply reflected waves in the transmission line introduces only small effects (fringes on the absorption spectra) compared to the effects of interest, then simpler descriptions are possible. These are based on ray tracing, knowledge of the general nature of the solutions of Maxwell's equations in homogeneous lossy regions, conservation of energy,

and a number of independent reflection and transmission measurements equal to or greater than the number of unknown parameters. This idea is developed in the following two sections.

2.1   Reflection only at Boundary A

First assume that the power-reflection coefficients at Boundaries B, C, and D are all zero, then $R_{12} = R_{23} = R_3 = 0$. In this case,

$$T = [1 - \rho]\tau_1\tau_2\tau_3 = 10^{(S_{21}/10)} \tag{A-1}$$

$$R = \rho = 10^{(S_{11}/10)} \tag{A-2}$$

$$A_1 = [1 - \rho][1 - \tau_1] \tag{A-3}$$

$$A_2 = [1 - \rho]\tau_1[1 - \tau_2] \tag{A-4}$$

$$A_3 = [1 - \rho]\tau_1\tau_2[1 - \tau_3] \tag{A-5}$$

$$\tau_n = \exp^{(-2\alpha_n Z_n)} \tag{A-6}$$

In these equations, S_{11} and S_{21} are the respective reflection and transmission coefficients in dB, ρ is the power-reflectance coefficient S_{11} at Boundary A, and α_n for $n = 1,..., 3$ are the amplitude-attenuation coefficients for Regions 1-3, respectively. Even though the order of the factors in these equations is not important, it simplifies tracing the flow of power through the device.

The amplitude absorption coefficient of a material, which is often denoted by α, should not be confused with the amplitude attenuation coefficient α_n of Region n of the transmission lines being considered here. Two times the amplitude absorption coefficient of a material, which can be calculated from the complex dielectric constant of that

121

material, describes the power attenuation per unit distance of a collimated wave of electromagnetic radiation propagating through a homogeneous slab of that material. On the other hand, two times α_n describes the power attenuation per unit distance of a guided wave of radiation propagating in Region n of a complex transmission line. In general α_n will depend upon both the geometry and the frequency-dependent complex dielectric constants of all of the structures that make up Region n of the transmission line.

2.2 Reflection only at Boundary B

Simple equations like A-1 to A-5 are rigorously true, without regard to the phase relations of the microwave amplitude, only when all but one of the reflection coefficients are zero. For instance, let ρ be the power reflection coefficient at Boundary B, and let all of the other reflection coefficients be zero. In this case, eqs. A-2 and A-3 must be replaced by

$$R = \tau_1 \rho \tau_1 \tag{A-7}$$

$$A_1 = [1 - \tau_1] + \tau_1 \rho [1 - \tau_1] \tag{A-8}$$

while the other equations remain valid.

2.3 Reflection only at Boundary C

If ρ is the power reflection coefficient at Boundary C and all of the other reflection coefficients are zero, then eqs. A-2 to A-4 must be replaced by

$$R = \tau_1 \tau_2 \rho \tau_2 \tau_1 \tag{A-9}$$

$$A_1 = [1 - \tau_1] + \tau_1 \tau_2 \rho \tau_2 [1 - \tau_1] \tag{A-10}$$

$$A_2 = \tau_1 [1 - \tau_2] + \tau_1 \tau_2 \rho [1 - \tau_2] \tag{A-11}$$

2.4 Reflection only at Boundary D

Continuing in the same vein, if ρ is the power reflection coefficient at Boundary D and all of the other reflection coefficients are zero, then eq. A-1 is still valid, but eqs. A-2 to A-5 must be replaced by

$$R = \tau_1 \tau_2 \tau_3 \rho \tau_3 \tau_2 \tau_1 \tag{A-12}$$

$$A_1 = [1 - \tau_1] + \tau_1 \tau_2 \tau_3 \rho \tau_3 \tau_2 [1 - \tau_1] \tag{A-13}$$

$$A_2 = \tau_1 [1 - \tau_2] + \tau_1 \tau_2 \tau_3 \rho \tau_3 [1 - \tau_2] \tag{A-14}$$

$$A_3 = [1 - \tau_1] + \tau_1 \tau_2 \tau_3 \rho [1 - \tau_3] \tag{A-15}$$

3 Absorption in transmission lines with two reflective boundaries

In the case where the amplitude of any two of the reflection coefficients is non-zero, it is still possible to derive good approximations to the reflectance and transmittance based on power flow if the effects of interference are small compared to the effects of interest. Practically speaking, this means that the reflectance coefficients will be small compared to one, which is equivalent to requiring good impedance matching at all boundaries. When the impedance matching is poor, there will be large fringes on the S_{11} and S_{21} spectra due to interference between multiply reflected waves propagating on the transmission line. On the other hand, when the impedance matching is good, the fringes will be barely visible compared to the effects of interest in the spectra.

In the approach used here [174], the powers in multiply reflected waves are simply added, which washes out all interference effects and produces a result intermediate between the envelope of the fringe maxima (constructive interference) and the envelope of the fringe minima (destructive interference) in the S-parameter

measurements. If the interference effects are large compared to the effects of interest, then the errors introduced by this approximation will be large. On the other hand, when the fringes are small compared to the effects of interest, then equations derived here will provide useful approximations.

3.1 Reflection only at Boundaries A and D

Continue to assume that Regions 1 and 3 have identical properties and that ρ is the power reflection coefficient at each probe. To derive a general expression, it is necessary to have expressions for the reflectance of the transmission line at the left probe and the transmittance of the transmission line at the right probe. These can be derived by expressing A_1, A_2, and A_3 as well as R and T as an infinite series of terms, each term describing the power in a wave that has been multiply reflected a different number of times, and summing the series analytically to produce closed-form expressions:

$$R = \frac{\rho[1 + \tau^2(1 - 2\rho)]}{1 - \rho^2\tau^2} \approx \rho[1 + \tau^2] \tag{A-16}$$

$$T = \frac{(1 - \rho)^2\tau}{1 - \rho^2\tau^2} \approx [1 - 2\rho]\tau \tag{A-17}$$

$$A_1 = \frac{[1 - \rho][1 - \tau_1][1 + \tau_1\tau_2\tau_3\rho\tau_3\tau_2]}{1 - \rho^2\tau^2} \approx [1 - \tau_1][1 - \rho + \tau_1\tau_2\tau_3\rho\tau_3\tau_2 \tag{A-18}$$

$$A_2 = \frac{[1 - \rho]\tau_1[1 - \tau_2][1 + \tau_2\tau_3\rho\tau_3]}{1 - \rho^2\tau^2} \approx [1 - \tau_2]\tau_1[1 - \rho + \tau_2\tau_3\rho\tau_3] \tag{A-19}$$

$$A_3 = \frac{[1 - \rho]\tau_1\tau_2[1 - \tau_3][1 + \tau_3\rho]}{1 - \rho^2\tau^2} \approx [1 - \tau_3]\tau_1\tau_2[1 - \rho + \tau_3\rho] \tag{A-20}$$

$$\tau = \tau_1\tau_2\tau_3 \tag{A-21}$$

124

The approximations on the right hand side of eqs. A-16 and A-20 were chosen to conserve energy as well as to be accurate to order ρ^2. They will be useful when $\rho^2 \ll 1$. They could also have been derived by ray tracing [174] to generate all terms linear in ρ without recourse to the sum of the series of all ray-tracing terms.

3.2   Reflection only at Boundaries B and C

As another alternative reflection model, assume again that Regions 1 and 3 have identical properties but that ρ is the power reflection coefficient at Boundaries B and C of Region 2.   In this case the only expressions that need to derived by the procedure described above are those for R_{12} and T_{23} because A_1, A_2, and A_3 can be expressed in terms of these quantities as shown below:

$$R_{12} = \frac{\rho[1 + \tau_2^2 (1 - 2\rho)]}{1 - \rho^2 \tau_2^2} \approx \rho[1 + \tau_2^2] \qquad \text{(A-22)}$$

$$T_{23} = \frac{(1 - \rho)^2 \tau_2}{1 - \rho^2 \tau_2^2} \approx [1 - 2\rho]\tau_2 \qquad \text{(A-23)}$$

$$R = \tau_1 R_{12} \tau_1 \approx \tau_1^2 \rho[1 + \tau_2^2] \qquad \text{(A-24)}$$

$$T = \tau_1 T_{23} \tau_3 \approx \tau_1 \tau_2 \tau_3 [1 - 2\rho] \qquad \text{(A-25)}$$

$$A_1 = [1 - \tau_1][1 + \tau_1 R_{12}] \qquad \text{(A-26)}$$

$$A_2 = \tau_1[1 - R_{12} + T_{23}] \qquad \text{(A-27)}$$

$$A_3 = \tau_1 T_{23}[1 - \tau_3] \qquad \text{(A-28)}$$

125

The approximations on the right hand side of eqs. A-22 and A-23 conserve energy, are accurate to order ρ^2, and will be useful when $\rho^2 << 1$. These approximations could also have been derived directly from ray tracing.

The extension of this type of analysis to three or more reflecting boundaries for all powers of ρ probably becomes impractically complex. On the other hand, ray tracing to generate all terms linear in ρ appears relatively straightforward. But the result will be useful only when the interference effects are small compared to the effects of interest.

4   Examples
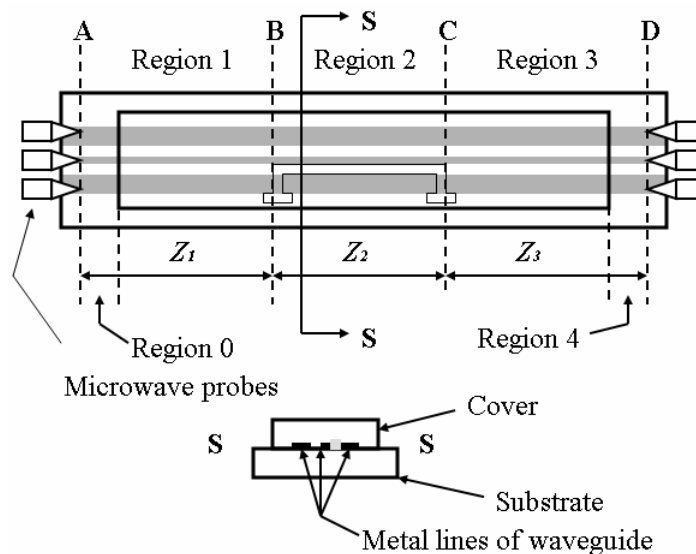
Figure A-0-2: Top view and side view of coplanar waveguide transmission line.

Chapter 4 describes in detail an application of the equations given above. Figure A-0-2 shows a top and a side view of the coplanar-waveguide transmission line of

Chapter 4. It is comprised of metal lines on a borosilicate glass substrate and a rectangular poly-dimethylsiloxane (PDMS) cover attached to the transmission line by contact adhesion. Region 1 of the transmission line extends from the microwave probes on the left side of the transmission line to the left end of the microchannel. Region 2 extends from the left end to the right end of the microchannel. Region 3 extends from the right end of the microchannel to the microwave probes on the right side of the transmission line. Regions 0 and 4 extend from the microwave probes to the closest end of the cover, respectively.
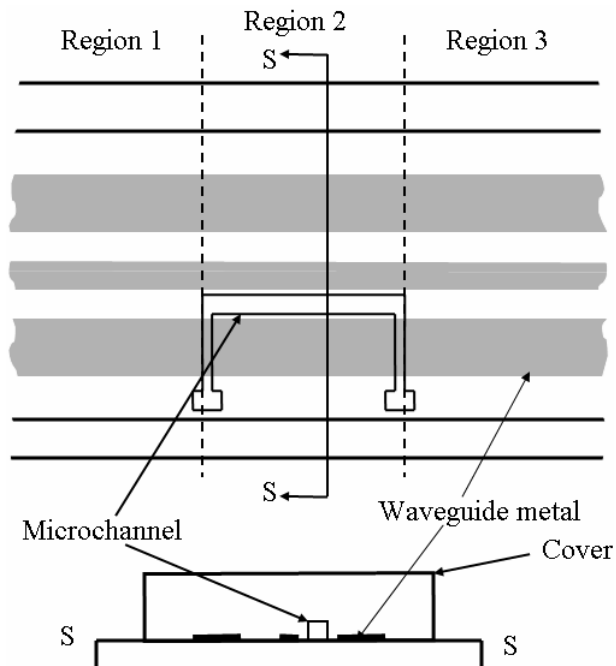
Figure A-0-3: Close up view of removable cover of Figure A-0-2 showing that the cover contains the microchannel.

Figure A-0-3 is a close up view of Fig. A-0-2 that shows the microchannel that is located in the cover over the coplanar waveguide. The figure is not to scale, and the channel cross section, which is actually trapezoidal, is only shown schematically.
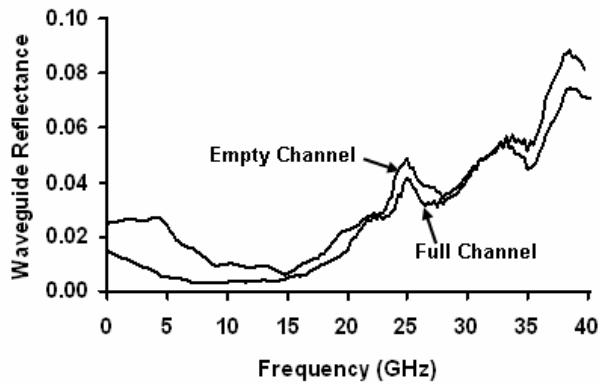
Figure A-0-4: Reflectance spectra of the coplanar waveguide device described in Chapter 4.
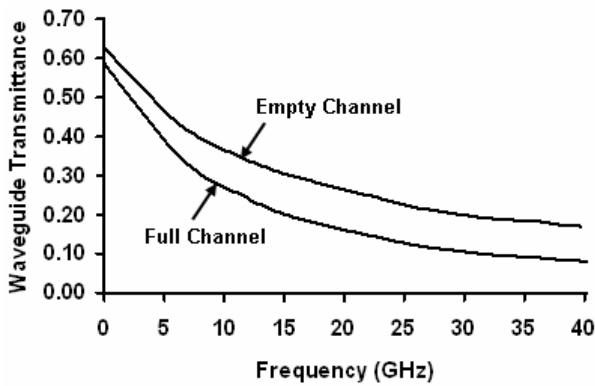
Figure A-0-5: Transmittance spectra of the coplanar waveguide device described in Chapter 4.

Figure A-0-4 plots the measured transmittance-line reflectance spectra when the microchannel in Fig. A-0-3 was empty and when it was full of de-ionized (DI) water. Figure A-0-5 plots the transmittance spectra for the same configurations of the transmission line. Most of the features on the reflectance spectra are probably interference fringes caused by multiple reflections between the boundaries of the homogeneous regions in the transmission line. Any interference fringes present in the transmission data are much less pronounced than on the reflection data due to the different scale on the y-axes in these two figures.

Over the frequency range of Figures A-0-4 and A-0-5, borosilicate glass and PDMS are approximately lossless (do not absorb microwave power) and have dielectric constants not very different from air when compared with those of gold and water. Therefore, the first assumption needed to apply the above equations to the transmission line of Fig. A-0-2 is that the transmission line properties in Regions 0, 1, 3, and 4 in Fig. A-0-2 are identical. This is illustrated by showing Region 0 as a subset of Region 1 and Region 4 as a subset of Region 3 in Fig. A-0-2. Thus the three-region transmission line of Fig. A-0-1 approximates the five-region transmission line of Fig. A-0-2 for the analysis presented here.
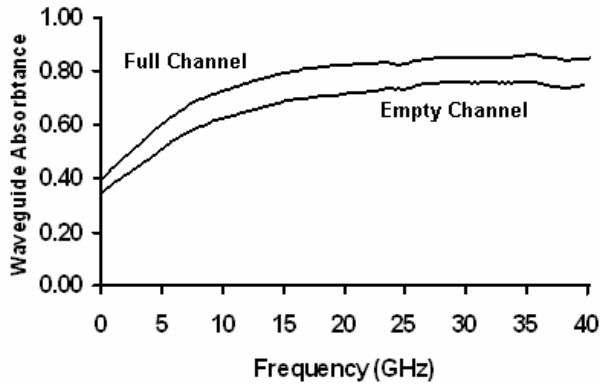
Figure A-0-6: Absorption spectra of coplanar waveguide device described in Chapter 4.

Figure A-0-6 plots the empty-channel and full-channel absorption spectra of the device described in Chapter 4

$$A_e = 1 - R_e - T_e \qquad\qquad (A\text{-}29)$$

$$A_f = 1 - R_f - T_f \qquad\qquad (A\text{-}30)$$

respectively, where the subscript e refers to the empty-channel data, and the subscript f refers to the full channel data. Any interference fringes on the empty and full-channel absorption spectra below about 25 GHz are very small compared to the difference between the two spectra. This fact suggests that the approximate equations derived here, which ignore interference effects, can be used to calculate the fraction of the incident microwave power that is absorbed in the channel water with little error due to interference effects below this frequency. Features that may be interference fringes are more evident above 25 GHz, but they are still relatively small compared to the difference between the absorption spectra, so the errors incurred will be relatively small even in this spectral region.

130

4.1   Difference in absorbed-power fractions

The simplest estimate of the fraction of the microwave power incident on the filled transmission line that is absorbed in the water in the microchannel is the difference between the fraction of the power absorbed when the channel is full and when it is empty, which is given by

$$\Delta A = A_f - A_e = R_e + T_e - R_f - T_f \qquad \text{(A-31)}$$

However, as will be shown below, this is only a lower bound to the fraction of the power absorbed in the microchannel water and can greatly underestimate the actual fraction absorbed.

4.2   Reflection only from the left boundary of Region 1

To derive a more accurate approximation, further assumptions about the transmission line are required. For instance, it can be assumed that eqs. A-1 through A-5 describe the empty device. In other words, $R_{12} = R_{23} = R_3 = 0$ and $\rho \neq 0$ is the power reflection coefficient at the left boundary of Region 1. Let $R = R_e$ and $T = T_e$ be the measured reflectance and transmittance for the empty transmission line in eqs. A-1 and A-2. In this case, these equations can be combined to give the attenuation coefficient of the empty transmission line as

$$\alpha_m = \frac{-1}{2[Z_1 + Z_2 + Z_3]} \ln\left(\frac{T_e}{1 - R_e}\right) \qquad \text{(A-32)}$$

and A_{1em}, A_{2em}, and A_{3em} can be calculated from eqs. A-3 to A-5, and A-32 with $\alpha_1 = \alpha_2 = \alpha_3 = \alpha_m$. Here the numeric subscripts designate the region, the subscript e designates the

131

empty transmission line, and the subscript m designates absorption due to the metal conductors.

Now let $R = R_f$ and $T = T_f$ be the measured reflectance and transmittance calculated from the S parameters when the channel is filled with DI water. The next assumption required is that the transmission line attenuation coefficient due to the metal conductors does not change when the microchannel in the transmission line is filled with water. This is a good approximation provided that the addition of the water does not substantially change the field distribution on the surface of the metal conductors even if it changes the distribution significantly in the middle of the channel. Regions 1 and 3 are still identical, and $\alpha_1 = \alpha_3 = \alpha_m$, but $\alpha_2 = \alpha_m + \alpha_w$, where α_w is the portion of the attenuation coefficient of the transmission line in Region 2 due to the additional absorption by the water in the channel. In this case, eqs. 1 and 2 can be combined to give

$$\alpha_w = \frac{-1}{2Z_2}\{\ln\left(\frac{T_f}{1-R_f}\right) - 2\alpha_e[Z_1 + Z_2 + Z_3]\} \tag{A-33}$$

and A_{1fm}, A_{2fm}, A_{2fw}, and A_{3fm} can be calculated from eqs. A-3 to A-5, A-32, and A-33 with $\alpha_1 = \alpha_3 = \alpha_m$ and $\alpha_2 = \alpha_m + \alpha_w$. Again, the numeric subscripts designate the region, but the subscript f designates the filled transmission line, and the subscript w designates absorption due to the water in the microchannel.

Table 0-1: Measured and calculated parameters for the device described in Chapter 4 at 5.02 GHz. The subscript numbers correspond to the different regions. The subscripts e and f correspond to an empty channel and a channel filled water, respectively, and the subscripts m and w correspond to the metal conductors and channel water.

Condition	Parameter	Value	Unit
Empty Channel	S_{11e}	-15.9956	dB
	S_{21e}	-3.24646	dB
	R_e	0.025144	
	T_e	0.473537	
	α_m	0.240687	cm^{-1}
	A_{1em}	0.233569	
	A_{2em}	0.118546	
	A_{3em}	0.149204	
	$R_e+T_e+A_{1em}+A_{2em}+A_{3em}$	1.000000	
Filled Channel	S_{11f}	-22.6425	dB
	S_{21f}	-3.97558	dB
	R_f	0.005442	
	T_f	0.400352	
	α_w	0.259523	cm^{-1}
	A_{1fm}	0.238289	
	A_{2fm}	0.110560	
	A_{2fw}	0.119212	
	A_{3m}	0.126145	
	$R_f+T_f+A_{1fm}+A_{2fm}+A_{2fw}+A_{3fm}$	1.000000	

Table 0-1 presents the results of applying eqs. A-32 and A-33 to S-parameter data measured at 5 GHz as shown in Chapter 4. The first and second sections of the table compare the measured and calculated parameters for the empty transmission line and the transmission line filled with DI water, respectively. First note that the calculation conserves power in that the sum of the reflected, transmitted, and absorbed fractions of the incident power is one. Also note that $R_f \neq R_e$, which shows that at least one parameter

changed when the transmission line was filled with water and also explains why $A_{1f} \neq A_{1e}$ in Table 0-1.

Also in Table 0-1, notice that $T_f \neq T_e$ and $A_{2f} \neq A_{2e}$. A small fraction of this difference is attributable to violations of the assumptions on which the analysis was based. But the main contributor is the large difference between the attenuation coefficients $\alpha_2 = \alpha_m$ for the empty channel case, and $\alpha_2 = \alpha_m + \alpha_w$ when the channel is filled with water. In other words, filling the microchannel with water has doubled the absorption (attenuation) in Region 2, with about half of the power being absorbed in the metal conductors and the other half being absorbed in the water in that region.

More precisely, the fraction A_{2fm} of the power absorbed in the Region 2 metal of the full-channel transmission line is only about 93 % as large as the fraction A_{2em} absorbed in the empty-channel transmission line. This difference is not the result of experimental error or a violation of the assumptions used in deriving the model. Instead, this difference is to be expected. When the water is present, the microwave power decreases more rapidly with distance along the channel than when the channel is empty due to the addition of water absorption to the metal absorption. Therefore, less power is available for the metal in Region 2 to absorb when the channel is full than when it is empty. In other words, water absorption competes with metal absorption in Region 2 when the channel is full of water.
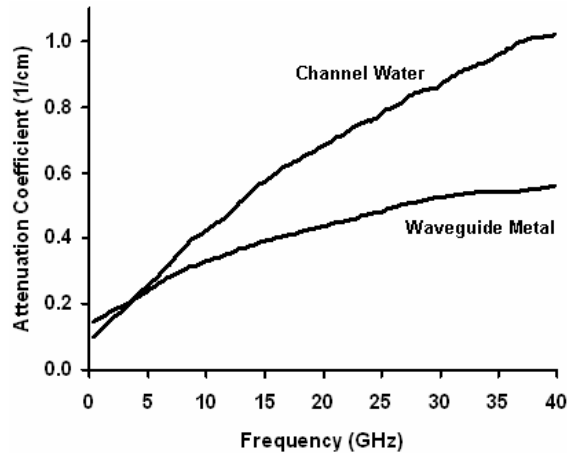
Figure A-0-7: Microwave attenuation coefficient data for the metal conductors and the channel water for the coplanar waveguide described in Chapter 4.

Figure A-0-7 compares the amplitude-attenuation coefficients for the metal conductors α_m and the channel water α_w that were calculated from the measured reflectance and transmittance spectra as illustrated in Table 0-1. Inspection of Fig. A-0-7 reveals that interference fringes are evident in both spectra, but are most obvious in the α_w spectrum. These are almost certainly artifacts of ignoring interference among multiple reflections in the approximate equations, but the error introduced by this approximation is small compared to the major trends in the spectra.

4.3   Alternative Assumptions and Comparison of Results

The model given in eq. A-31 of Section 4.1 can be rewritten as

$$A_{2\,fw} = \Delta A \tag{A-34}$$

in terms of the definitions given in connection with Table 0-1. For comparison with other models considered in this paper, the model of Section 4.1 will be referred to as Model (a).

135

Similarly, the model discussed in Section 4.2 that is based on the assumption that only the reflection coefficient at the left probe is non-zero will be referred to as Model (c). As alternatives to these models, the reflection coefficients might be assumed to be

(b) zero because they are small,

(d) non-zero only at the left end of the microchannel,

(e) non-zero only at both probes,

(f) non-zero only at both ends of the microchannel,

(g) non-zero only at the right end of the microchannel,

(h) non-zero only at the right probe.

These possibilities will be considered next. For case (b), which assumes that all reflection coefficients are zero, the same equations used in Section 4.2 can be used with the assumption that $R_e = R_f = 0$. For case (h), eqs. A-1 and A-12 can be combined to eliminate $\tau_1 \tau_2 \tau_3$ in these equations with the result

$$\rho = \frac{2R + T^2 - \sqrt{T^4 + 4RT^2}}{2R} \tag{A-35}$$

which can be substituted first into eq. A-32 to determine α_m and then along with α_m into eq. A-33 to determine α_w.

Closed form solutions are not possible for the remaining equations, so they must be solved numerically. For case (d), which assumes non-zero reflection only at the left end of the microchannel, the approximations on the right hand side of eqs. A-7 and A-1 can be combined to eliminate ρ to give,

$$\frac{R}{\tau_1 \tau_2} + \frac{T}{\tau_1 \tau_2 \tau_3} = 1 \tag{A-36}$$

which can then be solved numerically, first for α_m in terms of R_e and T_e and then for α_w in terms of α_m, R_w, and T_w.

For case (g), which assumes non-zero reflection only at the right end of the microchannel, the approximations on the right hand side of eqs. A-9 and A-1 can be combined to eliminate ρ to give,

$$\frac{R}{\tau_1^2 \tau_2^2} + \frac{T}{\tau_1 \tau_2 \tau_3} = 1 \tag{A-37}$$

which can then be solved numerically, first for α_m in terms of R_e and T_e and then for α_w in terms of α_m, R_w, and T_w.

For case (e), which assumes non-zero reflection only at both probes, the approximations on the right hand side of eqs. A-16 and A-17 can be combined to eliminate ρ to give,

$$\frac{2R}{[1 + \tau_2^2]} + \frac{T}{\tau_1 \tau_2 \tau_3} = 1 \tag{A-38}$$

which can then be solved numerically, first for α_m in terms of R_e and T_e and then for α_w in terms of α_m, R_w, and T_w.

For case (f), which assumes non-zero reflection only at both ends of the microchannel, the approximations on the right hand side of eqs. A-24 and A-25 can be combined to eliminate ρ to give,

$$\frac{2R}{\tau_1^2 [1 + \tau_2^2]} + \frac{T}{\tau_1 \tau_2 \tau_3} = 1 \tag{A-39}$$

which can then be solved numerically, first for α_m in terms of R_e and T_e and then for α_w in terms of α_m, R_w, and T_w.

Table A-0-2: Measured coplanar waveguide reflectance and transmittance at three frequencies.

Frequency	R_e	T_e	R_f	T_f
5 GHz	0.025144	0.473537	0.005442	0.400352
15 GHz	0.006318	0.308259	0.004613	0.203731
23 GHz	0.028247	0.244598	0.02854	0.142578

Table A-0-2 lists values of R_e and T_e obtained at 5 GHz, 15 GHz, and 23 GHz for

the coplanar waveguide device described in Chapter 4.

Table A-0-3: Comparison of results from the different models described in this appendix. The results in the column labeled by ρlp are based on the assumption that the reflection coefficient at the left probe was non-zero. Similarly, the results in the column labeled by ρrc are based on the assumption that the reflection coefficient at the right end of the channel is non-zero, etc.

Condition	Parameter	ΔA (a)	All zero (b)	ρ_{lp} (c)	ρ_{lc} (d)	$\rho_{lp} = \rho_{rp}$ (e)	$\rho_{lc} = \rho_{rc}$ (f)	ρ_{rc} (g)	ρ_{rp} (h)
					Non-Zero Reflection Coefficients				
5GHz Empty Channel	ρ_e		0.0000	0.0251	0.0429	0.0202	0.0249	0.0590	0.0924
	α_m		0.2492	0.2407	0.2346	0.2354	0.2322	0.2289	0.2169
	A_{2em}		0.1243	0.1185	0.1145	0.1186	0.1183	0.1236	0.1190
5 GHz Full Channel	ρ_f		0.0000	0.0054	0.0093	0.0047	0.0063	0.0194	0.0318
	α_w		0.2319	0.2595	0.2789	0.2759	0.2850	0.2888	0.3211
	A_{2fm}		0.1147	0.1106	0.1076	0.1087	0.1074	0.1079	0.1029
	A_{2fw}	0.0929	0.1068	0.1192	0.1279	0.1274	0.1319	0.1191	0.1524
15 GHz Empty Channel	ρ_f		0.0000	0.0063	0.0152	0.0058	0.0097	0.0263	0.0589
	α_m		0.3928	0.3902	0.3871	0.3884	0.3858	0.3834	0.3720
	A_{2em}		0.1582	0.1569	0.1549	0.1569	0.1568	0.1598	0.1576
15 GHz Full Channel	ρ_f		0.0000	0.0046	0.0111	0.0044	0.0089	0.0426	0.0917
	α_w		0.5720	0.5744	0.5778	0.5757	0.5742	0.5488	0.5230
	A_{2fm}		0.1309	0.1298	0.1283	0.1296	0.1292	0.1333	0.1325
	A_{2fw}	0.1062	0.1907	0.1911	0.1916	0.1922	0.1923	0.1908	0.1862
23 GHz Empty Channel	ρ_e		0.0000	0.0282	0.0773	0.0265	0.0495	0.1354	0.2591
	α_m		0.4694	0.4598	0.4425	0.4512	0.4346	0.4209	0.3694
	A_{2em}		0.1689	0.1631	0.1529	0.1635	0.1624	0.1789	0.1673
23 GHz	ρ_f		0.0000	0.0285	0.0779	0.0278	0.0641	0.2791	0.4396

Full Channel	α_w		0.7455	0.7452	0.7446	0.7416	0.7001	0.4944	0.3599
	A_{2fm}		0.1325	0.1279	0.1198	0.1278	0.1262	0.1579	0.1517
	A_{2fw}	0.1018	0.2104	0.2072	0.2015	0.2101	0.2032	0.1855	0.1478

Table A-0-3 compares the results of applying the different models derived above to the data in Table A-0-2. The approximation $A_{2fw} = \Delta A$ of eqs. A-31 and A-34, which is the simplest estimate of the fraction of the microwave power absorbed in the water, is also shown in the table for comparison. First notice that this estimate is significantly smaller at all three frequencies than that based on the other approximations discussed in this paper. This is a general result because ΔA completely ignores the competition between the water and metal absorption processes, which reduces the total amount of power absorbed in the metal when the water is present, as discussed previously.

The data at different frequencies (Table A-0-3) illustrate different relations among the empty-channel and full-channel transmission-line reflectances R_e and R_f. The values of R_e and R_f are given in Table A-0-2, but they are also given by ρ_e and ρ_f under (c) in the Table A-0-3 because this is the case where the only reflection occurs at the left probe. At 5 GHz, R_e is "big" (≈ 0.025) while R_f is "small" (≈ 0.005) and A_{2fw} is "small" (≤ 0.15). At 23 GHz, R_e, R_f, and R_f - R_e are "small," and A_{2fm} is "large" (≥ 0.15). At 15 GHz, both R_e and R_f and their difference are "small," but A_{2fw} is "large."
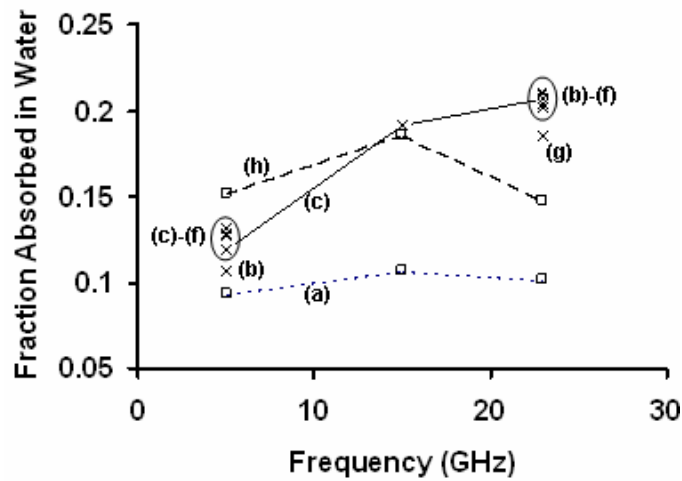
Figure A-0-8: Comparison of the fraction of the incident microwave power absorbed by the water in the channel in the transmission line described in Chapter 4. (a)-(h) represent models described here.

Figure A-0-8 compares the fraction A_{2fw} of the incident power that is absorbed in the microchannel water as calculated with the different models. Models (a) and (h) are plotted with squares, and the other models are plotted with times signs. The data points for (a) and (h) are connected with dashed lines, and the data points for (c) are connected with solid lines. An ellipse encircles a cluster of data points at 5 GHz, and another ellipse encircles a cluster of data points at 23 GHz. The cluster is so tight at 15 GHz, that no ellipse is needed. The models that have at least one non-zero reflection coefficient on the left side of the microchannel (c-f) agree among themselves significantly better than the other models. Also (b), which is based on assuming all reflection coefficients to be zero, agrees much better with these than do the models that assume non-zero reflection coefficients only to the right side of the microchannel. The reasons for and implications of these facts are discussed in the next section.

140

5   Discussion and conclusion

Equations that describe the absorption of microwave power in the lossy components of a complex transmission line have been derived for a number of simplified models of the general three-region transmission line. Examples of the use of these equations to estimate the fraction of the power absorbed in the water in a microchannel embedded in a transmission line were described. These examples required three assumptions common to all of the examples. First it was assumed that each transmission line could be divided into three homogeneous regions extending from the probes on one side of the device to the probes on the other side of the device. Second, it was assumed that the metal conductors and channel water are the only lossy components of the transmission line. Third, it was assumed that the portion of the attenuation coefficient of the transmission line that describes absorption of microwave power in the metal conductors did not change when the channel was filled with water. This is a good assumption if the presence of the water does not significantly change the field distribution on the surface of the metal conductors.

For some of the examples, it was further necessary to assume that the reflections at three of the four region boundaries in the transmission line were zero even though what appeared to be interference fringes on the transmission line reflectance spectra suggest that this is not the case. The results derived for these examples are rigorous. For two of the examples, (e) and (f), it was assumed that reflections at two of the four discontinuities were zero. These models are the most realistic because they assume identical reflection coefficients at pairs of boundaries that are mirror images of each other and should

therefore be identical in theory, and similar in practice. On the other hand, the results based on these models are accurate only to the extent that interference effects are negligible, and then only to order ρ^2, which will be more than adequate in many applications.

At the three frequencies for which data are reported in Fig. A-0-8, the results of four of the models (c-f) form tight clusters. Ellipses encircle these clusters at 5 GHz and 23 GHz, while the data in the cluster at 15 GHz cannot be resolved at the scale of the figure. Model (b) gives results that agree much better with the data in the clusters than do (a) and (h). It is reassuring in this connection that (a) and (h) are the least realistic models of the transmission line shown in Fig. A-0-2.

It has already been mentioned that (a) ignores the effect of the competition between the absorption by water and the metal conductors, and that it only provides a lower bound to the fraction of the power absorbed in the water. For the transmission line analyzed here, (h) requires an unrealistically large reflection coefficient at the right-hand probe to compensate for the absorption that is associated with two complete passes along the transmission line. To a lesser extent, Model (g) also suffers from this problem.

The fact that five of the eight models that were compared here give substantially identical results for the fraction of the incident microwave radiation that is absorbed in a water filled channel under a range of reflection conditions suggests that these models can be used with some confidence. Specifically, they should provide reasonably accurate results when the measured reflectance as well as the interference fringes on the measured reflectance and transmittance spectra are small compared to the absorbed fraction of

interest. The reason for this is that the fraction of the microwave power that is absorbed in a transmission-line region as calculated from these models is not very sensitive to the detailed assumptions about which boundaries are reflecting. On the other hand, the calculated values of the reflection coefficients are quite sensitive to the same assumptions. Nevertheless, if it is not obvious from physical reasoning or examination of experimental reflection and transmittance spectra which of these reflection models best describes a particular complex transmission line, then it is probably a good idea to compare the results of a number of models as was done here.

In the general case, three-region devices will have four non-zero, non-identical reflection coefficients. Similar approximate equations that are accurate when the products of all combinations of two of the power reflection coefficients are small can be easily derived for this case, but more independent measurement results will be needed to use these equations in the way that was illustrated here. The needed results could be obtained by performing the S-parameter measurements with the same PDMS cover located in different positions along the axis of the coplanar waveguide to change the dimensions of Z_1 and Z_3. This will change the fractions of the power returned to Boundary A by the reflections from Boundaries B, C, and D. And it will change them in different ways for each boundary.

REFERENCES

REFERENCES

1.   Moore, G.E., *Electronics*, 1965. **38**: p.114-117.

2.   Wambaugh, J., *The Blooding*. 1989, New York: Bantam Books.

3.   Butler, J.M., *Forensic DNA Typing: Biology, Technology, and Genetics of STR Markers*. 2nd ed. 2005: Academic Press.

4.   Kobilinsky, L., Liotti, T.F., Oeser-Sweat, J., *DNA: Forensic and Legal Applications*. 2005, Hoboken: John Wiley & Sons, Inc.

5.   http://www.fbi.gov/hq/lab/codis/index1.htm *FBI's Combined DNA Index System (CODIS)*. May 11th 2007.

6.   Roper, M.G., Easley, C.J., Landers, J.P., *Anal. Chem.*, 2005. **77**(12): p.3887-3893.

7.   Horsman, K.M., Bienvenue, J.M., Blasier, K.R., Landers, J.P., *J. Forensic Sci.*, 2007. **52**(4): p.784-799.

8.   Saiki, R.K., Bugawan, T.L., Horn, G.T., Mullis, K.B., Erlich, H.A., *Nature*, 1986. **324**(6093): p.163-166.

9.   Nelson, D.L. Cox, M.L., *Lehninger Principles of Biochemistry*. 3rd ed. 2000, Ney York: Worth Publishers.

10.   Wittwer, C.T. Garling, D.J., *Biotechniques*, 1991. **10**(1): p.76-81.

11.   Baker, D.R., *Capillary Electrophoresis*. 1995, New York: John Wiley & Sons, Inc.

12.   Landers, J.P., ed. *Handbook of Capillary Electrophoresis*. 2nd ed. 1996, CRC Press: Boca Raton.

13.   Grossman, P.D. Colburn, J.C., *Capillary Electrophoresis: Theory and Practice*. 1992, San Diego: Academic Press, Inc.

14.   Heller, C., *Electrophoresis*, 1999. **20**: p.1978-1986.

15.   Butler, J.M., Buel, E., Crivellente, F., McCord, B.R., *Electrophoresis*, 2004. **25**(10-11): p.1397-1412.

16.   Lagally, E.T. Mathies, R.A., *J. Phys. D-Appl. Phys.*, 2004. **37**(23): p.R245-R261.

17.   Bienvenue, J.M., Duncalf, N., Marchiarullo, D., Ferrance, J.P., Landers, J.P., *J. Forensic Sci.*, 2006. **51**(2): p.266-273.

18.   Liu, R.H. Grodzinski, P., *J. Microlithogr. Microfabr. Microsyst.*, 2003. **2**(4): p.340-355.

19.   Liu, P., Seo, T.S., Beyor, N., Shin, K.J., Scherer, J.R., Mathies, R.A., *Anal. Chem.*, 2007. **79**(5): p.1881-1889.

20.   Pratt, T.C., Gaffney, M.J., Lovrich, N.P., Johnson, C.L., *Criminal Justice Policy Review*, 2006. **17**(1): p.32-47.

21.   Gravesen, P., Branebjerg, J., Jenson, O.S., *J. Micromech. Microeng.*, 1993. **3**: p.168-182.

22.   Terry, S.C., Jerman, J.H., Angell, J.B., *IEEE Trans. Electron Devices*, 1979. **26**(12): p.1880-1886.

23.   Manz, A., Graber, N., Widmer, H.M., *Sens. Actuators B, Chem. (Switzerland)*, 1990. **1**(1-6): p.244-248.

24.   Manz, A., Harrison, D.J., Verpoorte, E.M.J., Fettinger, J.C., Paulus, A., Ludi, H., Widmer, H.M., *Journal of Chromatography*, 1992. **593**(1-2): p.253-258.

25.   Harrison, D.J., Fluri, K., Seiler, K., Fan, Z.H., Effenhauser, C.S., Manz, A., *Science*, 1993. **261**(5123): p.895-897.

26.   Weigl, B.H. Yager, P., *Science*, 1999. **283**(5400): p.346-347.

27.   Wilding, P., Shoffner, M.A., Kricka, L.J., *Clin. Chem.*, 1994. **40**(9): p.1815-1818.

28.   Oda, R.P., Strausbauch, M.A., Huhmer, A.F.R., Borson, N., Jurrens, S.R., Craighead, J., Wettstein, P.J., Eckloff, B., Kline, B., Landers, J.P., *Anal. Chem.*, 1998. **70**(20): p.4361-4368.

29.   Beebe, D.J., Mensing, G.A., Walker, G.M., *Annu. Rev. Biomed. Eng.*, 2002. **4**: p.261-286.

30.   Jakeway, S.C., de Mello, A.J., Russell, E.L., *Fresenius J. Anal. Chem.*, 2000. **366**(6-7): p.525-539.

31.   Tudos, A.J., Besselink, G.A.J., Schasfoort, R.B.M., *Lab Chip*, 2001. **1**(2): p.83-95.

32.   Verpoorte, E., *Electrophoresis*, 2002. **23**(5): p.677-712.

33.   Huang, Y., Mather, E.L., Bell, J.L., Madou, M., *Anal. Bioanal. Chem.*, 2002. **372**(1): p.49-65.

34.   Kock, M., Evans, A., Brunnschweiler, A., *Microfluidic Technology and Applications*. 2000, Hertfordshire: Research Studies Press.

35.   Northrup, M.A., Ching, M.T., M., W.R., Watson, R.T. *Proceedings of Transducers '93*. 1993. p.924-926.

36. Lin, Y.C., Yang, C.C., Huang, M.Y., *Sens. Actuator B-Chem.*, 2000. **71**(1-2): p.127-133.

37. Yang, J.N., Liu, Y.J., Rauch, C.B., Stevens, R.L., Liu, R.H., Lenigk, R., Grodzinski, P., *Lab Chip*, 2002. **2**(4): p.179-187.

38. Burns, M.A., Johnson, B.N., Brahmasandra, S.N., Handique, K., Webster, J.R., Krishnan, M., Sammarco, T.S., Man, P.M., Jones, D., Heldsinger, D., Mastrangelo, C.H., Burke, D.T., *Science*, 1998. **282**(5388): p.484-487.

39. Woolley, A.T., Hadley, D., Landre, P., deMello, A.J., Mathies, R.A., Northrup, M.A., *Anal. Chem.*, 1996. **68**(23): p.4081-4086.

40. Lagally, E.T., Emrich, C.A., Mathies, R.A., *Lab Chip*, 2001. **1**(2): p.102-107.

41. Lagally, E.T., Medintz, I., Mathies, R.A., *Anal. Chem.*, 2001. **73**(3): p.565-570.

42. Taylor, T.B., WinnDeen, E.S., Picozza, E., Woudenberg, T.M., Albin, M., *Nucleic Acids Res.*, 1997. **25**(15): p.3164-3168.

43. Pal, R., Yang, M., Johnson, B.N., Burke, D.T., Burns, M.A., *Anal. Chem.*, 2004. **76**(13): p.3740-3748.

44. Koh, C.G., Tan, W., Zhao, M.Q., Ricco, A.J., Fan, Z.H., *Anal. Chem.*, 2003. **75**(22): p.6379-6379.

45. Zou, Q.B., Sridhar, U., Chen, Y., Singh, J., *IEEE Sens. J.*, 2003. **3**(6): p.774-780.

46. Chaudhari, A.M., Woudenberg, T.M., Albin, M., Goodson, K.E., *J. Microelectromech. Syst.*, 1998. **7**(4): p.345-355.

47. Yoon, D.S., Lee, Y.S., Lee, Y., Cho, H.J., Sung, S.W., Oh, K.W., Cha, J., Lim, G., *J. Micromech. Microeng.*, 2002. **12**(6): p.813-823.

48. Kopp, M.U., de Mello, A.J., Manz, A., *Science*, 1998. **280**(5366): p.1046-1048.

49.   Schneegass, I., Brautigam, R., Kohler, J.M., *Lab Chip*, 2001. **1**(1): p.42-49.

50.   Liu, J., Enzelberger, M., Quake, S., *Electrophoresis*, 2002. **23**(10): p.1531-1536.

51.   Wheeler, E.K., Benett, W., Stratton, P., Richards, J., Chen, A., Christian, A., Ness, K.D., Ortega, J., Li, L.G., Weisgraber, T.H., Goodson, K., Milanovich, F., *Anal. Chem.*, 2004. **76**(14): p.4011-4016.

52.   Obeid, P.J. Christopoulos, T.K., *Anal. Chim. Acta*, 2003. **494**(1-2): p.1-9.

53.   Giordano, B.C., Ferrance, J., Swedberg, S., Huhmer, A.F.R., Landers, J.P., *Anal. Biochem.*, 2001. **291**(1): p.124-132.

54.   Giordano, B.C., Copeland, E.R., Landers, J.P., *Electrophoresis*, 2001. **22**(2): p.334-340.

55.   Huhmer, A.F.R. Landers, J.P., *Anal. Chem.*, 2000. **72**(21): p.5507-5512.

56.   Easley, C.J., *Development and Application of Microfluidic Genetic Analysis Systems*, in *Department of Chemistry*. 2006, University of Virginia, Charlottesville: Charlottesville.

57.   Harrison, D.J., Manz, A., Fan, Z.H., Ludi, H., Widmer, H.M., *Anal. Chem.*, 1992. **64**(17): p.1926-1932.

58.   Schmalzing, D., Koutny, L., Adourian, A., Belgrader, P., Matsudaira, P., Ehrlich, D., *Proc. Natl. Acad. Sci. U. S. A.*, 1997. **94**(19): p.10273-10278.

59.   Schmalzing, D., Koutny, L., Chisholm, D., Adourian, A., Matsudaira, P., Ehrlich, D., *Anal. Biochem.*, 1999. **270**(1): p.148-152.

60.   Medintz, I.L., Berti, L., Emrich, C.A., Tom, J., Scherer, J.R., Mathies, R.A., *Clin. Chem.*, 2001. **47**(9): p.1614-1621.

61.   Mitnik, L., Carey, L., Burger, R., Desmarais, S., Koutny, L., Wernet, O., Matsudaira, P., Ehrlich, D., *Electrophoresis*, 2002. **23**(5): p.719-726.

62.   Shi, Y.N. Anderson, R.C., *Electrophoresis*, 2003. **24**(19-20): p.3371-3377.

63.   Goedecke, N., McKenna, B., El-Difrawy, S., Carey, L., Matsudaira, P., Ehrlich, D., *Electrophoresis*, 2004. **25**(10-11): p.1678-1686.

64.   Goedecke, N., McKenna, B., El-Difrawy, S., Gismondi, E., Swenson, A., Carey, L., Matsudaira, P., Ehrlich, D.J., *J. Chromatogr. A*, 2006. **1111**(2): p.206-213.

65.   Crouse, C., Yeung, S., Greenspoon, S., McGuckian, A., Sikorsky, J., Ban, J., Mathies, R., *Croat. Med. J.*, 2005. **46**(4): p.563-577.

66.   Jacobson, S.C., Hergenroder, R., Koutny, L.B., Ramsey, J.M., *Anal. Chem.*, 1994. **66**(7): p.1114-1118.

67.   Schaller, T., Bohn, L., Mayer, J., Schubert, K., *Precis. Eng.-J. Am. Soc. Precis. Eng.*, 1999. **23**(4): p.229-235.

68.   Beebe, D.J., Moore, J.S., Yu, Q., Liu, R.H., Kraft, M.L., Jo, B.H., Devadoss, C., *Proc. Natl. Acad. Sci. U. S. A.*, 2000. **97**(25): p.13488-13493.

69.   McCormick, R.M., Nelson, R.J., AlonsoAmigo, M.G., Benvegnu, J., Hooper, H.H., *Anal. Chem.*, 1997. **69**(14): p.2626-2630.

70.   Roberts, M.A., Rossier, J.S., Bercier, P., Girault, H., *Anal. Chem.*, 1997. **69**(11): p.2035-2042.

71.   Becker, H. Heim, U., *Sens. Actuator A-Phys.*, 2000. **83**(1-3): p.130-135.

72.   Qi, S.Z., Liu, X.Z., Ford, S., Barrows, J., Thomas, G., Kelly, K., McCandless, A., Lian, K., Goettert, J., Soper, S.A., *Lab Chip*, 2002. **2**(2): p.88-95.

73.   Aumiller, G.D., Chandros.Ea, Tomlinso.Wj, Weber, H.P., *J. Appl. Phys.*, 1974. **45**(10): p.4557-4562.

74.   Masuda, S., Washizu, M., Nanba, T., *IEEE Trans. Ind. Appl.*, 1989. **25**(4): p.732-737.

75.   Duffy, D.C., McDonald, J.C., Schueller, O.J.A., Whitesides, G.M., *Anal. Chem.*, 1998. **70**(23): p.4974-4984.

76.   Manz, A., Miyahara, Y., Miura, J., Watanabe, Y., Miyagi, H., Sato, K., *Sens. Actuator B-Chem.*, 1990. **1**(1-6): p.249-255.

77.   Nakanishi, H., Nishimoto, T., Nakamura, R., Yotsumoto, A., Yoshida, T., Shoji, S., *Sens. Actuator A-Phys.*, 2000. **79**(3): p.237-244.

78.   Niklaus, F., Stemme, G., Lu, J.Q., Gutmann, R.J., *J. Appl. Phys.*, 2006. **99**(3): p.28.

79.   Lakowicz, J.R., *Principles of Fluorescence Spectroscopy*. 1999, New York: Kluwer Academic/Plenum Publishers.

80.   Diaspro, A., ed. *Confocal and Two-Photon Microscopy: Foundations, Applications, and Advances*. 2002, Wiley-Liss, Inc.: New York.

81.   http://www.microscopyu.com *Introduction to Confocal Microscopy*. 08/25/2007.

82.   Pozar, D.M., *Microwave Engineering*. 3rd ed. 2004, Hoboken: John Wiley & Sons, Inc.

83.   Becker, H. Locascio, L.E., *Talanta*, 2002. **56**(2): p.267-287.

84.   McDonald, J.C. Whitesides, G.M., *Accounts Chem. Res.*, 2002. **35**(7): p.491-499.

85.   Manz, A., Fettinger, J.C., Verpoorte, E., Ludi, H., Widmer, H.M., Harrison, D.J., *Trac-Trends Anal. Chem.*, 1991. **10**(5): p.144-149.

86.   Kopp, M.U., Crabtree, H.J., Manz, A., *Curr. Opin. Chem. Biol.*, 1997. **1**(3): p.410-419.

87.   Becker, H. Gartner, C., *Electrophoresis*, 2000. **21**(1): p.12-26.

88.   Liu, Y.J., Ganser, D., Schneider, A., Liu, R., Grodzinski, P., Kroutchinina, N., *Anal. Chem.*, 2001. **73**(17): p.4196-4201.

89.   Chen, J.F., Wabuyele, M., Chen, H.W., Patterson, D., Hupert, M., Shadpour, H., Nikitopoulos, D., Soper, S.A., *Anal. Chem.*, 2005. **77**(2): p.658-666.

90.   Ye, M.Y., Yin, X.F., Fang, Z.L., *Anal. Bioanal. Chem.*, 2005. **381**(4): p.820-827.

91.   Chen, Z.F., Gao, Y.H., Lin, J.M., Su, R.G., Xie, Y., *J. Chromatogr. A*, 2004. **1038**(1-2): p.239-245.

92.   Yousefpour, A., Hojjati, M., Immarigeon, J.P., *J. Thermoplast. Compos. Mater.*, 2004. **17**(4): p.303-341.

93.   Kan, C.W., Fredlake, C.P., Doherty, E.A.S., Barron, A.E., *Electrophoresis*, 2004. **25**(21-22): p.3564-3588.

94.   Lin, C.B., Lee, S.B., Liu, K.S., *J. Adhes.*, 1991. **34**(1-4): p.221-240.

95.   Licata, M. Haag, E., *Plast. Eng.*, 1986. **42**(6): p.53-55.

96.   Klank, H., Kutter, J.P., Geschke, O., *Lab Chip*, 2002. **2**(4): p.242-246.

97.   Brown, L., Koerner, T., Horton, J.H., Oleschuk, R.D., *Lab Chip*, 2006. **6**(1): p.66-73.

98.   Hiratsuka, A., Muguruma, H., Lee, K.H., Karube, I., *Biosens. Bioelectron.*, 2004. **19**(12): p.1667-1672.

99. Kricka, L.J., Fortina, P., Panaro, N.J., Wilding, P., Alonso-Amigo, G., Becker, H., *Lab Chip*, 2002. **2**(1): p.1-4.

100. Liu, R.H., Yang, J.N., Lenigk, R., Bonanno, J., Grodzinski, P., *Anal. Chem.*, 2004. **76**(7): p.1824-1831.

101. Gerlach, A., Lambach, H., Seidel, D., *Microsyst. Technol.*, 1999. **6**(1): p.19-22.

102. Maas, D., Bustgens, B., Fahrenberg, J., Keller, W., Ruther, P., Schomburg, W.K., Seidel, D., *IEEE Robotics and Automation; The Ninth Annual International Workshop on Micro Electro Mechanical Systems.* , 1996: p.331-336.

103. Lin, R. Burns, M.A., *J. Micromech. Microeng.*, 2005. **15**(11): p.2156-2162.

104. Kelly, R.T. Woolley, A.T., *Anal. Chem.*, 2005. **77**(5): p.96A-102A.

105. Martynova, L., Locascio, L.E., Gaitan, M., Kramer, G.W., Christensen, R.G., MacCrehan, W.A., *Anal. Chem.*, 1997. **69**(23): p.4783-4789.

106. Doherty, E.A.S., Kan, C.W., Barron, A.E., *Electrophoresis*, 2003. **24**(24): p.4170-4180.

107. Doherty, E.A.S., Kan, C.W., Paegel, B.M., Yeung, S.H.I., Cao, S.T., Mathies, R.A., Barron, A.E., *Anal. Chem.*, 2004. **76**(18): p.5249-5256.

108. Grossman, P.D., *J. Chromatogr. A*, 1994. **663**(2): p.219-227.

109. Buchholz, B.A., Shi, W., Barron, A.E., *Electrophoresis*, 2002. **23**(10): p.1398-1409.

110. Liu, J.K., Pan, T., Woolley, A.T., Lee, M.L., *Anal. Chem.*, 2004. **76**(23): p.6948-6955.

111. Hjerten, S. Kubo, K., *Electrophoresis*, 1993. **14**(5-6): p.390-395.

153

112. Towns, J.K. Regnier, F.E., *Anal. Chem.*, 1992. **64**(21): p.2473-2478.

113. Dolnik, V., *Electrophoresis*, 2004. **25**(21-22): p.3589-3601.

114. Gilges, M., Kleemiss, M.H., Schomburg, G., *Anal. Chem.*, 1994. **66**(13): p.2038-2046.

115. Proctor, K.G., Ramirez, S.K., McWilliams, K.L., Huerta, J.L., Kirkland, J.J., *Chemically Modified Surfaces: Recent Developments*. 1996, Cambridge: The Royal Society of Chemistry.

116. Boone, T., Fan, Z.H., Hooper, H., Ricco, A., Tan, H.D., Williams, S., *Anal. Chem.*, 2002. **74**(3): p.78A-86A.

117. Soper, S.A., Ford, S.M., Qi, S., McCarley, R.L., Kelly, K., Murphy, M.C., *Anal. Chem.*, 2000. **72**(19): p.642A-651A.

118. Zangmeister, R.A. Tarlov, M.J., *Langmuir*, 2003. **19**(17): p.6901-6904.

119. Ichijima, H., Okada, T., Uyama, Y., Ikada, Y., *Makromolekulare Chemie-Macromolecular Chemistry and Physics*, 1991. **192**(5): p.1213-1221.

120. Lawrence, J. Li, L., *Mater. Sci. Eng. A-Struct. Mater. Prop. Microstruct. Process.*, 2001. **303**(1-2): p.142-149.

121. Hozumi, A., Masuda, T., Hayashi, K., Sugimura, H., Takai, O., Kameyama, T., *Langmuir*, 2002. **18**(23): p.9022-9027.

122. Vasilets, V.N., Hirata, I., Iwata, H., Ikada, Y., *J. Polym. Sci. Pol. Chem.*, 1998. **36**(13): p.2215-2222.

123. Chaudhury, M.K. Whitesides, G.M., *Langmuir*, 1991. **7**(5): p.1013-1025.

124. Feurer, B. Harel, J.P., *Thin Solid Films*, 1983. **100**(3): p.249-255.

125. Henry, A.C., Tutt, T.J., Galloway, M., Davidson, Y.Y., McWhorter, C.S., Soper, S.A., McCarley, R.L., *Anal. Chem.*, 2000. **72**(21): p.5331-5337.

126. Vaidya, B., Soper, S.A., McCarley, R.L., *Analyst*, 2002. **127**(10): p.1289-1292.

127. Soper, S.A., Henry, A.C., Vaidya, B., Galloway, M., Wabuyele, M., McCarley, R.L., *Anal. Chim. Acta*, 2002. **470**(1): p.87-99.

128. Johnson, T.J., Ross, D., Gaitan, M., Locascio, L.E., *Anal. Chem.*, 2001. **73**(15): p.3656-3661.

129. Johnson, T.J., Waddell, E.A., Kramer, G.W., Locascio, L.E., *Appl. Surf. Sci.*, 2001. **181**(1-2): p.149-159.

130. Wu, D.P., Luo, Y., Zhou, X.M., Dai, Z.P., Lin, B.C., *Electrophoresis*, 2005. **26**(1): p.211-218.

131. Vig, J.R., *J. Vac. Sci. Technol. A-Vac. Surf. Films*, 1985. **3**(3): p.1027-1034.

132. Skurat, V.E. Dorofeev, Y.I., *Angewandte Makromolekulare Chemie*, 1994. **216**: p.205-224.

133. Liston, E.M., *J. Adhes.*, 1989. **30**(1-4): p.199-218.

134. Doherty, E.A.S., Berglund, K.D., Buchholz, B.A., Kourkine, I.V., Przybycien, T.M., Tilton, R.D., Barron, A.E., *Electrophoresis*, 2002. **23**(16): p.2766-2776.

135. Albarghouthi, M.N., Stein, T.M., Barron, A.E., *Electrophoresis*, 2003. **24**(7-8): p.1166-1175.

136. Shah, J.J., Geist, J., Locascio, L.E., Gaitan, M., Rao, M.V., Vreeland, W.N., *Anal. Chem.*, 2006. **78**(10): p.3348-3353.

137. Zhang, C.S., Xu, J.L., Ma, W.L., Zheng, W.L., *Biotechnol. Adv.*, 2006. **24**(3): p.243-284.

138.	Waters, L.C., Jacobson, S.C., Kroutchinina, N., Khandurina, J., Foote, R.S., Ramsey, J.M., *Anal. Chem.*, 1998. **70**(1): p.158-162.

139.	Lee, C.Y., Lee, G.B., Lin, J.L., Huang, F.C., Liao, C.S., *J. Micromech. Microeng.*, 2005. **15**(6): p.1215-1223.

140.	Maltezos, G., Johnston, M., Scherer, A., *Appl. Phys. Lett.*, 2005. **87**(15): p.1541051-1541053.

141.	de Mello, A.J., Habgood, M., Lancaster, N.L., Welton, T., Wootton, R.C.R., *Lab Chip*, 2004. **4**(5): p.417-419.

142.	Wittwer, C.T., Fillmore, G.C., Garling, D.J., *Anal. Biochem.*, 1990. **186**(2): p.328-331.

143.	Wittwer, C.T., Fillmore, G.C., Hillyard, D.R., *Nucleic Acids Res.*, 1989. **17**(11): p.4353-4357.

144.	Tanaka, Y., Slyadnev, M.N., Hibara, A., Tokeshi, M., Kitamori, T., *J. Chromatogr. A*, 2000. **894**(1-2): p.45-51.

145.	Ke, C., Berney, H., Mathewson, A., Sheehan, M.M., *Sens. Actuator B-Chem.*, 2004. **102**(2): p.308-314.

146.	Pal, D. Venkataraman, V., *Sens. Actuator A-Phys.*, 2002. **102**(1-2): p.151-156.

147.	Bengtsson, N.E. Ohlsson, T., *Proc. IEEE (USA)*, 1974. **62**(1): p.44-55.

148.	Bykov, Y.V., Rybakov, K.I., Semenov, V.E., *J. Phys. D-Appl. Phys.*, 2001. **34**(13): p.R55-R75.

149.	Wei, Y.Z. Sridhar, S., *J. Chem. Phys. (USA)*, 1990. **92**(2): p.923-928.

150.	Kappe, C.O. Dallinger, D., *Nat. Rev. Drug Discov.*, 2006. **5**(1): p.51-63.

151.   Fermer, C., Nilsson, P., Larhed, M., *Eur. J. Pharm. Sci.*, 2003. **18**(2): p.129-132.

152.   Auroux, P.A., Shah, J.J., Booth, J., Rao, M.V., Locascio, L.E., Gaitan, M. *Micro Total Analysis Systems*. 2006. p.1465-1467.

153.   Goodwin, D.C. Lee, S.B., *Biotechniques*, 1993. **15**(3): p.438-&.

154.   Nikawa, Y., Yamamoto, K., Izumidate, S., Kubota, N. *18th International Conference of the IEEE Engineering in Medicine and Biology Society*. 1996. p.1865-1866.

155.   Sundaresan, S.G., Polk, B.J., Reyes, D.R., Rao, M.V., Gaitan, M. *Micro Total Analysis Systems* 2005. p.657-659.

156.   Sklavounos, A., Marchiarullo, D.J., Barker, S.L.R., J.P., L., Barker, N.S. *Micro Total Analysis Systems 2006*. 2006. p.1238-1240.

157.   Booth J. C., M.J., Janezic M., Baker-Jarvis J., and Beall J. A. *IEET MTT-S Int. Microwave Symp.* 2006. p.1750-1753.

158.   Facer, G.R., Notterman, D.A., Sohn, L.L., *Appl. Phys. Lett.*, 2001. **78**(7): p.996-998.

159.   Duffy, D.C., Schueller, O.J.A., Brittain, S.T., Whitesides, G.M., *J. Micromech. Microeng.*, 1999. **9**(3): p.211-217.

160.   Engen, G.F., *IEEE Trans. Microw. Theory Tech.*, 1997. **45**(12): p.2414-2417.

161.   Ross, D., Gaitan, M., Locascio, L.E., *Anal. Chem.*, 2001. **73**(17): p.4117-4123.

162.   Arbeloa, T.L., Estevez, M.J.T., Arbeloa, F.L., Aguirresacona, I.U., Arbeloa, I.L., *J. Lumines.*, 1991. **48-9**: p.400-404.

163.   Kubin, R.F. Fletcher, A.N., *J. Lumines.*, 1982. **27**(4): p.455-462.

164. Gallery, J., Gouterman, M., Callis, J., Khalil, G., McLachlan, B., Bell, J., *Rev. Sci. Instrum.*, 1994. **65**(3): p.712-720.

165. Lemoine, F., Antoine, Y., Wolff, M., Lebouche, M., *Exp. Fluids*, 1999. **26**(4): p.315-323.

166. Tiercelin, N., Coquet, P., Sauleau, R., Senez, V., Fujita, H., *J. Micromech. Microeng.*, 2006. **16**(11): p.2389-2395.

167. Geist, J., Shah, J.J., Rao, M.V., Gaitan, M., *Journal of Research of the National Institute of Standards and Technology*, 2007. **112**(4): p.177-189.

168. Franks, F., *Water: a comprehensive treatise*. 1972: Plenum Press.

169. Carslaw H. S., J., J. C., *Conduction of Heat in Solids*. 2nd ed. 1959: Oxford University Press, Oxford.

170. Barrat, J.L. Chiaruttini, F., *Mol. Phys.*, 2003. **101**(11): p.1605-1610.

171. Tsao, C.W., Hromada, L., Liu, J., Kumar, P., DeVoe, D.L., *Lab Chip*, 2007. **7**(4): p.499-505.

172. Spanner, D.C., *Symposium of the Society for Experimental Biology*, 1954. **8**: p.76-93.

173. Alpert, Y. Jerby, E., *IEEE Trans. Plasma Sci.*, 1999. **27**(2): p.555-562.

174. Jacob, W., von Keudell, A., Schwarz-Selinger, T., *Braz. J. Phys.*, 2000. **30**(3): p.508-516.

Curriculum Vitae

Jayna Shah was born on July 28th 1980 in Gujarat, India. She moved to the USA with her family in 1996. She attended Newman Smith High School in Carrollton, TX and graduated in 1997. She went on to attend the University of Texas at Dallas (UTD) from where she received a Bachelors of Science degree in Electrical Engineering in 2001. During her undergraduate career, she worked at Alcatel USA, Inc. as a Co-Op student from 1999 to 2001. After graduating from UTD, she worked at Alcatel USA as an Electrical Design Engineer from 2001 to 2002.

She moved to Washington D.C. Metropolitan area in 2003 and became a graduate student at George Mason University (GMU) in Fairfax, VA. She completed her Masters of Science degree in Electrical Engineering from GMU in 2007. Her doctoral dissertation work was carried out in the Semiconductor Electronics Division at the National Institute of Standards and Technology (NIST) in Gaithersburg, MD, where she also worked as a Guest Researcher from 2003 to 2007. She received numerous merit-based fellowships as a graduate student including Armed Forces Communications and Electronics Association (AFCEA) and the School of Information and Technology of GMU's masters and doctoral research fellowships. She is a student member of IEEE. Her research interests include development of microfluidics technology for DNA fingerprinting, integrated microwave circuits for biological and fluidic applications, and studying microwave interactions with biological molecules.